EFFECT OF TITANIUM DIOXIDE NANOPARTICLES ON EARLY AGE AND LONG TERM PROPERTIES OF CEMENTITIOUS MATERIALS

A Dissertation
Presented to
The Academic Faculty

by

Bo Yeon Lee

In Partial Fulfillment
of the Requirements for the Degree
Doctor of Philosophy in the
School of Civil & Environmental Engineering

Georgia Institute of Technology
August 2012

EFFECT OF TITANIUM DIOXIDE NANOPARTICLES ON EARLY AGE AND LONG TERM PROPERTIES OF CEMENTITIOUS MATERIALS

Approved by:

Dr. Kimberly E. Kurtis, Advisor
School of Civil & Environmental Engineering
Georgia Institute of Technology

Dr. Angus P. Wilkinson
School of Chemistry & Biochemistry
Georgia Institute of Technology

Dr. Michael H. Bergin
School of Civil & Environmental Engineering
Georgia Institute of Technology

Dr. T. Russell Gentry
School of Architecture
Georgia Institute of Technology

Dr. Lawrence F. Kahn
School of Civil & Environmental Engineering
Georgia Institute of Technology

Date Approved: June 08, 2012

I can do all this through him who gives me strength.
Philippians 4:13

ACKNOWLEDGEMENTS

I would like to express my utmost gratitude to my advisor Dr. Kimberly E. Kurtis for her guidance throughout my Ph.D. study at Georgia Institute of Technology. Her insightful advice and guidance have been absolutely priceless and I am very fortunate to have her as my advisor. I would also like to thank my thesis committee members, Dr. Michael Bergin, Dr. Lawrence Kahn, Dr.Angus Wilkinson, and Dr. Russell Gentry for their time and support. My appreciation is also given to Amal Jayapalan for coworking on a same project.

I would like to thank all my current and previous lab members, Amal Jayapalan, Dr. Robert Moser, Dr. Jun Chen, Dr. Victor Garas, Chris Shearer, Passarin Jongvisuttisun, Bradley Dolphyn, Elizabeth Nadelman, Nathan Mayercsik, and Sarah Fredrich for their help and friendship. I am also very grateful to all the undergraduate students who have helped me with many experiments. I owe my sincere gratitude to my friends at Georgia Tech, especially to Sujin Kim, Eunjeong Cha, and Yoonduk Kim, for their good friendship.

Most importantly, I must express my deepest gratitude to my father Dr. Chong Bum Lee, my mother Mrs. Woo Kyung Lee, and my brother Jinsoo Lee for their unconditional love and abundant support. Without them, I would not have been the person I am today.

Last but not least, I thank my fiancé, Jihun Oh, with all my heart for his unwavering love, encouragement, and supports. He has been extremely supportive of me in my hardest times, and I appreciate everything that he has done for me.

TABLE OF CONTENTS

ACKNOWLEDGEMENTS iv

LIST OF TABLES xi

LIST OF FIGURES xii

LIST OF SYMBOLS AND ABBREVIATIONS xvi

SUMMARY xix

CHAPTER 1 INTRODUCTION

1.1 Background 1

1.2 TiO_2 Used in Construction Materials – Sustainable Development 8

1.3 Research Motivation 9

1.4 Research Objectives 10

1.5 Organization of Dissertation 12

1.6 References 13

CHAPTER 2 LITERATURE REVIEW

2.1 Use of Nanotechnology in Cement and Concrete 16

2.1.1 Definition of Nanotechnology in Cement and Concrete 16

2.1.2 Nano-Engineering of Cement and Concrete 17

2.1.3 Nanotechnology in Terms of Sustainable Development 19

2.2 Photocatalytic Cement 19

2.2.1 Titanium Dioxide 20

2.2.1.1 History 20

2.2.1.2 Crystal Structures 20
2.2.1.3 Photocatalytic Oxidation Reaction 22
2.2.2 NOx Oxidation Reactions 23
2.3 Early Age Hydration 25
2.3.1 Effect of Fine Additives on Cement Hydration 25
2.3.2 Early Age Hydration Mathematical Models 27
2.3.2.1 Avrami Nucleation and Growth Model 28
2.3.2.2 Boundary Nucleation Model 30
2.4 Photocatalytic Nitrogen Oxides Oxidation Experiments 32
2.4.1 NOx Removal Test Standards 32
2.4.1.1 JIS R 1701-1 32
2.4.1.2 ISO 22197-1 33
2.4.1.3 UNI 11247 34
2.4.2 Method for Current Study 35
2.5 Durability of Photocatalytic Cement 36
2.5.1 Acid Attack 36
2.5.2 Salt Crystallization 37
2.5.3 Carbonation 42
2.6 References 43

CHAPTER 3 EFFECTS OF NANO-TITANIUM DIOXIDE ON PROPERTIES OF CEMENTITIOUS MATERIALS

3.1 Introduction 54
3.2 Experimental Procedure 56

3.2.1 Materials ····· 56

3.2.2 Sample Preparation ····· 58

3.2.3 Methodology ····· 59

3.2.3.1 Isothermal Calorimetry ····· 59

3.2.3.2 Chemical Shrinkage ····· 60

3.2.3.3 Setting Time ····· 60

3.2.3.4 Compressive Strength ····· 61

3.2.3.5 Microhardness ····· 61

3.3 Results and Discussion ····· 62

3.3.1 Early Age Hydration ····· 62

3.3.2 Chemical Shrinkage ····· 66

3.3.3 Setting Time ····· 69

3.3.4 Compressive Strength ····· 71

3.3.5 Microhardness ····· 75

3.4 Conclusions ····· 77

3.5 References ····· 78

CHAPTER 4 INFLUENCE OF TiO_2 NANOPARTICLES ON EARLY ALITE AND BELITE HYDRATION

4.1 Introduction ····· 83

4.2 Theoretical Background ····· 85

4.2.1 Avrami Nucleation and Growth Model ····· 86

4.2.2 Boundary Nucleation Model ····· 87

4.3 Materials and Experimental Procedure ····· 90

4.4 Results and Discussion 95

4.4.1 C_3S Calorimetry Data 95

4.4.2 C_2S Calorimetry Data 101

4.4.3 C_3S Model Fits 108

4.5 Conclusions 113

4.6 References 115

CHAPTER 5 PHOTOCATALYTIC CEMENT EXPOSED TO NITROGEN OXIDES: EFFECT OF OXIDATION AND BINDING

5.1 Introduction 121

5.2 Materials and Experimental Procedure 123

5.2.1 Materials 123

5.2.2 Sample Preparation 123

5.2.3 Methodology 125

5.2.3.1 Photocatalysis Series with NO and NO_2 gases 126

5.2.3.2 NO and NO_2 Binding Series 127

5.3 Results and Discussion 128

5.3.1 Photocatalysis Series under NO and NO_2 128

5.3.2 NO and NO_2 Binding Series 134

5.4 Conclulsions 142

5.5 Reference 144

CHAPTER 6 DURABILITY OF PHOTOCATALYTIC CEMENT AFTER NITROGEN OXIDES-WET-DRY CYCLING

6.1 Introduction 146

6.2 Experiment 147

6.2.1 Materials and Sample Preparation 149

6.2.1.1 NO Experiment 149

6.2.1.2 NO_2 Experiment 150

6.2.2 Experimental Procedure 151

6.2.3 Surface Examinations 155

6.3 Results and Discussion 157

6.3.1 Photocatalytic Efficiency 157

6.3.2 Scanning Electron Microscopy 162

6.3.3 Microhardness 164

6.3.4 Surface Roughness 166

6.3.5 X-ray Diffraction Analysis 167

6.3.6 Mass Changes 171

6.4 Conclusions 171

6.5 References 173

CHAPTER 7 SALT CRYSTALLIZATION DAMAGE TO TiO_2 CONTAINING MORTAR BARS

7.1 Introduction 175

7.2 Theoretical Background 176

7.3 Experimental Procedure 178

7.3.1 Materials and Sample Preparation 178

7.3.2 Procedure: Salt Solution Exposure Conditions 179

7.4 Results and Discussion 182

7.4.1 Effect of Different Salt Solutions and Varying Water-to-Binder Ratio 182

7.4.2 Effect of Different Amounts of TiO_2 191

7.5 Conclusions 196

7.6 References 197

CHAPTER 8 CONCLUSIONS AND FUTURE RESEARCH

8.1 Conclusions and Contributions of Research 198

8.2 Recommendations 201

8.3 Future Research 203

8.4 References 206

VITA 207

LIST OF TABLES

Table 1.1—Air quality standards for NO_2 in several countries 7

Table 3.1—Properties of TiO_2 samples used 58

Table 3.2—Chemical oxide analysis and Bogue potential composition of cement 58

Table 3.3—Cumulative heat of hydration and degree of hydration compared to control 66

Table 3.4—Chemical shrinkage of P25 and PC50 modified cement pastes 68

Table 4.1—Cumulative heat of hydration and degree of hydration, α, of TiO_2-blended C_3S pastes at 12 and 24 h. 101

Table 4.2—Cumulative heat of hydration and degree of hydration, α, of TiO_2-blended C_2S pastes at 30, 60, and 90 days 107

Table 4.3—Area fractions of C_3S, TiO_2, hydration products, and porosity at 0 and 12 hrs. 109

Table 4.4—Fit parameters A, t_0, k_{avr}, and n for Avrami model 111

Table 4.5—Fit parameters O_v^B, A, t_0, G, I_B, k_B, k_G, and k_B/k_G for boundary nucleation model 111

Table 5.1—Photocatalytic efficiency of samples at different times 130

Table 6.1—Summary of the experimental conditions: NO and NO_2 experiments 154

Table 7.1—Experimental detail 180

Table 7.2—Damaged surfaces of samples immersed in $Ca(NO_3)_2$ solution 190

LIST OF FIGURES

Figure 1.1—Annual average NO_2 concentration trend in the US, 2001-2010 4

Figure 1.2—Annual average NO_2 concentration in 2000-2005 reported from selected cities worldwide 5

Figure 2.1—Crystal structures of TiO_2 (a) anatase, (b) rutile, and (c) brookite 21

Figure 2.2—Mechanism of photocatalytic TiO_2 23

Figure 3.1—Particle size distribution of TiO_2 powders 57

Figure 3.2—(a) Hydration rate of P25 and PC50 blended cement pastes, (b) Cumulative heat of hydration of P25 and PC50 blended cement pastes 64

Figure 3.3—Chemical shrinkage of P25 and PC50 modified cement pastes 67

Figure 3.4—Initical and final setting times of ordinary Portland cement and TiO_2 modified cements 70

Figure 3.5—Compressive strength of 0%, 5%, and 10% TiO_2-cement samples at w/c=0.50 72

Figure 3.6—Compressive strength of w/c=0.40, 0.50, and 0.60 samples at 28 days 74

Figure 3.7—Microhardness of 0%, 5%, and 10% TiO_2-cement samples 76

Figure 4.1—Boundary nucleation model fits to experimental rate curve at (1) $k_B/k_G = 0.1$, (2) $k_B/k_G = 1.3$, and (3) $k_B/k_G = 3$ 90

Figure 4.2—Diffraction pattern for C_3S sample compared to reference pattern for C_3S 91

Figure 4.3—Diffraction pattern for C_2S sample compared to reference pattern for C_2S 92

Figure 4.4—Particle size distribution of TiO_2 powder 92

Figure 4.5—(a) Hydration rate of TiO_2-blended C_3S pastes (b) Hydration rate of TiO_2-blended cement pastes 96

Figure 4.6—(a) Cumulative heat of hydration of TiO_2-blended C_3S pastes (b) Cumulative heat of hydration of TiO_2-blended cement pastes 97

Figure 4.7—Hydration rate of TiO_2-blended C_2S pastes 102

Figure 4.8—Cumulative heat of hydration of TiO_2-blended C_2S pastes 102

Figure 4.9—0%, 5%, 10%, and 15% TiO_2 at 0, 12 hrs hydration;
α=37, 42, 50, and 54% respectively ····· 109

Figure 4.10—Rate of hydration: Experiment vs. Avrami and BN models
(a) 0% TiO_2, (b) 5% TiO_2, (c) 10% TiO_2, and (d) 15% TiO_2 ····· 110

Figure 5.1—NOx reactor with UV light on ····· 126

Figure 5.2—Experimental set-up showing NO/NO_2 flow and UV reactor ····· 126

Figure 5.3—NO test data with samples with w/c=0.40, 0.50, and 0.60,
each with 5% TiO_2 by mass of cement ····· 129

Figure 5.4—NO_2 test data with samples with w/c=0.40, 0.50, and 0.60,
each with 5% TiO_2 by mass of cement ····· 129

Figure 5.5—Blank concentration: gas concentration after samples taken out of
the reactor (a) NO experiment, (b) NO_2 experiment ····· 133

Figure 5.6—(a) NO gas absorption in wet cement paste samples,
(b) NO gas absorption in dry cement paste samples ····· 136

Figure 5.7—(a) NO_2 gas absorption in wet cement paste samples,
(b) NO_2 gas absorption in dry cement samples ····· 137

Figure 5.8—(a) NO gas absorption in synthetic pore solution,
(b) NO_2 gas absorption in synthetic pore solution ····· 139

Figure 5.9—NO_2 sorption on hardened cement paste as well as into pore solution ····· 141

Figure 6.1—Diagram of the experimental process ····· 148

Figure 6.2—Vickers indentation mark obtained after 15 cycles on NO experiment ···· 156

Figure 6.3—Surface reconstructed after 15 cycles on NO experiment using
confocal microscope. Each direction measures 500 micrometers. ····· 157

Figure 6.4—NOx, NO and NO_2 concentration at 1st cycle (a) NO experiment
(b) NO_2 experiment ····· 159

Figure 6.5—(a) NO experiment: NOx concentration changes per tile when
UV light is on/off, (b) NO_2 experiment: NOx concentration
changes per tile when UV light is on/off. ····· 161

Figure 6.6—SEM image of a sample in NO experiment (a) before exposure,
(b) after 20 cycles of exposure ····· 163

Figure 6.7—SEM image of a sample in NO_2 experiment (a) before exposure,
(b) after 12 cycles of exposure ····· 164

Figure 6.8—Vickers hardness of samples exposed to NO or NO_2 and wet-dry cycling 166

Figure 6.9—Surface roughness of samples exposed to NO or NO_2 and wet-dry cycling 167

Figure 6.10—X-ray diffraction pattern of samples exposed to NOx wet-dry cycling (a) NO experiment, (b) NO_2 experiment 170

Figure 6.11—Mass changes of samples exposed to NO or NO_2 and wet-dry cycling .. 171

Figure 7.1—Schematic of capillary rise and evaporation 178

Figure 7.2—Mortar bars partially immersed in test solution 181

Figure 7.3—Schematic diagram of the experimental setup 181

Figure 7.4—Picture of the experimental setup 182

Figure 7.5—Samples partially immersed in 15% $Ca(NO_3)_2$ solution (a) w/b=0.40, (b) w/b=0.50, and (c) w/b=0.60 183

Figure 7.6—Samples partially immersed in 30% $Ca(NO_3)_2$ solution (a) w/b=0.40, (b) w/b=0.50, (c) w/b=0.60, and (d) crack detail of w/b=0.6 sample 183

Figure 7.7—Samples partially immersed in 15% Na_2SO_4 solution (a) w/b=0.40, (b) w/b=0.50, and (c) w/b=0.60 184

Figure 7.8—Samples partially immersed in deionized water (a) w/b=0.40, (b) w/b=0.50, and (c) w/b=0.60 184

Figure 7.9—X-ray diffraction pattern of salt outside of w/b=0.60 sample immersed in 15% Na_2SO_4 solution. "T" designates Thenardite, anhydrous form of Na_2SO_4 188

Figure 7.10—Phase diagram for sodium sulfate 188

Figure 7.11—Diffraction pattern of w/b=0.60 sample immersed in 30% $Ca(NO_3)_2$ solution. The top and the bottom represent deteriorated part and unaffected part, respectively 191

Figure 7.12—w/b=0.50 samples partially immersed in 15% $Ca(NO_3)_2$ solution (a) 0% TiO_2, (b) 5% TiO_2, (c) 10% TiO_2, and (d) 15% TiO_2 192

Figure 7.13—w/b=0.50 samples partially immersed in 15% $Ca(NO_3)_2$ solution (a) 0% TiO_2, (b) 5% TiO_2, (c) 10% TiO_2, and (d) 15% TiO_2 193

Figure 7.14—(a) Cumulative pore area distribution and (b) Cumulative pore volume distribution of w/b=0.50 paste samples at 7 days of curing at 0%, 5%, and 10% TiO_2 replacement 195

LIST OF SYMBOLS AND ABBREVIATIONS

A	Cement chemistry notation, Al_2O_3
Ȧ	Normalization constant for Avrami model and boundary nucleation model
Ā	Area of the surface in contact with the ground
ACI	American Ceramic Society
ACC	Anthropogenic climate change
ANOVA	Analysis of variance
BET method	Brunauer-Emmett-Teller method
BJH method	Barrett, Joyner, Hallenda method
BN model	Boundary nucleation model
C	Cement chemistry notation, CaO
C_2S	dicalcium silicate, belite
C_3S	tricalcium silicate, alite
CB	Conduction band
CH	Calcium hydroxide
C_p^{C2S}	Specific heat of C_2S
C_p^{paste}	Specific heat of fresh C_2S paste containing TiO_2 powder
C_p^{TiO2}	Specific heat of TiO_2
C_p^{water}	Specific heat of water
C-S-H	Calcium silicate hydrate
F	Cement chemistry notation, Fe_2O_3
G	Constant linear growth rate
g	Gravitational acceleration

h	Height that the liquid has risen to
h_s	Equilibrium height where the rate of capillary rise and drying are equal
I_B	Nucleation rate per unit area of boundary
ICP-OES	Inductively coupled plasma optical emission spectrophotometry
I_v	Rate of nucleation per unit of untransformed volume
J_c	Flux from the capillary rise
J_E	Rate of evaporation from the surface of a material
k	Permeability
k_{avr}	Effective rate constant of the Avrami model
k_B	Rate of transformation on the grain boundaries
k_G	Rate of transformation in the bulk matrix
LCA	Life cycle analysis
NAAQS	National Ambient Air Quality Standards
O_v^B	Total boundary area
O_v^b	Boundary area of a single plane
PAN	Peroxyacetyl nitrate
p_c	Capillary pressure
PM	Particulate matter
QXRD	Quantitative x-ray diffraction
R	Hydration rate
S	Cement chemistry notation, SiO_2
SEM	Scanning electron microscopy
t	Time since the start of the total reaction
t_0	Delay between the time of mixing and the time of start of nucleation and growth kinetics

TiO_2	Titanium dioxide
UNI	Italian organization for standardization
USEPA	United States Environmental Protectio Agency
VB	Valence band
VOC	Volatile organic compounds
w/b	Water-to-binder ratio
w/c	Water-to-cement ratio
w/s	Water-to-solid ratio
WHO	World Health Organization
X	True volume fraction
x^{C2S}	Mass fraction of C_2S in paste
X^e	Extended volume fraction
x^{TiO2}	Mass fraction of TiO_2 in paste
x^{water}	Mass fraction of water in paste
Y	True area of intersection
y	Distance between a single planar boundary and another plane parallel to this plane
Y^e	Extended area of the intersection between the plane and all regions nucleated on the grain boundary
η	Viscosity
ρ_L	Density of liquid
τ	Time at which the particular region nucleated
ϕ	Porosity of a material

SUMMARY

Today, with increasing global awareness and regulation of air pollution, interest in the smog-abating property of photocatalytic materials is increasing. Nanoparticles of titanium dioxide (TiO_2) are perhaps the most well known photocatalytic semiconductor and its use as passive but potentially effective means to reduce atmospheric nitrogen oxides ($NOx=NO+NO_2$) has been relatively recently introduced in construction materials, commercially sold as photocatalytic cements, photocatalytic pavements, self-cleaning tiles, and self-cleaning glass.

Prior research has examined the photocatalytic properties of the TiO_2 itself, as well as TiO_2-containing cement-based materials, and the majority of this effort has been on characterizing and enhancing the photocatalytic efficiency. However, relatively little research was performed to assess the potential impact of the photocatalytic reaction on the "parent" or "host" material.

In this research, the focus is on the effect of addition of chemically inert TiO_2 nanoparticles and the photocatalysis on the composition, structure, and properties of cementitious materials, which contain titania nanoparticles at early and late ages. With the addition of TiO_2 nanoparticles, the rate of early cement hydration and the degree of hydration are increased, resulting in decreased setting time and increased compressive strength at lower water-to-cement ratio, but with decreased microhardness. It was shown from modeling that the high surface area of nanoparticles provides nucleation sites for hydration products to form, thus accelerating the rate of hydration through a boundary nucleation effect. These series of results suggest that the TiO_2 nanoparticles could be

used to optimize cementitious materials to achieve specific early age behavior as well as hardened properties, setting aside the photocatalytic benefit. Further, the accelerated hydration of C_2S implies a potential pathway to sustainable development by using C_2S-rich cements that can be produced at lower temperatures while emitting less CO_2 during manufacture.

In the latter part of the study, the photocatalytic efficiency and the effects of the TiO_2 on the long-term durability of cement-based materials are investigated to demonstrate their suitability for long-term use in the field. The photocatalytic efficiency of the TiO_2 containing cementitious material under NO and NO_2 gases are similar at 3 hours of NOx/UV exposure. However, the efficiency decreases with long-term NOx and ultraviolet light exposure and with wet-dry cycling, possibly due to carbonation and overgrowth of hydration products. Also, it was found that the NO_2 gas has a greater potential to be bound in hardened cement paste than the NO gas, even in the absence of photocatalysis (e.g., without light exposure). Because the amount of NO_2 bound is comparable to the amount decreased by photocatalytic reactions, this new observation suggests that the photocatalytic cement-based materials could be used to alleviate NO_2 gas through both photocatalysis and binding within the cementitious matrix. Cycles of NOx and wet/dry exposure result in pits on the sample surfaces, as evidenced by SEM images, suggesting that extensive NOx and wet-drying has a potential to generate surface damage of a cementitious materials. However, microhardness, surface roughness, and x-ray diffraction are found to be insensitive to these changes. A separate salt crystallization experiment indicates that calcium nitrate, the possible product of photocatalysis, could damage cementitious materials by salt crystallization pressure at low relative humidity.

CHAPTER 1

INTRODUCTION

1.1 Background

Increasing worldwide urbanization negatively affects air quality. Stationary sources such as factories and power plants, and mobile sources such as cars, planes, and trains are the major contributors of urban air pollution. Increasing air pollution around big cities not only threatens the health of humans, but also influences this planet by changing climate or by affecting Earth's ecosystems and biological diversity. Although there is a minor group of scientists that are skeptic about humans as a cause of this climate change, about 97% of actively publishing climate scientists agree on the tenets of anthropogenic climate change (ACC) [1]. The rapid climate change seen today is caused by greenhouse gases such as carbon dioxide and ozone. The global average temperature has risen by 0.74 °C the last 100 years with the increase of carbon dioxide concentration [2]. This climate change affects ecosystems directly by decreasing biodiversity, increasing carbonic acid in the ocean that negatively affects marine life, alters habitats, and affects migrations and life cycle of species [3]. Ozone can damage vegetation, impacting the growth of plants and trees, which in turn reduces the ability of plants to uptake CO_2 from the atmosphere. Pollution in the form of acids and acid-forming compounds, known as acid rain, could negatively affect regional ecology in both land and water systems. Acid deposition can damage forest directly or by changing the chemical and physical characteristics of the soil [4]. It also can kill fish and other aquatic life [4]. Among many air pollutants, nitrogen dioxide (NO_2), sulfur dioxide (SO_2), particulate matter (PM), and

ozone (O_3) are classified as major atmospheric pollutants that have adverse effects on human health [5].

In particular, there is a growing concern about rising level of nitrogen dioxide in fast-growing cities globally. The major sources of anthropogenic emissions of NO_2 are the combustion processes in stationary sources (heating, power generation) and in mobile sources (combustion engines in vehicles) [5]. During the high-temperature combustion, nitrogen and oxygen combines to produce nitric oxide (NO), which then transforms into nitrogen dioxide (NO_2) in reaction with ozone and oxygen. The NO_2 is then photolyzed by sunlight to reform NO (Equation (1.1)). The NO and NO_2 coexist in equilibrium in the atmosphere.

$$\mathrm{N_2 + O_2 \xrightarrow{\text{high combustion temperature}} 2NO} \tag{1.1}$$

$$\mathrm{NO + O_3 \rightarrow NO_2 + O_2} \quad \text{and} \quad \mathrm{2NO + O_2 \rightarrow 2NO_2}$$

$$\mathrm{NO_2 \xrightarrow{\text{sunlight}} NO + O}$$

The sum of NO and NO_2 is often called nitrogen oxides or "NOx" in atmospheric chemistry, and for this reason, the NOx concentration in urban areas and near major roadways is greater than ambient atmosphere.

NOx are known to have adverse effect on human and nature in multiple ways. It has direct effect on human health such as irritation on eye, nose, throat, and respiratory tract [4]. Severe exposure can result in pulmonary edema and diffuse lung injury, and continued exposure to high NO_2 can contribute to acute or chronic bronchitis [4]. On a larger scale, the NO_2 together with SO_2 is known as the major contributor to the acid rain,

forming nitric acid (HNO_3) and sulfuric acid (H_2SO_4) respectively, that threatens the natural and built environments alike (Equation (1.2)).

$$NO_2 + OH\cdot \rightarrow HNO_3 \quad (1.2)$$

$$SO_{2(g)} + OH\cdot \rightarrow HOSO_2\cdot$$

$$HOSO_2\cdot + O_2 \rightarrow HO_2\cdot + SO_3$$

$$SO_{3(g)} + H_2O \rightarrow H_2SO_4$$

Importantly, NO_2 is a key precursor of secondary pollutants such as photochemical smog and particulate matters [5]. Photochemical smog is a term used to describe air pollution that is a result of the chemical reaction of NO_2, sunlight, and volatile organic compounds (VOCs). For example, the oxygen atom broken down from NO_2 (Equation (1.1)) combines with O_2 to form most of tropospheric ozone (O_3), which is considered a powerful greenhouse gas that contributes to global warming (Equation (1.3)). Also, the reaction of NO_2 with VOCs produce peroxyacetyl nitrate (PAN), which forms an important fraction of particulate matter, another major air pollutant (Equation (1.4)).

$$O + O_2 \rightarrow O_3 \quad (1.3)$$

$$NO_2 + O_2 + \text{hydrocarbons} \xrightarrow{\text{sunlight}} CH_3CO - OO - NO_2 \quad (1.4)$$

The photochemical smog forms when these pollutants become concentrated in the air and remain stationary, such as during inversion, which not only causes impaired visibility but

also very harmful to respiratory tract and eyes. In addition to that, NOx absorb visible solar radiation, which results in impaired visibility and potentially affects global climate change [5].

Although the adverse effect of NOx are well-known, it was reported that the concentration of NOx do not show a tendency to decrease except in the United States, while the concentration of SO_2 has decreased in most parts of the world [5], driven by various national and international regulations. Specifically, the average NO_2 concentration in the United States has decreased 33% from 2001 to 2010 (Figure 1.1), but it often is higher in many of the large cities on all continents. Figure 1.2 illustrates the annual average NO_2 concentrations in selected cities worldwide. It should be noted that NO_2 level in many of the big cities exceed 40μg/m^3 (0.021ppm), which is WHO's guideline for air quality. Air pollution levels are normally higher in developing countries than in highly developed industrialized countries. The reason for this is because the NOx concentration is mainly related to mobile sources which are increasing, and there is decreasing demand on burning fossil fuel globally that produces SO_2.

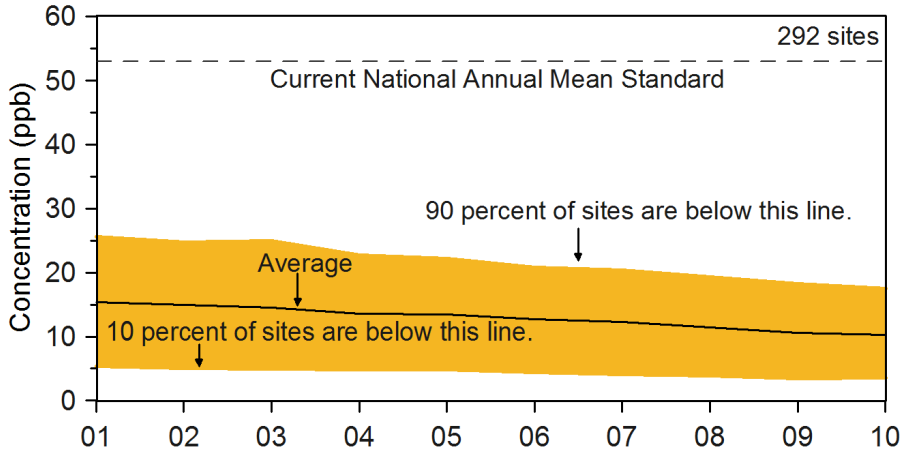

Figure 1.1—Annual average NO_2 concentration trend in the US, 2001-2010 [4]

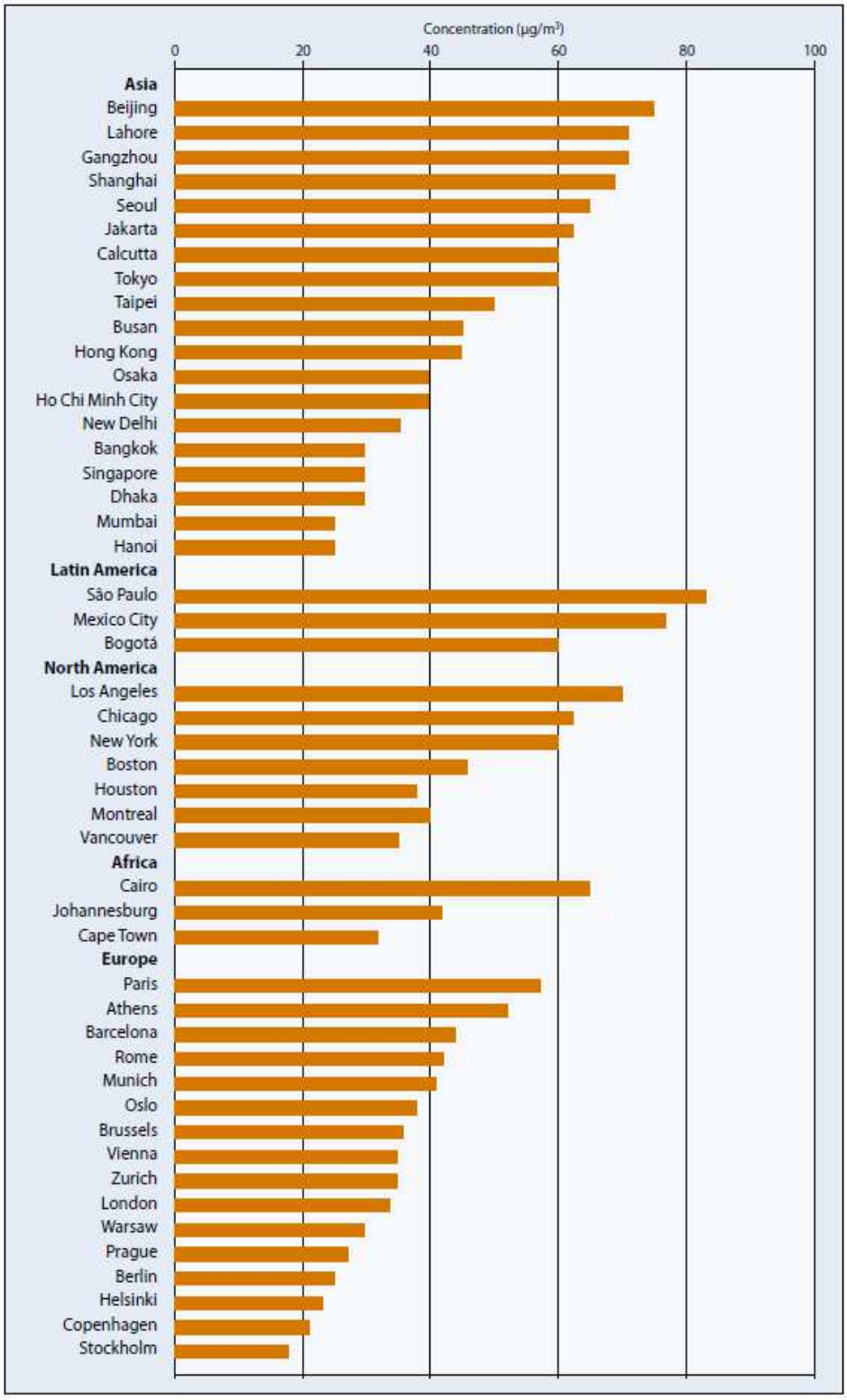

Figure 1.2—Annual average NO_2 concentrations in 2000-2005 reported from selected cities worldwide [5]

Despite significant effort to lower direct NO emissions through regulation in many countries, NO_2 concentration has been frequently exceeding the limit values on urban curbside stations [6]. Because automobiles are a major source of NOx, the higher levels of concentration occur at rush-hour near busy roads. It was recorded that hourly NO_2 concentration exceeded 940$\mu g/m^3$ (500 ppb) [7], which is far above the standard. In Atlanta, the annual concentration of NO_2 stays below 30ppb which is far below the standard [4], but it exceeds 1 hour standard once in a while near the roadways as experimentally measured.

Due to increasing understanding and concern regarding the rising NOx levels, regulation of NOx is generally increasing on a global scale, with several regions and countries taking the lead in setting lower limits in recent years. World Health Organization (WHO) has published "WHO air quality guidelines" that is updated in 2005 to protect public health [5]. This document offers guidance to policy makers on four most common air pollutants – nitrogen dioxide, sulfur dioxide, particulate matter, and ozone – in order to reduce their health effects. Here, NO_2 is stated to have an adverse effect on health by direct exposure at both short-term and long-term exposure, and also by secondary pollutants. The guidelines for annual and 1-hour mean are summarized in Table 1.1. In the US, United States Environmental Protection Agency (USEPA) recently strengthened the health-based National Ambient Air Quality Standards (NAAQS) for nitrogen dioxide on January 2010, setting a new 1-hour NO_2 standard at the level of 100 ppb, retaining the current annual average standard of 53ppb. This change was made based on current scientific evidence that short-term NO_2 exposure, from 30 minutes to 24 hours, could exacerbate respiratory illnesses and symptoms including asthma. This new standard

was prepared to protect populations, particularly people with asthma, children and the elderly. The short-term standard is expected to be applied near major roadways in urban areas at peak times, where the NOx concentration can be 30 to 100 percent higher than away from major roads. Most of the European countries follow air quality standards set by "European Commission – Environment" where the limit value for NO_2 has been enforced since January 2010. Similar air quality standards can be found from other countries and they are summarized in Table 1.1.

Table 1.1—Air quality standards for NO_2 in several countries

	WHO	USA	EU	Korea	Japan
1 hour	200 μg/m^3 (106 ppb)	100 ppb	200 μg/m^3 (106 ppb)	100 ppb	-
1 day	-	-	-	60 ppb	40-60 ppb
1 year	40 μg/m^3 (21 ppb)	53 ppb	40 μg/m^3 (21 ppb)	30 ppb	-

On one way of reducing the NOx concentration in the atmosphere, titanium dioxide (TiO_2) has drawn much attention to researchers due to its strong oxidizing capability. Titanium dioxide is the most well known photocatalytic semiconductor which has an electronic structure characterized by its valence band (VB) and conduction band (CB) energy positions. The detailed mechanism for the photocatalytic reactions is going to be introduced later in Chapter 2. It is generally known that water, oxygen, and UV light are required in order for the photocatalytic oxidation reactions to occur [8]. These reactions enable TiO_2 to oxidize or decompose NOx, organic, and small inorganic compounds.

In addition to photocatalytic properties, it is chemically and biologically inert, non-toxic, and relatively low cost [8, 9], which makes it an accessible material for general applications. The applications of nano-anatase TiO_2 include self-cleaning, air and water purification, self-sterilizing, and anti-fogging surfaces [10].

1.2 TiO_2 Used in Construction Materials – Sustainable Development

The interest in use of titanium dioxide in construction materials stemmed initially from its white color and therefore for its ability to be used in a wide range of products and applications. However, the recognition of certain forms of titanium dioxide [11] as a photocatalytic material has widened its application. The study of the usage of TiO_2 in construction materials as a photocatalytic material initiated from the early 1990s [12]. The early studies and applications focused on its self cleaning ability, which enabled the facades of buildings to remain clean from stains [13]. Today, with increasing global awareness and regulation of air pollution, interest in the smog-abating property of photocatalytic materials is increasing. TiO_2 is considered one way of solving pollution by a passive but an effective way, as demonstrated in several laboratory studies [14, 15] and by some pilot projects [16, 17]. This relatively new technology is already being used in some of the countries, commercially sold as photocatalytic cement (Italcementi Group), photocatalytic pavement [18], self-cleaning tiles (TOTO) and self-cleaning glass (Nippon Sheet Glass). Along with smog oxidizing properties, there are active discussions on hydrophilic and hydrophobic characteristics of TiO_2 [10, 12, 19], because it can enhance self-cleaning process or air purification by removing residue from the photocatalytic activity.

1.3 Research Motivation

Prior research has examined the photocatalytic properties of TiO_2 itself [8, 10, 20], as well as TiO_2-containing cement-based materials [17, 21, 22]. The majority of this effort has been on characterizing and enhancing the photocatalytic efficiency.

However, relatively little research was performed to assess the potential impact of the photocatalytic reaction on the "parent" or "host" material. In this research, the focus is on the effect of photocatalysis on the composition, structure, and properties of cementitious materials, which contain titania nanoparticles at early and late ages. Fundamental examinations on the addition of these chemically non-reactive nanoparticles to cement-based materials and the effect of the TiO_2 on the long term durability of cement-based materials must be thoroughly performed to demonstrate their suitability for long-term use in the field. The high surface of nanoparticles could alter early age properties of cementitious materials, such as setting time, dimensional stability, and hydration rate. Also, since the process of degradation involves chemical changes, there could be some effects of photocatalysis on cementitious substrate which could eventually degrade its mechanical properties or change its oxidation power. Although cement is known to efficiently adsorb NOx in the atmosphere to cement surface, a detailed study should be conducted. Considering that this relatively new technology has been started to be used in some parts of the world such as in Europe and in Japan, careful fundamental examination should be performed in order to better utilize this technology.

1.4 Research Objectives

The global objectives of this research are to understand the effect of chemically non-reactive nano-anatase titanium dioxide on early age hydration of cement-based materials, and to understand durability of titanium dioxide containing cementitious materials undergoing photocatalysis.

Five detailed main objectives are:

1) To understand the effect of chemically inert nano-anatase titanium dioxide on early age hydration of cement using different techniques, which include isothermal calorimetry, chemical shrinkage, Vicat setting time, compressive strength, and Vickers microhardness indentations. Titanium dioxides from two different manufacturers are utilized at addition level of 5% to 15%. The results are compared to neat control cement paste.

2) To understand the effect of TiO_2 nanoparticles on the hydration rate of pure phase C_3S and C_2S and to understand early age hydration kinetics of TiO_2-cement by mathematical modeling using pure C_3S, as a substitute for cement. “Avrami nucleation model” and “boundary nucleation model” are used to describe the kinetics of early hydration. The effect of the addition of large surface area TiO_2 on hydration kinetics is examined and explained using the models.

3) To understand and compare the photocatalytic efficiency and NOx binding capacity of TiO_2-containing cementitious materials under both nitric oxide and nitrogen dioxide. Photocatalytic efficiency experiments are performed in a chamber, where cement paste samples are subjected to a constant UV light and a constant flow of NO or NO_2. For measuring NOx binding capacity, samples are exposed to either NO or NO_2 gases without UV irradiation. The results of the NO and NO_2 gases are compared.

4) To understand characteristics of TiO_2-cement after cycles of NOx and UV exposure accompanied by wetting and drying. First, the photocatalytic efficiency is measured during the course of multiple cycling to examine the efficiency after long-term environmental exposure. Second, the surfaces of TiO_2-cement tiles that are exposed to the specific environmental condition are examined by scanning electron microscopy, x-ray diffraction analysis, microhardness indentation technique, and surface roughness. Any effects due to extensive exposure condition are discussed.

5) To understand the potential effect of the final NOx oxidation products, especially calcium nitrate salts, on salt crystallization damage to cement-based materials. Mortar bars at varying w/c and containing different percentages of TiO_2 nanoparticles are partially submerged in calcium nitrate salt solution in a low humidity sealed chamber. The results are compared to samples subjected to deionized water and sodium sulfate solution, and the extent of damage is discussed in relation to microstructure of mortar samples.

1.5 Organization of Dissertation

The structure of the dissertation is outlined as follows:

- Chapter 2 presents a thorough literature review on the background of nanotechnology in cement and concrete research, photocatalytic cement, hydration modeling, existing standards for NOx removal testing, and topics related to long-term durability.

- Chapter 3 presents effects of addition of titanium nanoparticles on the properties of cementitious materials. Results from isothermal calorimetry, chemical shrinkage, setting time, compressive strength, and microhardness are presented.

- Chapter 4 presents the results of the rate of hydration study when titanium nanoparticles are added to pure tricalcium silicate and dicalcium silicate. The early hydration kinetics of C_3S are examined by mathematical modeling and applied to the rate of hydration data.

- Chapter 5 presents the results from photocatalytic oxidation experiment, where samples are exposed to either NO or NO_2 gases. Photocatalytic efficiency and NOx binding property of cement paste samples are compared when NO and NO_2 gases were utilized.

- Chapter 6 presents the durability of TiO_2-cement after cycles of NOx-wetting-drying exposure. The exposed surfaces are examined with various techniques for possible degradation, and photocatalytic efficiency throughout the cycles is presented.

- Chapter 7 presents the effect of NOx oxidation final product, calcium nitrate salt, on the crystallization damage of cement-based materials. The results are compared to when sodium sulfate salt solution and deionized water are utilized.

- Chapter 8 provides a summary of the research performed and its key conclusions. Further research is recommended based upon the outcomes of the current research.

Each chapter contains its own reference section to improve the readability of the dissertation.

1.6 References

1. Anderegg, W.R.L., et al., *Expert credibility in climate change.* Proceedings of the National Academy of Sciences of the United States of America, 2010. **107**(27): p. 12107-12109.

2. Solomon, S., et al., *Climate Change 2007: The Physical Science Basis*. 2007, Cambridge, UK and New York, NY: Cambridge University Press.

3. Parry, M.L., et al., *Climate Change 2007: Impacts, Adaptation and Vulnerability : Contribution of Working Group II to the Fourth Assessment Report of the Intergovernmental Panel on Climate Change*. 2007, Cambridge, UK: Cambridge University Press.

4. USEPA. *United States Environmental Protection Agency*. Available from: http://www.epa.gov/.

5. WHO, *Air quality guidelines, Global update 2005*. World Health Organization, 2005.

6. Carslaw, D.C., S.D. Beevers, and M.C. Bell, *Risks of exceeding the hourly EU limit value for nitrogen dioxide resulting from increased road transport emissions*

of primary nitrogen dioxide. Atmospheric Environment, 2007. **41**(10): p. 2073-2082.

7. Hickman AJ, Bevan MG, and C. DM, *Atmospheric pollution from vehicle emissions at four sites in Coventry*. Crowthorne, Department of the Environment, 1976. **Report No. CR 695**.

8. Carp, O., C.L. Huisman, and A. Reller, *Photoinduced reactivity of titanium dioxide.* Progress in Solid State Chemistry, 2004. **32**(1-2): p. 33-177.

9. Tobaldi, D.M., et al., *Photocatalytic activity for exposed building materials.* Journal of the European Ceramic Society, 2008. **28**(14): p. 2645-2652.

10. Fujishima, A., X.T. Zhang, and D.A. Tryk, *TiO_2 photocatalysis and related surface phenomena.* Surface Science Reports, 2008. **63**(12): p. 515-582.

11. Fujishima, A., K. Hashimoto, and T. Watanabe, *TiO_2 photocatalysis. Fundamentals and applications*. 1st ed. ed. 1999, Tokyo: BKC.

12. Chen, J. and C.S. Poon, *Photocatalytic construction and building materials: From fundamentals to applications.* Building and Environment, 2009. **44**(9): p. 1899-1906.

13. Cassar, L., et al. *White cement for architectural concrete, possessing photocatalytic properties*. in *11th Int. Congr. on the Chemistry of Cement*, 2003. Durban.

14. Poon, C.S. and E. Cheung, *NO removal efficiency of photocatalytic paving blocks prepared with recycled materials.* Construction and Building Materials, 2007. **21**(8): p. 1746-1753.

15. Husken, G., M. Hunger, and H. Brouwers. *Comparative study on cementitious products containing titanium dioxide as photo-catalyst*. in *RILEM Int. Symp. on Photocatalysis, Environment and Construction Materials*, 2007. Italy.

16. Beeldens, A. *Air purification by road materials: Results of the test project in Antwerp*. in *International RILEM Symposium on Photocatalysis, Environment, and Construction Materials*, 2007. Florence, Italy.

17. Maggos, T., et al., *Photocatalytic degradation of NO_x in a pilot street canyon configuration using TiO_2-mortar panels.* Environmental Monitoring and Assessment, 2008. **136**(1-3): p. 35-44.

18. Fujishima, A. and X.T. Zhang, *Titanium dioxide photocatalysis: present situation and future approaches.* Comptes Rendus Chimie, 2006. **9**(5-6): p. 750-760.

19. Sakai, N., et al., *Quantitative evaluation of the photoinduced hydrophilic conversion properties of TiO_2 thin film surfaces by the reciprocal of contact angle.* Journal of Physical Chemistry B, 2003. **107**(4): p. 1028-1035.

20. Cappelletti, G., et al., *Photodegradation of Pollutants in Air: Enhanced Properties of Nano-TiO_2 Prepared by Ultrasound.* Nanoscale Research Letters, 2009. **4**(2): p. 97-105.

21. Chen, J. and C.S. Poon, *Photocatalytic activity of titanium dioxide modified concrete materials - Influence of utilizing recycled glass cullets as aggregates.* Journal of Environmental Management, 2009. **90**(11): p. 3436-3442.

22. Ramirez, A.M., et al., *Titanium dioxide coated cementitious materials for air purifying purposes: Preparation, characterization and toluene removal potential.* Building and Environment, 2010. **45**(4): p. 832-838.

CHAPTER 2

LITERATURE REVIEW

2.1 Use of Nanotechnology in Cement and Concrete

Nanotechnology is commonly defined as the understanding, control, and restructuring of matter on the order of nanometers (i.e., less than 100nm) to create materials with fundamentally new properties and functions [23]. There have been a lot of efforts in physics, chemistry, and biology in the area of nanotechnology [24] since the concept of nanotechnology was introduced by Feynman in 1959 [25]. In recent years, interest in nanotechnology in cement-based materials is increasing [24, 26-37]. Cement and concrete are essentially composed of different nano/micro size crystals and nanoscale amorphous phase, where there is a huge potential that the bulk material properties be modified [38]. This section reviews recent development of nanotechnology in cement and concrete research.

2.1.1 Definition of Nanotechnology in Cement and Concrete

The nanoscience and nano-engineering (or nanomodification) of concrete are the terms that are generally used in the nanotechnology of cement and concrete research [24]. Sanchez et al., in their review paper, defined the two terms as below [24].

> *Nanoscience deals with the measurement and characterization of the nano and microscale structure of cement-based materials to better understand how this structure*

affects macroscale properties and performance through the use of advanced characterization techniques and atomistic or molecular level modeling.

Nano-engineering encompasses the techniques of manipulation of the structure at the nanometer scale to develop a new generation of tailored, multifunctional, cementitious composites with superior mechanical performance and durability potentially having a range of novel properties such as: low electrical resistivity, self-sensing capabilities, self-cleaning, self-healing, high ductility, and self-control of cracks.

In this chapter, a thorough review of nano-engineering in cement and concrete research is presented. The term "nanotechnology" is going to be used for "nano-engineering" for convenience.

2.1.2 Nano-Engineering of Cement and Concrete

Nano-engineering, or nanomodification, of cement-based materials implies adding nano-size cement additives in the mixing procedure, to enhance and control some of the properties of the material, including hydration, performance, and degradation process. Depending on the desired final properties, the additives can be classified as nanoparticles, superplasticizers, or nanoreinforcements. For the scope of this dissertation, only the literature reviews on nanoparticles are going to be presented.

Nanoparticles have tremendous surface area to volume ratio, which potentially could affect chemical reaction of hydrating cement. There have been studies with nano-silica (nano-SiO_2) [26-31], nano-titanium dioxide (nano-TiO_2) [30, 32, 33], nano-iron (nano-Fe_2O_3) [26], nano-alumina (nano-Al_2O_3) [31, 34], and some other nanoparticles such as nanoclay [35, 36] and nanosized cement particles [37]. These nanoparticles could

promote cement hydration by adding additional surface area for hydration products to form, could enhance mechanical strength by nanoreinforcement, or could act as a nano-filler, which densifies the microstructure and the ITZ, leading to lower porosity. Among others, nano-silica has been the most studied. It has been found that nano-silica improves concrete strength and workability [27]. It was also shown that the addition of nano-SiO_2 accelerate early hydration reactions by adding high surface area [29]. Also, it improves the microstructure due to filler effect and activates pozzolanic reactions [27]. Nano-TiO_2 is known for its photocatalytic properties including NOx oxidation [14, 15, 17, 39-42], removal of volatile organic compounds [12, 43, 44], self-cleaning [12, 39, 41, 45-47], and biocidal characteristics [48, 49]. Due to these novel functionalities, it has been used with construction materials such as cement-based materials. In addition, due to its nano-size, it can accelerate the early-age hydration of portland cement [50]. Also, it was shown to increase compressive and flexural strengths of concrete [30, 33]. Nano-Fe_2O_3 was reported to improve strength and flexural strengths of concrete [51]. Also, it was reported to provide self-monitoring capabilities of cement mortar [51]. Nazari et al. examined abrasion resistance of concrete when nano-Al_2O_3 nanoparticles are embedded, and concluded that the abrasion resistance was improved while compressive strength were not affected [31]. In most of the cases where nanoparticles are used with cement-based materials, improved mechanical properties was found out due to its physical small size and high surface area, in addition to showing their unique functionality. The nano-modification of cement-based materials is currently an active research area.

Although the use of nano-materials in cementitious materials holds great advantages, problems related to effective dispersion, lowering cost, and human health still need to be resolved [27, 52, 53].

2.1.3 Nanotechnology in Terms of Sustainable Development

Nanotechnology might hold the key to a sustainable development. Nano-TiO_2, introduced in section 2.1.2, has photocatalytic properties, which makes it a promising material in reducing atmospheric harmful nitrogen oxides as well as volatile organic compounds. This novel application holds potential as a sustainable development, along with nanomodification of cementitious materials. Detailed literature reviews on photocatalytic cements are presented in section 2.2. In addition to that, nano-TiO_2 could also be used to accelerate C_2S hydration [52]. This could contribute to sustainability in terms of lower CO_2 emissions by ameliorating cement compositions. Nano-sized cement particles or nanobinders have been proposed as one way of improving cement performance while reducing atmospheric CO_2 emissions during cement production by lowering clinkering temperature [54].

2.2 Photocatalytic Cement

Cement has been often selected as a substrate for the TiO_2 for infrastructure applications, since TiO_2 has limited capacity for adsorbing or storing organic or inorganic substances. Photocatalytic cement is essentially any cement-based materials that contain titanium dioxide (TiO_2) particles. TiO_2, also known as titania, is responsible for the photocatalytic oxidation of various components in the atmosphere or in the water. In

order to study the photocatalytic cement, it is crucial to understand the material properties and underlying chemical processes that take place on the TiO_2 surface.

2.2.1 Titanium Dioxide

2.2.1.1 History

Titanium dioxide is a naturally occurring oxide of titanium. The use of this material initiated as a white pigment in the early 20^{th} century due to its high refractive index, replacing toxic lead oxides [8]. Over half of its total production is used to make paints as a white pigment (51% of total production). Other industry applications as white pigment include plastic, paper, cosmetic products, medicine, food coloring, and many others [8]. The photocatalytic properties were later discovered and named as "Honda-Fujishima effect," published in *Nature* [55]. Most of the studies are focused on its photocatalytic efficiency under various conditions. These unique properties have widened the application of TiO_2 to smog abatement [14, 15, 17, 39-42], self-cleaning [12, 39, 41, 45-47], biocidal capacities [48, 49], and indoor air quality enhancement by volatile organic compounds (VOCs) removal [12, 43, 44]. Moreover, the use of TiO_2 received a great attention due to its chemical/biological stability, ease of production, relatively low cost, and being safe for the environment [8].

2.2.1.2 Crystal Structures

In general, there are three main types of crystal structures of TiO_2 found in nature, which are rutile (tetragonal), anatase (tetragonal), and brookite (orthorhombic) (Figure

2.1) [8, 10]. Some other high-pressure crystal structures can be synthesized having PbO_2 structure, hollandite structure, baddeleyite structure, and cotunnite structure [8, 56]. It is known that the rutile is the most stable phase above particle size of 35nm and anatase is the most stable phase for particles less than 11nm [57]. These crystal structures have different photo reactivity, and anatase phase is known to be the most photocatalytically reactive among them followed by rutile, although the reasons behind have been on debate. Recently, Ahmed et al. proposed an explanation why the anatase nanoparticles exhibit higher photocatalytic activities than rutile [58-60]. There is also an indication that an optimal anatase-to-rutile ratio exists for the photoreactivity of TiO_2 [61]. Thus, for the photocatalysis applications, the anatase type of TiO_2 is the most widely used. Also, due to easy charge transfer on the surface of nano-sized particles, which makes the reaction efficient [8, 18], nanoparticles of anatase TiO_2 are commercially produced and widely used.

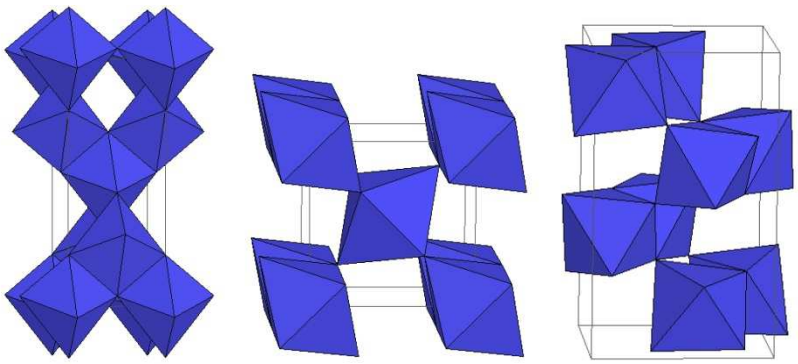

Figure 2.1—Crystal structures of TiO_2 (a) anatase, (b) rutile, and (c) brookite

TiO_2 is usually sold in the form of powder, but it is also sold in the form of sol or slurry [62, 63]. Because of the health related problems that the nanoparticles might cause,

such as respiratory or skin irritations, nano-TiO_2 powder is usually sold in the form of agglomerates of mean size of 1~2 μm.

2.2.1.3 Photocatalytic Oxidation Reaction

TiO_2 is known as one of the semiconductors, and such a property defines many of the unique characteristics of TiO_2 including photocatalysis. All photoinduced phenomena of TiO_2 including photocatalysis, photovoltaic solar cell, or superhydrophilicity are initiated when sufficient energy is absorbed by TiO_2. TiO_2 has an electronic structure characterized by valence band (VB) and conduction band (CB) energy. The energy difference between the two is called "band gap energy," and it is known to be 3.20 eV in case of bulk anatase TiO_2 [64]. When a photon that has higher energy than the band gap is in direct contact with TiO_2, an electron (e-) is excited from the VB to the CB, leaving a hole (h+) behind. This energy-rich electron-hole pair (e^--h^+) can be used electronically, chemically, or to change the properties of the catalyst surface [8], as well as takes part in photocatalytic oxidation and reduction reactions [22]. The band gap energy of TiO_2 corresponds to absorption threshold of 384 nm wavelength, which is near UV light range (360-380 nm). As the UV light is irradiated, reduction occurs at the CB and oxidation occurs at the VB. During these chain of chemical reactions, highly reactive superoxide radical-anions (O_2^-) and hydroxyl radicals (•OH) are expected to form on the surface of TiO_2 nanoparticles, which then decomposes organic and inorganic pollutants as well as micro-organisms adsorbed on the surface [22]. The schematic that describes these reactions occurring on the surface of TiO_2 oxidizing nitrogen dioxide is shown in Figure 2.2, reproduced from [40].

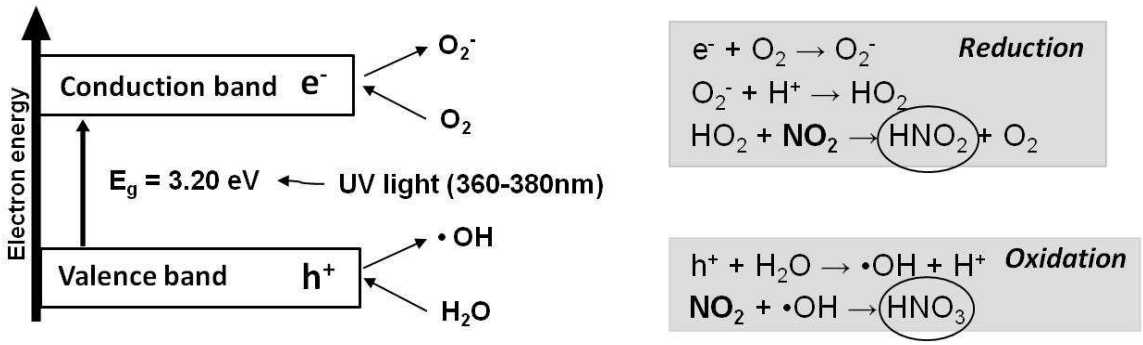

Figure 2.2—Mechanism of photocatalytic TiO_2 [40]

2.2.2 NOx Oxidation Reactions

Focusing on the aspect of air quality improvement in outdoor environment, TiO_2 has been known to effectively oxidize nitrogen oxides (NOx=NO+NO_2). Especially, NO_2 is classified as one of the major air pollutants these days, participating in the formation of photochemical smog and ozone (O_3), as well as threatening human health [5]. Many mechanisms for the NOx oxidation reaction on TiO_2 particle were proposed. Dalton proposed that hydroxyl radicals oxidize NO to NO_2 and NO_2 to NO_3^-, while active oxygen oxidizes NOx to NO_3^- [40]. Devahasdin et al. proposed a lengthy mechanism, essentially saying that the oxidation process involves hydroxyl radical and that the NO is first converted to HNO_2, which is converted to NO_2, and then finally converted to HNO_3. They suggested that the reverse reaction is also viable when the equilibrium is reached [65]. In other study, it was proposed that NO_2 is converted to HNO_3 and NO is converted to HNO_2 by hydroxyl radicals [66]. Anpo reported some other perspectives, that the NO is decomposed into N_2, O_2, and N_2O during the photocatalytic degradation [67]. Although many researchers have proposed mechanisms for the NOx oxidation, the detailed

mechanism is still not fully established. However, the set of chemical reactions proposed by Ndour [68] gives general understanding on the mechanism (Equation (2.1)).

$$\text{On valence band, } h_{vb}^{+} + H_2O \rightarrow \bullet OH + H^{+} \tag{2.1}$$

$$NO_2 + \bullet OH \rightarrow HNO_3$$

$$\text{On conduction band, } e_{cb}^{-} + O_2 \rightarrow O_2^{-}$$

$$NO_2 + O_2^{-} + H^{+} \rightarrow HNO_2 + O_2$$

Leading to the following postulated catalytic net reaction:

$$2NO_2 + H_2O \xrightarrow{+hv,TiO_2} HNO_2 + HNO_3$$

According to Ndour and many others, it is generally accepted that the final products of NOx oxidation are nitric acid (HNO_3) and nitrous acid (HNO_2 or HONO) [65, 69-71]. These final products are believed to accumulate on the TiO_2 surface, inhibiting the photocatalytic reaction. However, these are soluble and can easily be washed away by water, such as in rain, and the photocatalytic activity is restored.

It is generally understood that the oxidation reaction converts atmospheric "harmful" NO and NO_2 to a form that is implicitly "safe" substances. This, however, might not hold true, if it is used with cement-based materials. Nitric acid or nitrous acid, the final products of the reaction, could take part in chemical reactions with cementitious substrate and affect durability of the material. Apart from the good photocatalytic NOx oxidation properties, a thorough study is needed in terms of any effect on cementitious substrate.

2.3 Early Age Hydration

2.3.1 Effect of Fine Additives on Cement Hydration

Addition of TiO_2 nanoparticles to cement-based materials is getting interest due to its air purifying properties. Researchers have shown that the photocatalytic activity is superior in nano-crystalline TiO_2 [8, 18], and that it exhibits maximum efficiency in anatase phase compared to rutile or brookite phase [58-60]. Thus, for the photocatalytic applications, the TiO_2 powder is produced in anatase nanoparticles and often in agglomerated form due to possible health related problems. These nanoparticles are often added to cementitious materials during mixing. It being a nano-material, the effect of the addition of such large surface area filler could directly modify early age hydration kinetics, affecting setting time, dimensional stability, and strength development.

There have been studies on the addition of fillers to cement and their effect on early-age hydration of portland cement. The fillers for cementitious system can be categorized by their particle size and reactivity. Whether they are hydraulic or non-reactive, the surface of the fine fillers has been shown to provide sites for nucleation of cement hydration products (C-S-H) and catalyzes the reaction by reducing the energy barrier [72]. The effectiveness of this catalysis depends on fineness and dosage of the filler [72]. In addition, other phenomena may occur including water absorption by the particles, interactions with surface treatments, and reaction of materials previously presumed to be inert. Some researchers investigated the effect of addition of micro-sized particles. Zelic et al. concluded that silica fume that has surface area of $18 m^2/g$ accelerated the early cement hydration by nucleation effect due to added surface area and not by pozzolanic activity [73]. Gutteridge et al. compared non-hydraulic particles (rutile

(0.5μm)) to hydraulic particles (pulverized fuel ash, slag, silica) and concluded that the degree of hydration was enhanced due to larger specific surface added [74, 75]. Limestone powder was also shown to increase early hydration rate of cement [76]. Similar results were found from submicro-sized particles from various researchers. Kadri et al. investigated various submicro-sized particles, such as alumina (0.8μm, 1.5μm, and 63μm), silica fume (0.15μm), quartz (2.2μm), and calcium carbonate (0.07μm), and concluded that the fillers, either chemically inert or active, act as heterogeneous nucleation sites and the rate of hydration is accelerated with increasing fineness [77]. More recently, a number of researchers examined the effect of addition of nanoparticles to cement-based materials. The literature reviews on the effect of addition of nanoparticles are addressed earlier in this chapter in 2.1.2.

From the above, researchers have noted an acceleration of cement hydration when fine fillers are added to cement, providing nucleation sites for the hydration products to form. However, most of the fine fillers that are previously examined react chemically to some extent in the cement hydration process, contributing to cement hydration. Also, many of the fillers used were micron to submicron size, much larger than the nano-TiO_2, used for the photocatalytic cement. Considering that the TiO_2 act as chemically non-reactive filler which does not participate in the hydraulic reaction of portland cement, and also having nano-scale, there needs to be a study that directly focuses on the effect of non-reactive nano-filler on cement hydration.

On the other hand, addition of fine non-reactive filler, such as TiO_2 particles, to cement modifies the hydration rate primarily due to dilution, modification of particle size distribution and heterogeneous nucleation [72]. For increasing dosage rates of chemically

inert filler (when used as a partial replacement of cement), the effective water-to-cement ratio (w/c) increases and the effective cement content decreases as a result of dilution effect, when water-to-solids ratio (w/s) is kept constant. The modification of particle size distribution due to chemically inert filler addition might change the system porosity. Added surface area by the fine fillers provide heterogeneous nucleation sites for the hydration products. While dilution effect decreases the hydration rate of cement, added nucleation sites contributes to the early cement hydration. It is crucial to know the optimal total surface area and dosage of fine inert fillers in cement to tailor the hydration reaction mechanism.

2.3.2 Early Age Hydration Mathematical Models

The addition of TiO_2 nanoparticles to cement has been experimentally proven by the author to accelerate early hydration reaction of cementitious materials. Despite the practical importance of the kinetics of cement hydration, detailed early age reactions of cement-based materials remain imperfectly understood [78-80]. Several mathematical models have been suggested to characterize the hydration kinetics of the principal components of portland cement such as C_3S and C_2S. Here, the “Avrami nucleation and growth model” [81-83] (sometime also denoted as the “JMAK” model [84]) and the “boundary nucleation model” (BN model) [85] will be considered.

2.3.2.1 Avrami Nucleation and Growth Model

Among others, the Avrami nucleation and growth model [81-83] has been most widely accepted to describe the early age hydration rate for tricalcium silicate [86-89]. The theory was first treated by Kolmogorov [90], Johnson and Mehl [91], and Avrami [81-83] to explain the kinetics of phase change of metals. The main assumptions made were that the new phase is nucleated by germ nuclei and that the grain centers of the new phase are randomly distributed throughout the matrix.

Consider that nucleation is spatially random and nuclei grow in a constant linear growth rate, G, in any direction forming a sphere. This sphere will have a volume of $4\pi/3G^3(t-\tau)^3$, where t is time since the start of the total reaction and τ is the time at which the particular region nucleated. The "extended" volume fraction, X^e, of all the nuclei can be found by summing the individual regions, which can be expressed as Equation (2.2).

$$X^e = \frac{4\pi}{3}\int_{\tau=0}^{t} I_v G^3 (t-\tau)^3 \, d\tau \tag{2.2}$$

Here, I_v is the rate of nucleation per unit of untransformed volume. As the nucleation and growth process continues, those growing regions will impinge on each other, forming a common interface over which there is no growth. Considering impingement, the relationship between the "true" volume, X, and the "extended" volume fraction can be written as Equation (2.3).

$$X^e = -\ln(1-X) \tag{2.3}$$

Assuming that the nucleation rate, I_v, is constant with time, a new equation can be derived from Equation (2.2) and (2.3), shown in Equation (2.4):

$$X = 1 - \exp\left(\frac{-\pi G^3 I_v}{3} t^4\right) \rightarrow X = 1 - \exp\left[(-k_{avr}t)^n\right] \quad (2.4)$$

where k_{avr} is an effective rate constant and the exponent n should be between 3 and 4. The rate of transformation can be obtained by differentiating Equation (2.4). For direct application to rate data, such as that obtained from isothermal calorimetry, new parameters need to be introduced. The hydration rate, R, can then be expressed as Equation (2.5):

$$R = \dot{A} n k_{avr}^n (t - t_0)^{n-1} \exp\left(-[k_{avr}(t - t_0)]^n\right) \quad (2.5)$$

where Ȧ is a normalization constant and t_0 is a delay between the time of mixing and the time of start of nucleation and growth kinetics.

Due to its simple mathematical form, the theory has been widely adapted for C_3S hydration [86-89]. However, the heterogeneous nucleation process that occurs during cement hydration may not be best described by a random or homogeneous nucleation assumption [92, 93]. Also, this theory assumes that the rate of diffusion of reactants does not affect growth rate, which might not hold true at later hydration age. These are considered shortcomings of the Avrami model at the later stage of hydration, where the hydration rate is controlled by diffusion rather than nucleation and growth.

2.3.2.2 Boundary Nucleation Model

Thomas [92] recently proposed a mathematical C_3S hydration model based on the boundary nucleation model (BN model) developed by Cahn [85]. The theory, which was used originally to describe a solid-solid phase transformation in a polycrystalline material, has been shown to give a better approximation of early age hydration kinetics of C_3S than the Avrami model. The key difference in the assumption is that nucleation is permitted to occur only on grain boundaries, unlike the Avrami model which assumes that nucleation occurs at randomly distributed locations everywhere within the untransformed volume. This, applying to cement hydration, implies that hydration products start to grow on available surfaces such as unhydrated cement and fillers. Experimental observations of the outward growth of hydration products from the hydrating cement grains [94, 95] confirm heterogeneous nucleation. This model was developed such that the nucleation and growth kinetics is adopted under the conditions of grain boundary nucleation.

Consider a single planar boundary and assume nucleation occurs at random locations on this boundary. Assume another plane parallel to this plane at a distance y. The new phase grows as a hemisphere on the initial boundary. When this hemisphere intersects the other plane, a circular area with $\pi(G^2(t-\tau)^2-y^2)$ is created. The extended area of the intersection between the plane and all regions nucleated on the grain boundary, denoted Y^e can be calculated as,

$$Y^e = \pi \int_0^{t-\frac{y}{G}} I_B (G^2(t-\tau)^2 - y^2) d\tau \quad (2.6)$$

$$\rightarrow \quad Y^e = \pi \frac{I_B}{3} G^2 t^3 \left[1 - \frac{3y^2}{G^2 t^2} + \frac{2y^3}{G^3 t^3}\right]$$

where I_B is the nucleation rate per unit area of boundary. In order to calculate true area of intersection, Y, under the assumption that nucleation sites are randomly distributed on the boundary, the relationship Y=1- exp ($-Y^e$) is applied to Equation (2.6). The volume fraction of hydrated phase can be found by integrating Y over the perpendicular distance y between the plane and the boundary, presented in Equation (2.7):

$$2 \int_0^{\infty} O_v^b Y \, dy = 2 O_v^b \int_0^{Gt} [1 - \exp(-Y^e)] dy \quad (2.7)$$

Where O_v^b is the boundary area of a single plane. Now, taking account that there are large number of grain boundaries with total boundary area of O_v^B and considering impingement from regions originating on different boundaries, Equation (2.4) is applied to Equation (2.7), and the true hydrated volume, X, can be expressed as Equation (2.8).

$$X = 1 - \exp\left[-2 O_v^B \int_0^{Gt} (1 - \exp(1 - Y^e)) dy\right] \quad (2.8)$$

The hydration rate can be numerically differentiating Equation (2.8) with respect to time.

The BN model accounts for effect of the surface area of the starting material, which in the case of hydrating cement or C_3S is known to have a strong effect on the hydration kinetics [96, 97]. However, the BN model also does not reflect the later

hydration stage where the rate of hydration is controlled by diffusion rather than nucleation and growth.

2.4 Photocatalytic Nitrogen Oxides Oxidation Experiments

As the use of photocatalytic materials increase, standardized test methods have been developed. Although not all researchers directly implement these standards, it is helpful to review these as a starting point, and to modify them to meet a specific need when planning an experiment.

2.4.1 NOx Removal Test Standards

2.4.1.1 JIS R 1701-1

The JIS R 1701-1 standard entitled “Fine ceramics (advanced ceramics, advanced technical ceramics) – Test method for air purification performance of photocatalytic materials – Part 1: Removal of nitric oxide [98]” can be considered as a pioneer standard, established in Japan in 2004, that can be used for cement-based materials for NO removal. Japanese researchers are one of the earliest to adopt TiO_2 to construction materials, and it is not surprising that the standard was first made in this country.

In this method, a continuous flow of testing gas passes through a reactor where samples are placed. UV light is irradiated on top of the reactor, which the top part is UV transparent. The NO concentration is measured by a chemiluminescent NOx analyzer at the output of the reactor. After the photocatalytic experiment, elution test is performed on the test piece to measure nitrate and nitrite ions produced during the reaction. It should be

noted that in this standard, any results relating to changes in the test gas is calculated based on the elution test results.

This test utilizes only NO for the experiment at 1ppm concentration. The specified temperature is 25.0°C ± 2.5°C. Flow rate of the test gas should be 3.0 L/min and relative humidity of 50% is specified. A fluorescent lamp that has wavelength range from 300nm to 400nm is used for the UV light source and the irradiance at the sample surface shall be 10 W/m^2. Sample photocatalytic sample should have dimensions of 49.5mm ± 0.5mm wide and 99.5mm ± 0.5mm long flat plate. The distance between the sample surface and the window plate should be 5mm, where the test gas passes through. The gas needs to be stabilized under dark condition before UV illumination until the NOx concentration is more than 90% of the desired concentration, to account for adsorption process. The UV irradiation continues for 5 hours for the photocatalytic reaction. After the photoirradiation, flow zero-calibration gas until the NOx concentration reached zero.

This standard also introduces steps for elution test to measure nitrate and nitrite ions produced on the test piece. Using series of equations, results such as the amount of NOx removed, NO_2 generated, NOx adsorbed, and NOx desorbed by the test piece can be calculated.

2.4.1.2 ISO 22197-1

The ISO 22197-1 standard, entitled “Fine ceramics (advanced ceramics, advanced technical ceramics) – Test method for air-purification performance of semiconducting photocatalytic materials – Part1: Removal of nitric oxide [99]” was established in 2007,

following the JIS standard. This standard is essentially almost identical to the JIS standard, making it public to international use.

2.4.1.3 UNI 11247

More recently in 2010, the Italian organization for standardization (UNI) published testing standards for building materials with photocatalytic activity. Three standards have been published, as of today, specially focused on cement-based materials. Those are UNI 11238-1, titled as “Determination of the catalytic degradation of organic micropollutants in air. Part 1: Photocatalytic cementitious materials,” UNI 11247, titled as “Determination of the catalytic degradation of nitrous dioxides by photocatalytic inorganic materials,” and UNI 11259, titled as “Determination of the photocatalytic activity of hydraulic binders. Rhodamine test method.” For the scope of this study, only the UNI 11247 [100] is only going to be introduced below.

The test set-up is similar to JIS/ISO standard, where a constant concentration of test gas flows through a reactor while UV light is irradiated and the concentration of test gas is measured at the output. The NOx concentration is fixed at 0.55 ppm, with 0.15 ppm of NO_2 and 0.4 ppm of NO, with flow rate at 3 L/min. The UV light intensity is twice the JIS/ISO at $20W/m^2$ on the sample surface. The duration of UV exposure is about 1 hour following stabilization time, and the NOx concentration is checked after the UV light is turned off to check if it goes back to its initial value.

One of the key differences of this standard from the other two is that the test gas used is combination of NO and NO_2. The advantage of using mixed gas is that it simulates a real world environmental condition, so the photocatalytic efficiency results

can be used to predict what is happening in real life. This point is important because NO and NO_2 convert to each other under photocatalytic reaction. However, due to the fact that NO and NO_2 converts to each other makes it not suitable for analytical work for studying detailed oxidation mechanism. The other difference from the JIS/ISO is that this standard is specially prepared for cement-based materials. This customized method might be more usable than JIS/ISO. Lastly, the results of the UNI method are calculated from the NOx plot, given as NOx reduction percentage. Photocatalytic activity could also be calculated from gas concentration measurement. This is a more direct and practical method compared to measuring the amount of byproduct (nitrate and nitrite ions) by the photocatalysis.

2.4.2 Method for Current Study

Each of the standards has its advantages and disadvantages for an experiment that specifically examines a certain properties of a material. For this study, experimental setup was mostly adopted from JIS/ISO method and results were analyzed similar to UNI method. The experimental methods such as sample size, test gas concentration, flow rate, and exposure duration were modified to author's need to better investigate the objectives of the study.

2.5 Durability of Photocatalytic Cement

2.5.1 Acid Attack

The final products of the NOx oxidation reaction, nitric acid (HNO_3) and nitrous acid (HNO_2), could be involved in chemical reaction with cementitious substrate, eventually causing damage to the material. It is widely accepted that these reaction products can be washed away by water (or rain) [12], which is further promoted by the hydrophilicity property of TiO_2 [101]. However, these acids are detrimental to the cement-based materials. Nitric acid is a strong acid that could decompose hydrated and unhydrated compounds of cement that are highly alkaline with pH ranging between 12.5-13.5. When hydrated cement based material is subjected to aggressive acidic solutions containing anions such as nitric acid solution, the alkalinity of the pore solution decreases.. The decrease in pH then results the surface of cement to a state of chemical disequilibrium, eventually destabilizing the hydration products of cement. Calcium hydroxide ($Ca(OH)_2$ or CH) decomposes as the pH drops below 12.5, ettringite decomposes at pH below 11, and calcium silicate hydrate (C-S-H) decalcifies as the pH decreases, and decomposes at pH values below 9. It was reported that nitric acid forms calcium salts that are easily soluble, which facilitates decalcifying effect [102]. The calcium salts are removed by leaching out into acid solution. The affected porous layer becomes weak in diffusion resistance, loses weight, and loses binding capacity. Nitrous acid is a weak acid that has a lower impact than nitric acid, but it could also contribute to acid attack. Nitrite ion (NO_2^-) from HONO can take part in producing nitrite salts, which will be described in the following section in more detail.

Among all the hydrated cement components, the most pronounced is the decomposition of CH; the chemical representation of this reaction under nitric acid attack is presented in Equation (2.9). The decomposition of the primary hydration products can lead to increased porosity and permeability, with loss of strength and adhesion. Acids can also deteriorate limestone aggregates [102].

$$2HNO_3 + Ca(OH)_2 \rightarrow Ca(NO_3)_2 + 2H_2O \quad (2.9)$$

The extent of the acid attack depends on the type and chemical composition of the cement as well as the pH, or ionic concentration, of the attacking acid [103]. Furthermore, soluble calcium salts ($Ca(NO_3)_2$ and $Ca(NO_2)_2$) that are formed as a result of acid attack could contribute to salt crystallization, leading to more damage. This is discussed in detail in the following section.

2.5.2 Salt Crystallization

The product of photocatalysis of NOx can further take part in formation of various salts that can eventually result in cracking and spalling of cementitious materials. During the course of photocatalytic NOx oxidation, it is anticipated that the nitrates and nitrites combine with calcium ions (Ca^{2+}) that are readily abundant in cement-based materials, forming various nitrogenous compounds of calcium (e.g., $Ca(NO_2)_2$, $Ca(NO_3)_2$). These calcium salts are highly hygroscopic, meaning that they can attract water, potentially affecting the stability of the surrounding cementitious material. In addition they are readily solvable in water, meaning that they can participate in repeated

dissolution and recrystallization cycles [104]. Furthermore, in the alkali-rich cement-based materials, nitrates can combine with alkali ions, forming other highly disruptive salts such as $NaNO_3$ and KNO_3. The formation of such salts could potentially contribute to the degradation of porous materials by salt crystallization. However, the degradation by salt crystallization due to photocatalytic oxidation has not been examined previously.

Salt crystallization is a phenomenon that porous materials such as cement-based materials, masonry, or stone undergo cracking and spalling damage due to crystallization pressure of salt crystals in their pores. When the crystallizing pressure of salts exceeds tensile strength of a porous material, the damage occurs.

There are several mechanisms proposed for several decades to explain this phenomenon and the most widely accepted these days is the theory of salt crystallization by supersaturation proposed by Scherer [105]. In his theory, condition for the occurrence of crystallization pressure is the presence of supersaturation (for precipitation) or undercooling (for freezing), and a disjoining pressure between the growing crystal and pore wall. A solute in a supersaturated solution has higher potential energy than in a corresponding saturated solution, which performs work against an external confining surface when the solute crystallizes out of solution [106]. The supersaturation can be achieved by several ways. When there is a quick drop of temperature without nucleation occurring, the solution becomes supersaturated. Also, more often the case is the evaporation of liquid. According to Scherer [105], there can be three cases where crystallization pressure affects a material. First is the case of “capillary rise and evaporation” when a porous material is in contact with a continuous supply of salt solution. The salts in a solution that is drawn into the pores by capillary suction,

precipitates as subflorescence and cause damage if the crystallization pressure exceeds the tensile strength of a material. Second is “cyclic wetting and drying,” where the water supply is from intermittent wetting such as by rain. It should be noted that the damage is found to occur during the wetting cycle rather than drying. Last case is delayed ettringite formation or growth of C-S-H in the process of cement hydration. Ettringite is expected to form during the initial hydration reaction because of addition of gypsum. However, the formation of ettringite in hardened concrete is called delayed ettringite formation, where crystallization pressure develops in nanometric pores of the paste leading to cracking. The supersaturation is reached when a material is heated to a temperature about 70°C to destabilize ettringite with respect to monosulfate phases followed by cooling to 20°C. This could produce a crystallization pressure about 6 MPa, well excess of the tensile strength of concrete. The crystallization pressure of C-S-H growth comes from the fact that there is a large increase in volume when di- and tricalcium silicate transforms into C-S-H. This is often opposed by capillary pressure created by the self-dessication of the paste.

The general form of crystallization pressure, which is the driving force for a damage of a material, can be written as Equation (2.10) [105]:

$$p_w = \frac{R_g T}{V_C} \ln\left(\frac{Q^E}{Q^S}\right) = \frac{\gamma_{CL}}{r_p - \delta} \tag{2.10}$$

where p_w is the pressure exerted by the crystal on the surrounding solid matrix, or the crystallization pressure, R_g is the gas constant, T is the absolute temperature, V_c is the molar volume of the crystal, Q^E is the solubility product, Q^S is the lower solubility

product, γ_{CL} is crystal/liquid interfacial free energy, r_p is pore radius, and δ is thickness of the film of solution lying between the crystal and the pore wall. The maximum pressure can be expected when a large crystal grows in a pore with small entries. If the pore size is macroscopic, then $Q^S=K$ and Equation (2.10) reduces to Equation (2.11) with $Q=Q^E$, known as Correns' equation.

$$p = \frac{R_g T}{V_C} \ln\left(\frac{Q}{K}\right) \tag{2.11}$$

Here, p denotes a general term for a mechanical pressure, Q is a solubility product, and K is the equilibrium solubility for a macroscopic crystal.

Most salts are reported to cause salt crystallization damage especially when subjected to repeated dissolution-crystallization cycles. During the cycles, ion concentration tends to increase which makes the salt solution supersaturated [104, 107]. The damage is also closely related to the structure of the precipitated salts [104] and pore size distribution of a material [105, 108].

There have been studies on the salt crystallization damage on porous materials. Salt scaling of concrete roadways by the use of deicing salts is among them. Usually calcium chloride ($CaCl_2$) or sodium chloride (NaCl) is used to lower the freezing point of water on the roadways in the winter, which penetrates into porous concrete and cause spalling. It gets worse by repeated wet-dry cycles and freeze-thaw cycles. Most often, research has focused on salt crystallization by sodium sulfate, sodium chloride, and sodium carbonate [106, 109-113]. For example, Scherer experimentally studied the stress from crystallization of sodium sulfate salt (thenardite (Na_2SO_4) and mirabilite

($Na_2SO_4 \cdot 10H_2O$) [105]) in stone. This phenomenon can be explained by precipitation of salt crystals from the liquid in pore structure of a material. Scherer also proposed crystallization pressure theory with the results from damage to rocks due to sodium sulfate salts [105]. Chatterji also experimentally demonstrated that a crystal growth pressure exerted by sodium thiosulfate pentahydrate ($Na_2S_2O_3 \cdot 5H_2O$) could break glass test tubes without confinement [106]. Thaulow has reviewed the mechanisms of surface scaling of concrete due to sodium sulfate salt (thenardite (Na_2SO_4) and mirabilite ($Na_2SO_4 \cdot 10H_2O$)) [110]. He compared three existing proposed mechanisms, which are solid volume change hypothesis, salt hydration pressure hypothesis, and crystallization pressure hypothesis, and concluded that it can only be explained by salt crystallization pressure theory. Lewin examined the effect of sodium chloride (NaCl) solution on stone [114], and Idorn reported on the effect of seawater on concrete [111]. Haynes et al. has performed extensive research on sodium sulfate, sodium carbonate, as well as sodium chloride solutions on concrete and mortar samples [112, 113]. More recently, Valenza has published review papers on salt scaling [109, 115] which introduces damage mechanisms associated with salt crystallization damage in porous materials.

Other salts, including nitrates, oxalates, and acetates, are known to damage porous materials [116-118] such as masonry and ceramics. For example, nitrate (NO_3^-) salts are known to damage masonry near agricultural lands [117]. Although no published literature addresses on the potential for damage by nitrate salts in cementitious materials, this suggests that $Ca(NO_3)_2$ salts could also induce cracking on cement and concrete when optimal environmental condition is provided. Thus, it is worth investigating if these salts are forming after the NOx oxidation, and contribute to scaling by salt crystallization.

2.5.3 Carbonation

Cementitious materials undergo carbonation when they are exposed to atmospheric carbon dioxide (CO_2) and moisture. Upon carbonation, the chemical composition of the surface of a material is altered which is accompanied by changes in porosity and inner structure of cement-based materials. Although carbonation does not physically degrade cementitious substrate, the changes in chemical composition and pore structure might have an effect on durability of photocatalytic cement-based materials. The main hydration products such as calcium silicate hydrate (C-S-H) and calcium hydroxide (CH), and unhydrated calcium silicates (C_3S and C_2S) react with CO_2 to form calcium carbonate ($CaCO_3$ or calcite) [119] (Equation 2.12).

$$\mathrm{Ca(OH)_2} \leftrightarrow \mathrm{Ca^{2+} + 2OH^-} \tag{2.12}$$

$$\mathrm{Ca^{2+} + 2OH^- + CO_2 \rightarrow CaCO_3 + H_2O}$$

$$\mathrm{(3CaO \cdot 2SiO_2 \cdot 3H_2O) + 3CO_2 \rightarrow (3CaCO_3 \cdot 2SiO_2 \cdot 3H_2O)}$$

$$\mathrm{(3CaO \cdot SiO_2) + 3CO_2 + \nu H_2O \rightarrow SiO_2 \cdot \nu H_2O + 3CaCO_3}$$

$$\mathrm{(2CaO \cdot SiO_2) + 2CO_2 + \nu H_2O \rightarrow SiO_2 \cdot \nu H_2O + 2CaCO_3}$$

The changes in cementitious material during carbonation can affect photocatalytic reactivity since photocatalysis takes place on the surface of a material where UV light is irradiated. It has been experimentally determined that cement carbonation decreases the rate of pollutant degradation [42, 120]. Lackhoff et al. examined the influence of carbonation on the degradation rate of atrazine, and found reduction of photocatalytic activity possibly due to decreased specific surface area, decreased atrazine sorptivity, and

calcite overgrowth on the cement surface [120]. Chen et al. performed experiments on NOx degradation, where they also found reduced photocatalytic efficiency after surface carbonation, possibly due to $CaCO_3$ deposition in pores and thus reducing total porosity [42]. It is not clear what mechanism is responsible for decreased photocatalytic efficiency until now. However, it is anticipated that carbonation occurs simultaneously with the previously stated nitric acid attack and salt crystallization. Considering that most of the photocatalytic cement applications are in outdoor environment, long term concrete ageing should be taken into account in relation to photocatalytic efficiency and to long term durability.

2.6 References

5. WHO, *Air quality guidelines, Global update 2005.* World Health Organization, 2005.

8. Carp, O., C.L. Huisman, and A. Reller, *Photoinduced reactivity of titanium dioxide.* Progress in Solid State Chemistry, 2004. **32**(1-2): p. 33-177.

10. Fujishima, A., X.T. Zhang, and D.A. Tryk, *TiO_2 photocatalysis and related surface phenomena.* Surface Science Reports, 2008. **63**(12): p. 515-582.

12. Chen, J. and C.S. Poon, *Photocatalytic construction and building materials: From fundamentals to applications.* Building and Environment, 2009. **44**(9): p. 1899-1906.

14. Poon, C.S. and E. Cheung, *NO removal efficiency of photocatalytic paving blocks prepared with recycled materials.* Construction and Building Materials, 2007. **21**(8): p. 1746-1753.

15. Husken, G., M. Hunger, and H. Brouwers. *Comparative study on cementitious products containing titanium dioxide as photo-catalyst*. in *RILEM Int. Symp. on Photocatalysis, Environment and Construction Materials*, 2007. Italy.

17. Maggos, T., et al., *Photocatalytic degradation of NO_x in a pilot street canyon configuration using TiO_2-mortar panels.* Environmental Monitoring and Assessment, 2008. **136**(1-3): p. 35-44.

18. Fujishima, A. and X.T. Zhang, *Titanium dioxide photocatalysis: present situation and future approaches.* Comptes Rendus Chimie, 2006. **9**(5-6): p. 750-760.

22. Ramirez, A.M., et al., *Titanium dioxide coated cementitious materials for air purifying purposes: Preparation, characterization and toluene removal potential.* Building and Environment, 2010. **45**(4): p. 832-838.

23. NSTC, *The national nanotechnology initiative - Strategic plan*, December 2007: Executive Office of the President of the United States.

24. Sanchez, F. and K. Sobolev, *Nanotechnology in concrete – A review.* Construction and Building Materials, 2010. **24**(11): p. 2060-2071.

25. Feynman, R., *There's plenty of room at the bottom (reprint from speech given at annual meeting of the American Physical Society).* Eng Sci 1960. **23**: p. 23-36.

26. Hui, L., H.G. Xiao, and J.P. Ou, *A study on mechanical and pressure-sensitive properties of cement mortar with nanophase materials.* Cement and Concrete Research, 2004. **34**(3): p. 435-438.

27. Jo, B.W., et al., *Characteristics of cement mortar with nano-SiO_2 particles.* Construction and Building Materials, 2007. **21**(6): p. 1351-1355.

28. Tao, J., *Preliminary study on the water permeability and microstructure of concrete incorporating nano-SiO_2.* Cement And Concrete Research, 2005. **35**(10): p. 1943-1947.

29. Bjornstrom, J., et al., *Accelerating effects of colloidal nano-silica for beneficial calcium-silicate-hydrate formation in cement.* Chemical Physics Letters, 2004. **392**(1-3): p. 242-248.

30. Li, H., M.H. Zhang, and J.P. Ou, *Abrasion resistance of concrete containing nano-particles for pavement.* Wear, 2006. **260**(11-12): p. 1262-1266.

31. Nazari, A. and S. Riahi, *Abrasion resistance of concrete containing SiO_2 and Al_2O_3 nanoparticles in different curing media.* Energy and Buildings, 2011. **43**(10): p. 2939-2946.

32. Lee, B.Y. and K.E. Kurtis, *Influence of TiO_2 Nanoparticles on Early C_3S Hydration.* Journal of the American Ceramic Society, 2010. **93**(10): p. 3399-3405.

33. Li, H., M.H. Zhang, and J.P. Ou, *Flexural fatigue performance of concrete containing nano-particles for pavement.* International Journal of Fatigue, 2007. **29**(7): p. 1292-1301.

34. Campillo, I., et al., *Improvement of initial mechanical strength by nanoalumina in belite cements.* Materials Letters, 2007. **61**(8-9): p. 1889-1892.

35. Kuo, W.Y., J.S. Huang, and C.H. Lin, *Effects of organo-modified montmorillonite on strengths and permeability of cement mortars.* Cement And Concrete Research, 2006. **36**(5): p. 886-895.

36. Chang, T.P., et al., *Material properties of portland cement paste with nano-montmorillonite.* Journal of Materials Science, 2007. **42**(17): p. 7478-7487.

37. Lee, S.J. and W.M. Kriven, *Synthesis and hydration study of Portland cement components prepared by the organic steric entrapment method.* Materials and Structures, 2005. **38**(275): p. 87-92.

38. Scrivener, K.L. and R.J. Kirkpatrick, *Innovation in use and research on cementitious material.* Cement And Concrete Research, 2008. **38**(2): p. 128-136.

39. Cassar, L., *Photocatalysis of cementitious materials: Clean buildings and clean air.* Mrs Bulletin, 2004. **29**(5): p. 328-331.

40. Dalton, J.S., et al., *Photocatalytic oxidation of NO_x gases using TiO_2: a surface spectroscopic approach.* Environmental Pollution, 2002. **120**: p. 415-422.

41. Cassar, L. *Nanotechnology and photocatalysis in cementitious materials*. in *Nanotechnology in Construction 2*, 2005. Bilbao: RILEM Publications SARL.

42. Chen, J. and C.S. Poon, *Photocatalytic cementitious materials: Influence of the microstructure of cement paste on photocatalytic pollution degradation.* Environmental Science & Technology, 2009. **43**(23): p. 8948-8952.

43. Strini, A., S. Cassese, and L. Schiavi, *Measurement of benzene, toluene, ethylbenzene and o-xylene gas phase photodegradation by titanium dioxide dispersed in cementitious materials using a mixed flow reactor.* Applied Catalysis B-Environmental, 2005. **61**(1-2): p. 90-97.

44. Wang, S., H.M. Ang, and M.O. Tade, *Volatile organic compounds in indoor environment and photocatalytic oxidation: State of the art.* Environment International, 2007. **33**: p. 694-705.

45. Vallee, F., et al. *Innovative self-cleaning and de-polluting facades surfaces*. in *CIB World Building Congress*, 2004. Toronto, Canada.

46. Diamanti, M.V., M. Ormellese, and M. Pedeferri, *Characterization of photocatalytic and superhydrophilic properties of mortars containing titanium dioxide.* Cement And Concrete Research, 2008. **38**(11): p. 1349-1353.

47. Ruot, B., et al., *TiO_2-containing cement pastes and mortars: Measurements of the photocatalytic efficiency using a rhodamine B-based colourimetric test.* Solar Energy, 2009. **83**(10): p. 1794-1801.

48. Giannantonio, D.J., et al., *Effects of concrete properties and nutrients on fungal colonization and fouling.* International Biodeterioration & Biodegradation, 2009. **63**(3): p. 252-259.

49. Ramirez, A.M. and N. De Belie, *Evaluation of the algaecide activity of titanium dioxide on autoclaved aerated concrete.* Journal of Advanced Oxidation Technologies, 2009. **12**(1): p. 100-104.

50. Jayapalan, A.R., B.Y. Lee, and K.E. Kurtis. *Effect of nano-sized titanium dioxide on early age hydration of portland cement*. in *Nanotechnology in Construction 3,* 2009. Prague, Czech Republic.

51. Li, H., H.-g. Xiao, and J.-p. Ou, *A study on mechanical and pressure-sensitive properties of cement mortar with nanophase materials.* Cement And Concrete Research, 2004. **34**(3): p. 435-438.

52. Lee, B.Y. and K.E. Kurtis, *Proposed acceleratory effect of TiO_2 nanoparticles on belite hydration: Preliminary results.* Journal Of The American Ceramic Society, 2012. **95**(1): p. 365-368.

53. Rana, A.K., et al., *Significance of nanotechnology in construction engineering.* International Journal of Recent Trends in Engineering, 2009. **1**(4): p. 46-48.

54. Sobolev, K. and M.F. Gutierrez, *How nanotechnology can change the concrete world.* American Ceramic Society Bulletin, 2005. **84**(11): p. 16-19.

55. Fujishima, A. and K. Honda, *Electrochemical photolysis of water at a semiconductor electrode.* Nature, 1972. **238**(5358): p. 37-+.

56. Dubrovinsky, L.S., et al., *The hardest known oxide.* Nature, 2001. **410**(6829): p. 653.

57. H.Zhang and J.F. Banfield, J. Phys. Chem. B, 2000. **104**: p. 3481-3487.

58. Ahmed, A.Y., et al., *Photocatalytic activities of different well-defined single crystal TiO_2 surfaces: anatase versus rutile.* The Journal of Physical Chemistry Letters, 2011. **2**(19): p. 2461-2465.

59. Tanaka, K., M.F.V. Capule, and T. Hisanaga, *Effect of crytallinity of TiO_2 on its photocatalytic action.* Chemical Physics Letters, 1991. **187**(1-2): p. 73-76.

60. Bianchi, C.L., et al. *The Role of the Synthetic Procedure of Nano-Crystalline TiO_2 on the Photodegradation of Toluene*. in *International RILEM Symposium on Photocatalysis, Environment, and Construction Materials - TDP 2007*, 2007. Florence, Italy: Rilem Publications.

61. Su, R., et al., *How the anatase-to-rutile ratio influences the photoreactivity of TiO_2.* The Journal of Physical Chemistry C, 2011. **115**(49): p. 24287-24292.

62. Tayca Corporation. *http://www.tayca.co.jp/english*.

63. Millenium Inorganic Chemicals. *http://www.milleniumchem.com*.

64. A. Fujishima, K. Hashimoto, and T. Watanabe, *TiO2 photocatalysis. Fundaments and applications*. 1st ed. 1999, Tokyo: BKC.

65. Devahasdin, S., et al., *TiO_2 photocatalytic oxidation of nitric oxide: transient behavior and reaction kinetics.* Journal of Photochemistry and Photobiology a-Chemistry, 2003. **156**(1-3): p. 161-170.

66. Ardizzone, S., et al., *Tailored anatase/brookite nanocrystalline TiO_2. The optimal particle features for liquid- and gas-phase photocatalytic reactions.* The Journal of Physical Chemistry C, 2007. **111**(35): p. 13222-13231.

67. Anpo, M., *Utilization of TiO_2 photocatalysts in green chemistry.* Pure and Applied Chemistry, 2000. **72**(7): p. 1265-1270.

68. Ndour, M., et al., *Photoenhanced uptake of NO_2 on mineral dust: Laboratory experiments and model simulations.* Geophysical Research Letters, 2008. **35**(5).

69. Laufs, S., et al., *Conversion of nitrogen oxides on commercial photocatalytic dispersion paints.* Atmospheric Environment, 2010. **44**(19): p. 2341-2349.

70. Ohko, Y., et al., *Photocatalytic oxidation of nitrogen dioxide with TiO_2 thin films under continuous UV-light illumination.* Journal of Physical Chemistry C, 2008. **112**(28): p. 10502-10508.

71. Tseng, Y.H., et al., *Visible-light-responsive nano-TiO_2 with mixed crystal lattice and its photocatalytic activity.* Nanotechnology, 2006. **17**(10): p. 2490-2497.

72. Lawrence, P., M. Cyr, and E. Ringot, *Mineral admixtures in mortars - Effect of inert materials on short-term hydration.* Cement and Concrete Research, 2003. **33**(12): p. 1939-1947.

73. Zelic, J., et al., *The role of silica fume in the kinetics and mechanisms during the early stage of cement hydration.* Cement and Concrete Research, 2000. **30**(10): p. 1655-1662.

74. Gutteridge, W.A. and J.A. Dalziel, *Filler cement: The effect of the secondary component on the hydration of Portland cement: Part I. A fine non-hydraulic filler.* Cement And Concrete Research, 1990. **20**(5): p. 778-782.

75. Gutteridge, W.A. and J.A. Dalziel, *Filler cement - The effect of the secondary component on the hydration of portland-cement 2. Fine hydraulic binders.* Cement and Concrete Research, 1990. **20**(6): p. 853-861.

76. Lothenbach, B., et al., *Influence of limestone on the hydration of Portland cements.* Cement And Concrete Research, 2008. **38**(6): p. 848-860.

77. Kadri, E. and R. Duval, *Effect of ultrafine particles on heat of hydration of cement mortars.* Aci Materials Journal, 2002. **99**(2): p. 138-142.

78. Thomas, J.J., H.M. Jennings, and J.J. Chen, *Influence of nucleation seeding on the hydration mechanisms of tricalcium silicate and cement.* Journal of Physical Chemistry C, 2009. **113**(11): p. 4327-4334.

79. Bishnoi, S. and K.L. Scrivener, *Studying nucleation and growth kinetics of alite hydration using μic.* Cement and Concrete Research, 2009. **39**(10): p. 849-860.

80. Damasceni, A., et al., *A novel approach based on differential scanning calorimetry applied to the study of tricalcium silicate hydration kinetics.* Journal of Physical Chemistry B, 2002. **106**(44): p. 11572-11578.

81. Avrami, M., *Kinetics of phase change I - General theory.* Journal of Chemical Physics, 1939. **7**(12): p. 1103-1112.

82. Avrami, M., *Kinetics of phase change 2 - Transformation-time relations for random distribution of nuclei.* Journal of Chemical Physics, 1940. **8**: p. 212-24.

83. Avrami, M., *Granulation, phase change, and microstructure - Kinetics of phase change. III.* Journal of Chemical Physics, 1941. **9**(2): p. 177-184.

84. Fanfoni, M. and M. Tomellini, *The Johnson-Mehl-Avrami-Kolmogorov model: A brief review.* Il Nuovo Cimento. D, 1998. **20**: p. 1171-1182.

85. Cahn, J.W., *The kinetics of grain boundary nucleated reactions.* Acta Metallurgica, 1956. **4**(5): p. 449-459.

86. Brown, P.W., J. Pommersheim, and G. Frohnsdorff, *A kinetic-model for the hydration of tricalcium silicate.* Cement and Concrete Research, 1985. **15**(1): p. 35-41.

87. FitzGerald, S.A., et al., *In situ quasi-elastic neutron scattering study of the hydration of tricalcium silicate.* Chemistry of Materials, 1998. **10**(1): p. 397-402.

88. Thomas, J.J. and H.M. Jennings, *Effects of D_2O and mixing on the early hydration kinetics of tricalcium silicate.* Chemistry of Materials, 1999. **11**(7): p. 1907-1914.

89. Ridi, F., et al., *Hydration process of cement in the presence of a cellulosic additive. A calorimetric investigation.* Journal of Physical Chemistry B, 2005. **109**(30): p. 14727-14734.

90. Kolmogorov, A.N., *A statistical theory for the recrystallization of metals.* Bulletin of the Academy of Sciences of the USSR: physics series, 1937. **1**: p. 355-359.

91. Johnson, W.A. and R.F. Mehl, *Reaction kinetics in processes of nucleation and growth.* Transactions of the American Institute of Mining and Metallurgical Engineers 1939. **135**: p. 416-442.

92. Thomas, J.J., *A new approach to modeling the nucleation and growth kinetics of tricalcium silicate hydration.* Journal of the American Ceramic Society, 2007. **90**(10): p. 3282-3288.

93. Garrault, S., T. Behr, and A. Nonat, *Formation of the C-S-H layer during early hydration of tricalcium silicate grains with different sizes.* Journal of Physical Chemistry B, 2006. **110**(1): p. 270-275.

94. Gauffinet, S., et al., *Direct observation of the growth of calcium silicate hydrate on alite and silica surfaces by atomic force microscopy.* Comptes Rendus De L Academie Des Sciences Serie Ii Fascicule a-Sciences De La Terre Et Des Planetes, 1998. **327**(4): p. 231-236.

95. Makar, J.M. and G.W. Chan, *Growth of cement hydration products on single-walled carbon nanotubes.* Journal of the American Ceramic Society, 2009. **92**(6): p. 1303-1310.

96. Brown, P.W., *Effects of particle-size distribution on the kinetics of hydration of tricalcium silicate.* Journal of the American Ceramic Society, 1989. **72**(10): p. 1829-1832.

97. Bentz, D.P., et al., *Effects of cement particle size distribution on performance properties of portland cement-based materials.* Cement and Concrete Research, 1999. **29**(10): p. 1663-1671.

98. JIS, *Fine ceramics (advanced ceramics, advanced technical ceramics) - Test method for air purification performance of photocatalytic materials* in *Part 1: Removal of nitric oxide*2004.

99. ISO, *Fine ceramics (advanced ceramics, advanced technical ceramics) - Test method for air-purification performance of semiconducting photocatalytic materials*, in *Part 1: Removal of nitric oxide*2007.

100. UNI, *Determination of the catalytic degradation of nitrous dioxides by photocatalytic inorganic materials*, 2010.

101. Wang, R., et al., *Light-induced amphiphilic surfaces.* Nature, 1997. **388**(6641): p. 431-432.

102. Pavlik, V. and S. Uncik, *The rate of corrosion of hardened cement pastes and mortars with additive of silica fume in acids.* Cement And Concrete Research, 1997. **27**(11): p. 1731-1745.

103. Beddoe, R.E. and H.W. Dorner, *Modelling acid attack on concrete: Part I. The essential mechanisms.* Cement And Concrete Research, 2005. **35**(12): p. 2333-2339.

104. Shahidzadeh-Bonn, N., et al., *Salt crystallization during evaporation: Impact of interfacial properties.* Langmuir, 2008. **24**(16): p. 8599-8605.

105. Scherer, G.W., *Stress from crystallization of salt.* Cement and Concrete Research, 2004. **34**(9): p. 1613-1624.

106. Chatterji, S. and N. Thaulow, *Unambiguous demonstration of destructive crystal growth pressure.* Cement and Concrete Research, 1997. **27**(6): p. 811-816.

107. Flatt, R.J., *Salt damage in porous materials: how high supersaturations are generated.* Journal of Crystal Growth, 2002. **242**(3-4): p. 435-454.

108. Coussy, O., *Deformation and stress from in-pore drying-induced crystallization of salt.* Journal of the Mechanics and Physics of Solids, 2006. **54**(8): p. 1517-1547.

109. Valenza, J.J. and G.W. Scherer, *A review of salt scaling: I. Phenomenology.* Cement and Concrete Research, 2007. **37**(7): p. 1007-1021.

110. Thaulow, N. and S. Sahu, *Mechanism of concrete deterioration due to salt crystallization.* Materials Characterization, 2004. **53**(2-4): p. 123-127.

111. Idorn, G.M., *Concrete progress : from antiquity to third millennium*. 1997, London :: Thomas Telford.

112. Haynes, H., et al., *Salt weathering distress on concrete exposed to sodium sulfate environment.* Aci Materials Journal, 2008. **105**(1): p. 35-43.

113. Haynes, H., et al., *Salt weathering of concrete by sodium carbonate and sodium chloride.* Aci Materials Journal, 2010. **107**(3): p. 258-266.

114. Lewin, S.Z., *The mechanism of masonry decay through crystallization*, in *Conservation of historic stone buildings and monuments* 1982, National Academy Press: Washington, D.C. :. p. 120-144.

115. Valenza, J.J. and G.W. Scherer, *A review of salt scaling: II. Mechanisms.* Cement and Concrete Research, 2007. **37**(7): p. 1022-1034.

116. Linnow, K., L. Halsberghe, and M. Steiger, *Analysis of calcium acetate efflorescences formed on ceramic tiles in a museum environment.* Journal of Cultural Heritage, 2007. **8**(1): p. 44-52.

117. Ottosen, L.M. and I. Rorig-Dalgard, *Electrokinetic removal of $Ca(NO_3)_2$ from bricks to avoid salt-induced decay.* Electrochimica Acta, 2007. **52**(10): p. 3454-3463.

118. Dei, L., M. Mauro, and G. Bitossi, *Characterisation of salt efflorescences in cultural heritage conservation by thermal analysis.* Thermochimica Acta, 1998. **317**(2): p. 133-140.

119. Papadakis, V.G., C.G. Vayenas, and M.N. Fardis, *Fundamental modeling and experimental investigation of concrete carbonation.* Aci Materials Journal, 1991. **88**(4): p. 363-373.

120. Lackhoff, M., et al., *Photocatalytic activity of semiconductor-modified cement-influence of semiconductor type and cement ageing.* Applied Catalysis B-Environmental, 2003. **43**(3): p. 205-216.

CHAPTER 3

EFFECTS OF NANO-TITANIUM DIOXIDE ON PROPERTIES OF CEMENTITIOUS MATERIALS

3.1 Introduction

Over the past 15-20 years, interest and use of titanium dioxide (TiO_2) in building materials has increased [121]. The interest in use of TiO_2 in construction materials started with additions to white cement due to the mineral's inherently white color. However, its capacity in certain forms for environmental photocatalysis, producing self-cleaning and smog-abating properties as well as its ability to exhibit both hydrophobicity and hydrophilicity, has widened its application. Study of TiO_2 in construction materials as a photocatalytic material initiated from the early 1990s [12]. The early studies and applications focused on its self cleaning ability, which enabled the facades of buildings to remain clean from stains [13]. More recently, interest in its smog-abating property is increasing [12, 14-17, 122]. Especially, studies report that TiO_2 effectively oxidizes nitrogen oxides ($NOx = NO+NO_2$), shown by several laboratory studies [14, 15, 122] and some pilot projects [16, 17]. Also, TiO_2 is reported to effectively oxidize volatile organic compounds (VOCs), which negatively affect indoor air quality [43, 44]. This technology is already available commercially in cementitious materials among other applications, including its use in photocatalytic cement (Italcementi Group) or in concrete paving materials [18].

In commercially available TiO_2-containing cementitious materials, the titania can be present in a surface coating (of varying thickness) or throughout the bulk material, where it is typically present at rates of less than 5% by mass. This research focuses on the latter method of use, but the results are also applicable to some surface coatings such as cementitious overlays (i.e., “whitetoppings”).

When combined with cement and water, the TiO_2 nanoparticles tend to agglomerate [123]. However, due to their high surface area, even when agglomerated, the nanoparticles impart high photocatalytic efficiency to the cementitious substrate [123]. It is important to recognize that these particles are chemically inert, in terms of their potential to directly react during cement hydration.

Prior research on TiO_2-containing cementitious materials have examined their photocatalytic properties, including quantifying the photocatalytic efficiency and development of enhancements for this behavior [17, 21, 22]. However, relatively little research has examined the influence of TiO_2 nanoparticle additions on the performance of the cementitious substrate, although preliminary results do suggest that their use does have measureable effects on a range of properties. For example, Lackhoff et al. [120] have reported increased compressive strength of TiO_2-modified mortar cubes. More recent research by this author and co-workers has demonstrated that TiO_2 nanoparticles, although chemically inert with cement as noted above, can accelerate cement hydration by providing additional surface area for product nucleation (i.e., boundary nucleation effect [92]) [32, 124]. Others [125] have examined the abrasion resistance of a TiO_2-cement coating by loaded-wheel tester and it was concluded that the coating did not affect the wear resistance of the surface. Given the growing application of TiO_2-modified

cementitious systems and their tremendous potential for environmental benefit, it is crucial that the performance of this emerging class of materials be examined more comprehensively.

In this research, the effects of the addition of several commercially available TiO_2 nanoparticles on the early and late age properties of cementitious materials were examined. At early ages, the influence of their addition on heat of hydration, setting time, and early age shrinkage were assessed and at later ages, measurements of surface hardness and compressive strength were made, all at varying percentages of TiO_2 addition. The overall aim of this study was to better understand the influence of the TiO_2 nanoparticles in cementitious materials, forming a basis for optimizing cementitious composites to achieve desired early age behavior and mechanical properties while introducing new functionality.

3.2 Experimental Procedure

3.2.1 Materials

TiO_2 particles produced by different manufacturers tend to have different properties due to different manufacturing processes and treatments. Different particle/agglomerate size, dispersability, pH, and composition may affect TiO_2-cement properties at varying ages. In this research, two TiO_2 sources – P25 (Aeroxide TiO_2 P25, Evonik Industries) and PC50 (Millennium Inorganic Chemicals) – were selected for study based on their frequency of usage in cementitious materials, similarity in particle size and pH, and their reported photocatalytic efficiency.

For both samples, the TiO_2 particle size distribution was measured in water (Zetasizer Nano, Malvern Instruments, UK) (Figure 3.1). In order to better disperse the TiO_2 particles, superplasticizer was used at 2% by mass of water, and the slurry was ultrasonicated for 1 hour prior to the measurement. Note that the measured particle size of TiO_2 is in micro-scale, which is expected and is likely due to agglomeration [123]. Other properties were obtained from the manufacturer and are listed in Table 3.1.

The cement used was ASTM C 150 Type Ⅰ portland cement. Table 3.2 presents chemical oxide analysis and Bogue potential composition of the cement.

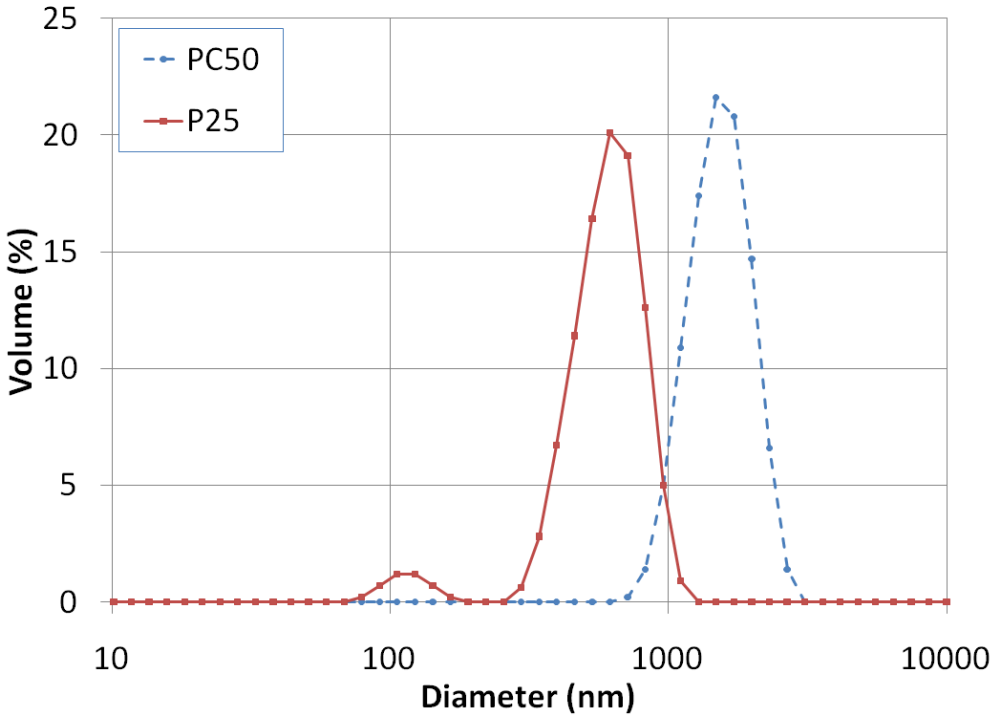

Figure 3.1—Particle size distribution of TiO_2 powders

Table 3.1—Properties of TiO_2 samples used*

	Crystal Size (nm)	Surface Area (m^2/g)	pH	Purity (%)	Structure	Specific Gravity
P25	21	50±15	3.5 - 4.5 (40 g/l or 4% dispersion)	99.5	80% Anatase	3.8
PC50	20-30	45-55	3.5 - 5.5 (10g/100ml)	≥ 97	97% Anatase	3.8

* All are manufacturer provided data.

Table 3.2—Chemical oxide analysis and Bogue potential composition of cement

Oxide/Phase	Wt(%)	Oxide/Phase	Wt(%)
Silicon Dioxide (SiO_2)	20.38	Phosphorus Pentoxide (P_2O_5)	0.06
Aluminum Oxide (Al_2O_3)	5.00	Strontium Oxide (SrO)	0.04
Iron Oxide (Fe_2O_3)	3.09	Barium Oxide (BaO)	0.03
Calcium Oxide (CaO)	61.82	Sulfur Trioxide (SO_3)	2.62
Magnesium Oxide (MgO)	3.66	Loss on Ignition	2.35
Sodium Oxide (Na_2O)	0.07	Insoluble Residue	0.30
Potassium Oxide (K_2O)	0.50	Tricalcium Silicate (C_3S*)	51.30
Total Alkali (Na_2Oeq)	0.40	Tricalcium Aluminate (C_3A*)	8.01
Titanium Oxide (TiO_2)	0.25	Dicalcium Silicate (C_2S*)	19.73
Manganic Oxide (Mn_2O_3)	0.13	Tetracalcium Aluminoferrite (C_4AF*)	9.41

* The cement chemistry notations of these oxides are defined as C=CaO, S=SiO_2, F=Fe_2O_3, and A=Al_2O_3.

3.2.2 Sample Preparation

For this study, cement paste samples with and without TiO_2 nanoparticles were prepared. When used, the TiO_2 particles were mixed with deionized water for 1 minute using a hand-held mixer in a low speed in an attempt to improve their dispersion. Cement

was then added to the TiO_2 slurry and mixed for 2 minutes at a low speed and another 1 minute at a medium speed. All the samples were prepared at w/c of 0.50 except for those used for measured of setting time by the Vicat method [126]; a w/c of 0.37 was used for optimal consistency among the various samples. For P25-cement samples, the TiO_2 powder was dosed at 5% and 10% replacement rate by mass of cement, and PC50-cement samples were prepared at 5%, 10%, and 15% TiO_2 replacement by mass of cement. Dosing rate of 15% of P25-cement was not examined due to difficulties mixing at the highest dosage rate examined. Control samples without any TiO_2 powder were prepared in a similar manner.

3.2.3 Methodology

Heat of hydration, chemical shrinkage, and setting time experiments were performed with P25 and PC50 modified cement pastes to examine the early age properties. Compressive strength and microhardness tests were performed only with PC25 modified cement pastes.

3.2.3.1 Isothermal Calorimetry

The total heat evolved and rate of hydration were measured by isothermal calorimetry (TAM AIR, TA instruments) following ASTM C1702 [127], at 25°C, with a precision of ±20μW and accuracy greater than 95%. To prepare the samples, all materials and mixing equipment were equilibrated at 23±2°C for 24h before the testing. Less than 10g of samples were put in plastic ampoules and placed into the calorimetry less than 5 minutes after mixing with cement. The calorimetry data from the initial 15 minutes after

mixing were excluded as some time is required for the samples to become equilibrated within the instrument. Measurements were made up to initial 80 hours from the start of mixing.

3.2.3.2 Chemical Shrinkage

Chemical shrinkage is the volume reduction that is associated with the reaction between cement and water. It is proportional to the degree of hydration. The chemical shrinkage of cement pastes with TiO_2 particles was performed according to ASTM C 1608-07 Procedure A [128]. For all the mixes, w/c was constant at 0.50. Cement pastes were put in glass vials mounted with graduated capillary tube, and placed in an environmental chamber where temperature was maintained at 23°C. Readings were recorded every 30 min for the first 24 hours, and then 2 hours thereafter up to 50 hours. Results are averaged from three replicates for each mix.

3.2.3.3 Setting Time

Setting times were measured according to ASTM C 191 Method A [126] using Vicat needle. The w/c was remained constant at 0.37 among all the samples, which was determined for normal consistency of neat ordinary portland cement according to [129]. This enables direct comparison between samples with different kinds and addition rates of TiO_2. The penetration depth was measured every 15 minutes until final set with measurements at five different locations averaged.

3.2.3.4 Compressive Strength

Compressive strength of cement pastes at different addition rates of TiO_2 (P25) was determined using half-inch (2.54cm) cubes. Samples were cast in plastic cube molds and vibrated for better compaction. The samples were demolded after 1 day of curing at 100% RH, and then stored in limewater at room temperature (23±2°C) until the compression testing. To ensure same condition among all the samples at the time of the testing, the samples were remained wet until just prior to testing. A SATEC Materials Testing Machine (INSTRON) with a capacity of 100kN (22kips) was used at a loading increment rate of 500 lbs/min (226 kg/min). Twelve samples were tested per each group, and results were averaged. Samples were tested at 1, 3, 7, 14, and 28 days of age. Additional tests were performed on samples of w/c=0.40, 0.50, and 0.60 and TiO_2 (P25) at 0%, 5%, and 10% dosage rates at 28 days in order to examine the effect of w/c and TiO_2 addition rates. Sample preparation and testing conditions were the same, but here, different Type 1 portland cement was used due to unavailability. The Bogue potential composition of this cement was 54.0% C_3S, 18.0% C_2S, 6.7% C_3A, 10.0% C_4AF, and 6.4% gypsum.

3.2.3.5 Microhardness

Because hardness is directly related to wear resistance, the surface hardness of TiO_2-bearing cementitious material is of importance for applications such as pavements. In addition, surface hardness can be used to assess quality of a cementitious material as it relates to variations in composition or environmental exposure [130-133].

Vickers microindentation method was performed, following ASTM C 1327-08 [134], on 5cm x 5cm x 0.8cm (1.97in x 1.97in x 0.31in) TiO_2-cement tiles. The samples were demolded after 1 day of curing at RH of 100%, and continued to be cured under limewater at room temperature (23±2°C) until the time of testing. Samples were tested at 1, 3, 7, 14, and 28 days of age. Samples tested at 1 and 3 days could only be polished to 1 μm due to their soft surface, and samples at higher age were polished to 0.3 μm, so that indentation marks can clearly be identified. The samples were polished immediately before testing to avoid spurious effects due to variations in degree of hydration or carbonation at the surface. A 1 kgf load was applied and twelve indentations were made per sample at each age and averaged.

3.3 Results and Discussion

3.3.1 Early Age Hydration

The calorimetry results for 5% and 10% P25-cement pastes, 5%, 10%, and 15% PC50-cement pastes, and control neat cement paste are presented in Figure 3.2 (a) and (b); the rate of hydration data per gram of cement (i.e., excluding TiO_2) for the first 30 h after mixing are shown in Figure 3.2 (a) and corresponding cumulative heat data for the first 80 h are presented in Figure 3.2 (b). These data from Figure 3.2 (a) suggest that the rate peak heights were increased and the reaction was accelerated with the addition of the chemically inert TiO_2 nanoparticles. For example, for the P25-cement pastes, the initial rate peak (i.e., that typically associated with C_3S reaction) was increased by 53% and 81% and the second rate peak (i.e., that typically associated with C_3A) was increased by 47% and 81%, for the 5% and 10% case respectively compared to neat cement paste. For the

PC50-cement pastes, the second rate peaks, which are more apparent, were increased by 5%, 9%, and 12% for the 5%, 10%, and 15% case respectively compared to neat cement paste.

Comparing the rate peaks among P25-cement paste samples, the occurrence of the initial peak was accelerated, or shifted to the left, by 3.42 h and 3.77 h for the 5% and 10% case respectively compared to neat control cement paste. For the PC50-cement pastes, the rate peaks were accelerated by 0.83 h, 1.26 h, 1.64 h for the 5%, 10%, and 15% case respectively compared to neat cement paste. Again, for the PC50 containing samples, the second rate peaks are considered for the analysis as the first rate peaks are not as well-defined.

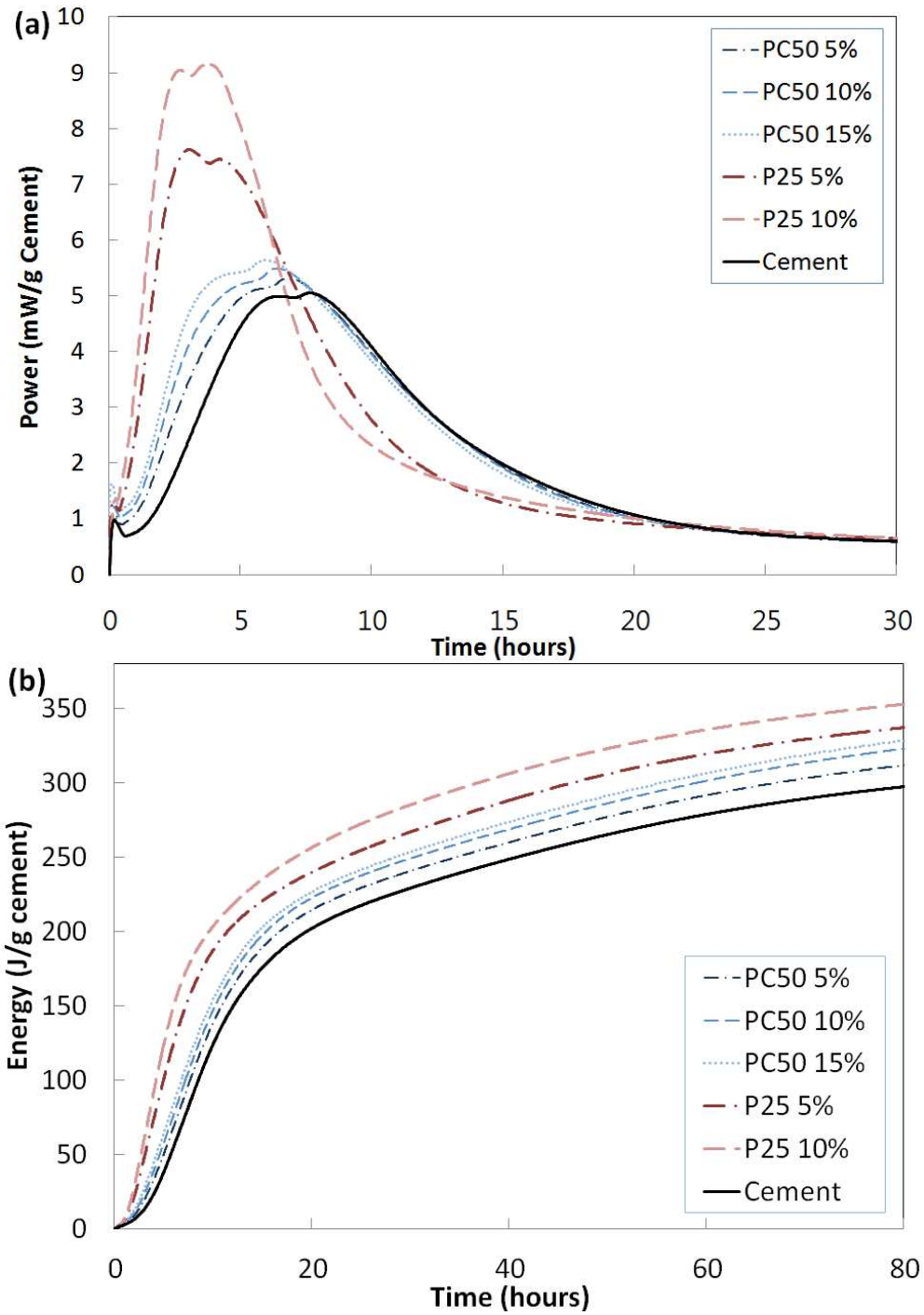

Figure 3.2—(a) Hydration rate of P25 and PC50 blended cement pastes (b) Cumulative heat of hydration of P25 and PC50 blended cement pastes

The effect of TiO_2 addition on the degree of hydration can be inferred from the cumulative heat data in Figure 3.2 (b). These indicate that the addition of TiO_2 nanoparticles increase the degree of hydration of cement paste from initial hydration throughout 80 hours of data acquired. Qualitatively, higher rate of TiO_2 addition resulted higher degrees of hydration at all times.

The cumulative heat of hydration and the degree of hydration, α, of TiO_2 modified cement paste samples at 12 h and 48 h compared to neat cement paste are presented in Table 3.3. The degree of hydration was calculated by dividing the cumulative heat of hydration at a given time by the maximum theoretical heat release (i.e., upon 100% reaction). Maximum heat released can be calculated by combining theoretical heat of each of the main components of cement at their corresponding mass fraction. The reported values of theoretical heat of each of the components of cement used for this study are 490 J/g for C_3S, 225 J/g for C_2S, 1160 J/g for C_3A, and 375 J/g for C_4AF [135]. A simplifying assumption was made that the remaining mass (i.e., that is not part of the four main components of cement) releases an average heat of the four main components. Comparing the calorimetry results between the P25 modified cement pastes and PC50 modified cement pastes, the P25 samples showed faster rate of reaction and greater heat evolution than PC50 samples throughout the experiment up to 80 hours. As a result, the degree of hydrations for the P25 sample at 5% and 10% dosage rates are higher than PC50 5% and 10% samples by 8% and 9% at 80 h. It is believed that this may be due to differences in the dispersability of the two nanoparticles examined (Figure 3.1). The greater dispersability and small particle size of P25 is thought to provide more surface area for nuclei to form on during early hydration [124], thus resulting in a faster rate of

reaction. The P25 accelerates the rate of hydration more than the PC50, reaches higher rate peaks, and results in higher degree of hydration than PC50.

Table 3.3–Cumulative heat of hydration and degree of hydration compared to control

		OPC	P25		PC50		
		-	5%	10%	5%	10%	15%
12 h	Cumulative heat of hydration, J/g cement	149	204	218	162	172	178
	Degree of hydration, α	0.31	0.43	0.45	0.34	0.36	0.37
	Relative increase, %	-	36.62	46.15	8.54	14.99	19.22
48 h	Cumulative heat of hydration, J/g cement	262	303	320	274	283	288
	Degree of hydration, α	0.55	0.63	0.67	0.57	0.59	0.60
	Relative increase, %	-	15.52	22.12	4.48	7.93	9.88

3.3.2 Chemical shrinkage

Figure 3.3 shows chemical shrinkage results up to initial 80 h after mixing for samples including 5% and 10% P25-cement pastes, 5%, 10%, and 15% PC50-cement pastes, and neat cement paste. In general, the rate of chemical shrinkage was relatively fast through the first 10-20 hours and then slowed down, ultimately reaching a plateau. All of the samples that include TiO_2 particles resulted greater chemical shrinkage than the control neat cement paste sample. The trends in chemical shrinkage were similar to the energy release curve from the calorimetry (Figure 3.2 (b)) as expected, since chemical shrinkage is directly related to the degree of hydration. The relative chemical shrinkage increase of all the TiO_2 cements compared to neat cement paste were calculated at 12 h

and 48 h after mixing, presented in Table 3.4. These results suggest that the TiO_2 particles increase the degree of hydration during the length of the test. Comparing percent increase of the shrinkage (Table 3.4) and the cumulative heat data (Table 3.3), the values are comparable, taking into account the variability of the chemical shrinkage data.

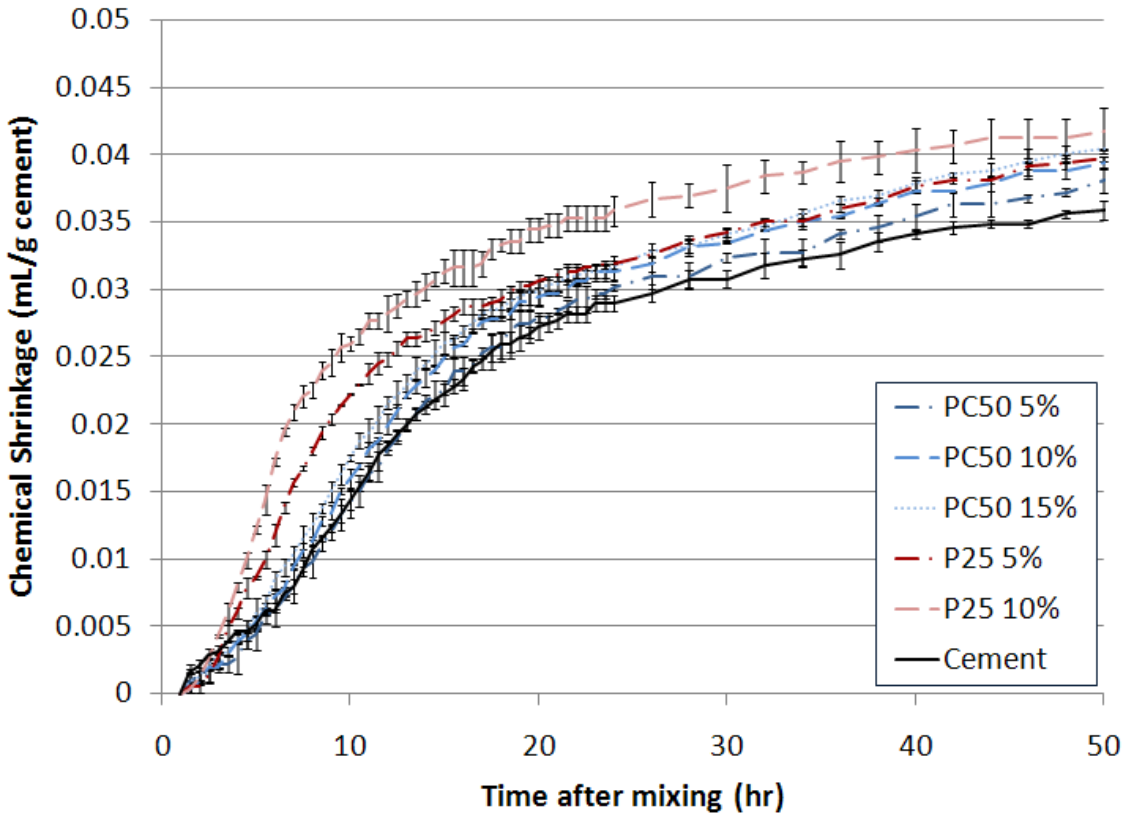

Figure 3.3 – Chemical shrinkage of P25 and PC50 blended cement pastes

Table 3.4 – Chemical shrinkage of P25 and PC50 modified cement pastes

		OPC	P25		PC50		
	TiO_2, %	0%	5%	10%	5%	10%	15%
12 h	Chemical shrinkage, mL/g cement	0.018	0.025	0.028	0.018	0.020	0.022
	Relative increase, %	-	34.52	52.97	-1.58	8.48	17.08
48 h	Chemical shrinkage, mL/g cement	0.036	0.039	0.041	0.037	0.039	0.040
	Relative increase, %	-	10.74	15.69	4.48	8.92	12.56

The samples containing P25 resulted in greater chemical shrinkage than the samples containing PC50. These results are supported by the assessments which showed that the degree of hydration of the P25 samples were greater than that of the PC50 samples at the same TiO_2 dosage rate. It is hypothesized, again, that the differences in dispersion affects the hydration rate and also the chemical shrinkage in these pastes. In addition, for both TiO_2's, the higher TiO_2 replacement rate resulted in a greater chemical shrinkage, which is again similar to the cumulative calorimetry data shown in Figure 3.2 (b).

Finally, the rate of hydration can be inferred from the slope of the chemical shrinkage curves. P25-containing samples show steeper slope than PC50 containing samples or control sample initially up to ~10 hours, indicating faster rate of reaction in its early hydration. This can be compared to Figure 3.2 (a), where the peak heights of P25-containing samples are higher than PC50-containing samples. These results suggest that the TiO_2 particles increase the degree of hydration during the first 80 hrs examined and

overcome any effect of dilution (i.e., reduction in cement content) up to addition level 10% for P25 and 15% for PC50.

3.3.3 Setting Time

Initial and final setting times of TiO_2-modified cement pastes were determined and compared to data for the neat cement paste control samples. All the samples that contained TiO_2 nanoparticles exhibited shorter final setting time than the control sample, as shown in Figure 3.4. Higher amounts of TiO_2 replacement lead to shorter time to final set, further indicating that chemically inert nanoparticles accelerate initial cement hydration, hence resulting more rapid stiffening of the matrix, even when used as cement replacement. The setting time results are also comparable to the calorimetry and chemical shrinkage results, where it was shown that the hydration rates of all the samples containing TiO_2 particles were accelerated and degree of hydration was increased compared to neat cement paste.

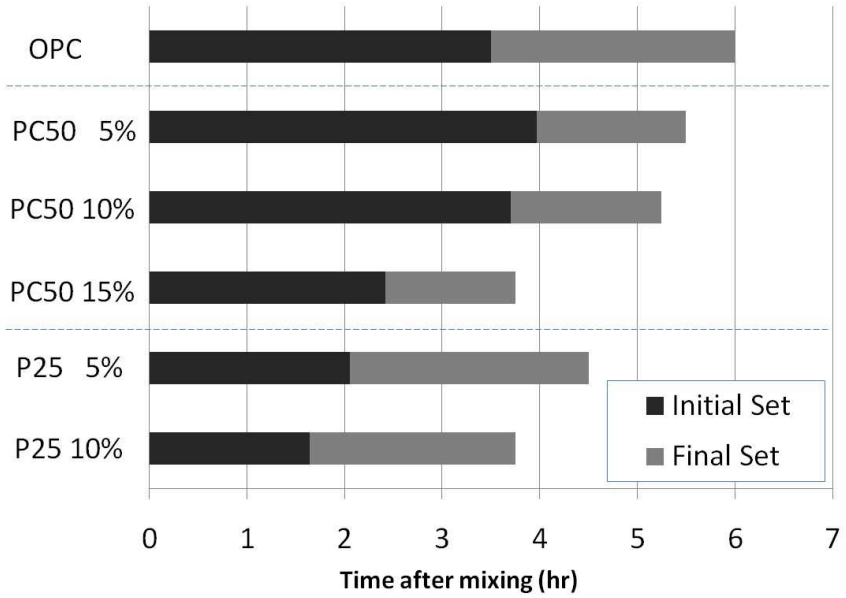

Figure 3.4 – Initial and final setting times of ordinary portland cement and TiO_2 modified cements

Observing the initial setting times of the samples, P25-containing cement pastes resulted in shorter initial setting times than the control sample as expected. Higher dosages of TiO_2 nanoparticles generally shortened the time to set. However, samples with PC50 did not follow the expected trend; samples with 5% and 10% PC50 resulted longer initial setting times than ordinary portland cement, showing about twice longer time to set than P25-containing cement paste at equivalent TiO_2 dosage. However, the sample containing 15% of PC50 resulted shorter initial setting time than OPC. This different behavior between the two TiO_2's might come, again, from variations in their dispersability or particle size distribution. It is proposed that the smaller particle size and larger surface area of the P25 particles provide a greater availability of nucleation sites, leading to faster hydration rate and shorter setting time. On the other hand, PC50 has a relatively larger particle size that might not contribute as much to the total surface area

available for nucleation. Also, surface treatments during production of different TiO_2's might have an effect in hydration rates. It is known that chloride and sulfate processes are the two most common manufacturing methods to extract and purify TiO_2 from ore [136], and those ions could have dissolved into the mixing water and affect hydration of cement [32]. Moreover, the TiO_2 replacement for cement causes a dilution effect, and this reduction in the cement content can contribute to the delayed initial setting time for the 5% and 10% cases. It can be understood that at higher dosages of PC50 enough additional surface area is provided allowing for the hydration reaction to be accelerated to an extent which overcomes the cement dilution effect.

Comparing the setting time data with calorimetry and chemical shrinkage data, it can be inferred that early hydration acceleration, or increase of degree of hydration (α), shown in Figures 3.2 and 3.3 does not necessarily relate to shorter setting time. This is because setting time accounts for decreased amounts of cement due to TiO_2 replacement, that tends to offset acceleration, while calorimetry and shrinkage data are normalized by gram of cement.

3.3.4 Compressive Strength

Compressive strength of cement cubes containing 0%, 5%, and 10% TiO_2 (P25) was measured at 1, 3, 7, 14, and 28 days of age at w/c=0.50 (Figure 3.5). In general, the average compressive strength for each composition increased until 14 days and reached a plateau thereafter at ~5500-6000 psi. The high standard deviation that is observed is likely due to the small physical specimen size. Imperfections such as air voids or uneven surfaces in small specimen could affect the strength more than larger specimen. In order

to compare samples with high standard deviations, single factor analysis of variance test (ANOVA test) was performed with data at 28 days of curing. Significance level was set to 5% and samples between 0%-5%, 5%-10%, and 0%-10% were compared. The P values were calculated to be 0.27, 0.76, and 0.44 for 0%-5%, 5%-10%, and 0%-10% cases respectively, all exceeding the significance level at 0.05. The results indicate that the compressive strength of each case at 28 days can be considered the same, despite the fact that 5% and 10% cases contain less amount of cement than the control. This suggests that the TiO_2-modified cement not only accelerates the early hydration rate as examined by calorimetry, shrinkage, and setting time testing, but also gives comparable strength to ordinary portland cement.

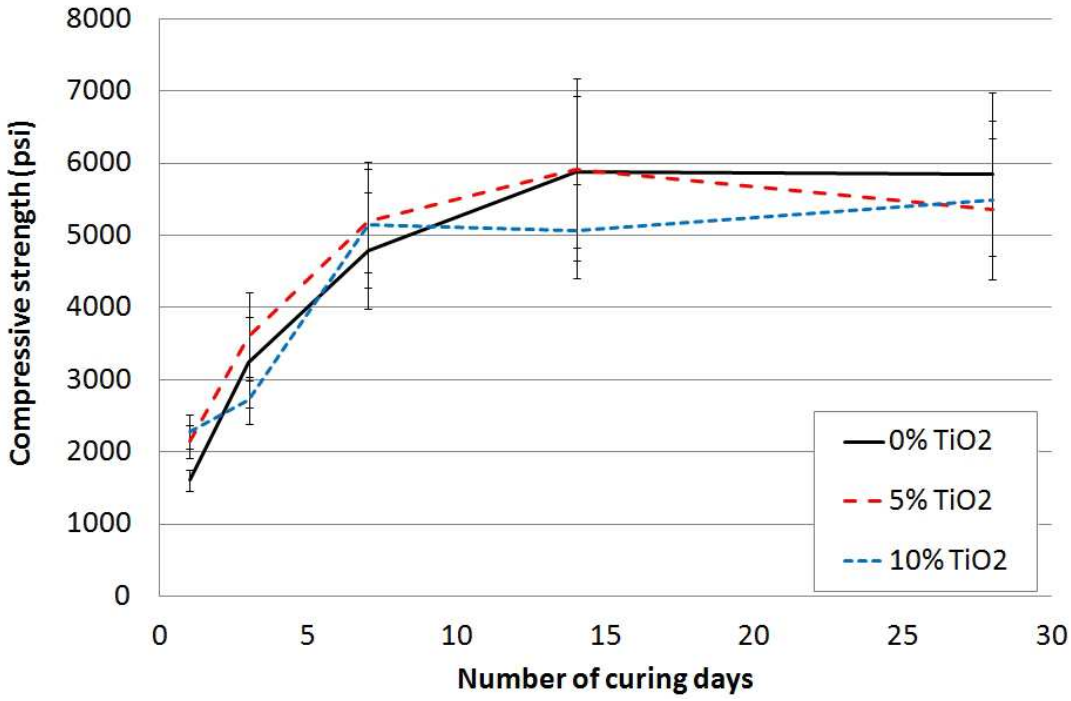

Figure 3.5 – Compressive strength of 0%, 5%, and 10% TiO_2-cement samples at w/c=0.50

Additional testing was performed to examine the effect of varying w/c on compressive strength at 28 days. The strength results are shown in Figure 3.6. From the figure, it can be concluded that the higher water content resulted in decreased strength at all TiO_2 addition rates. This is expected and generally known behavior because high water content increases porosity which decreases strength. Here, the trend of each w/c was examined with varying addition rates of TiO_2. In order to quantify the data, single factor ANOVA was performed again at 5% significant level. For the w/c=0.40 case, the P values were calculated to be 0.155 and 0.018 for 0%-5% and 5%-10% respectively, indicating that the strength was increased between 5% and 10%. In case of w/c=0.50, the P values were 0.330 and 0.017 for 0%-5% and 5%-10% respectively, indicating that strength decreased between 5% and 10%. In case of w/c=0.60, the strength were found to remain the same with the P values calculated to be 0.164 and 0.419 for 0%-5% and 5%-10% respectively. The strength increase with TiO_2 addition, as with the case of w/c=0.40, was also reported in literatures. Lackhoff et al. observed 20% strength increase on mortar cubes when the same type of TiO_2 was used at 10% and at w/c= 0.5 [120]. Nazari et al. also found that nano-TiO_2 addition up to 2% increased the compressive strength of concrete [137]. It is proposed that the strength enhancement of w/c=0.40 case can be explained by the addition of well-dispersed high surface nanoparticles, which gave more uniform and complete hydration of cement [32]. These nanoparticles might also improve particle packing of cement paste thus participate in increasing the strength, which compromise the lesser cement content [138, 139]. Interestingly, w/c=0.50 case resulted in decreasing compressive strength with increasing TiO_2 dosing rate. However, this can be

thought of as a minor decrease considering that no apparent strength decrease was found from the w/c=0.60 case. The slight decrease of strength found from w/c=0.50 case and possibly from w/c=0.60 case could be due to higher replacement rate of TiO_2 that resulted in decreased cement content. This is related to dilution effect and the strength is expected to decrease more at higher replacement level. These results demonstrate that addition of nano-TiO_2 up to 10 wt.% could potentially increase the compressive strength of cementitious materials at w/c=0.40 or lower, possibly due to microstructure modification or particle packing effect. Also, it was shown that TiO_2 replacements level up to 10% by mass of cement does not sacrifice strength at higher w/c up to w/c=0.60, despite the fact that the cement content is reduced by the substitution with TiO_2.

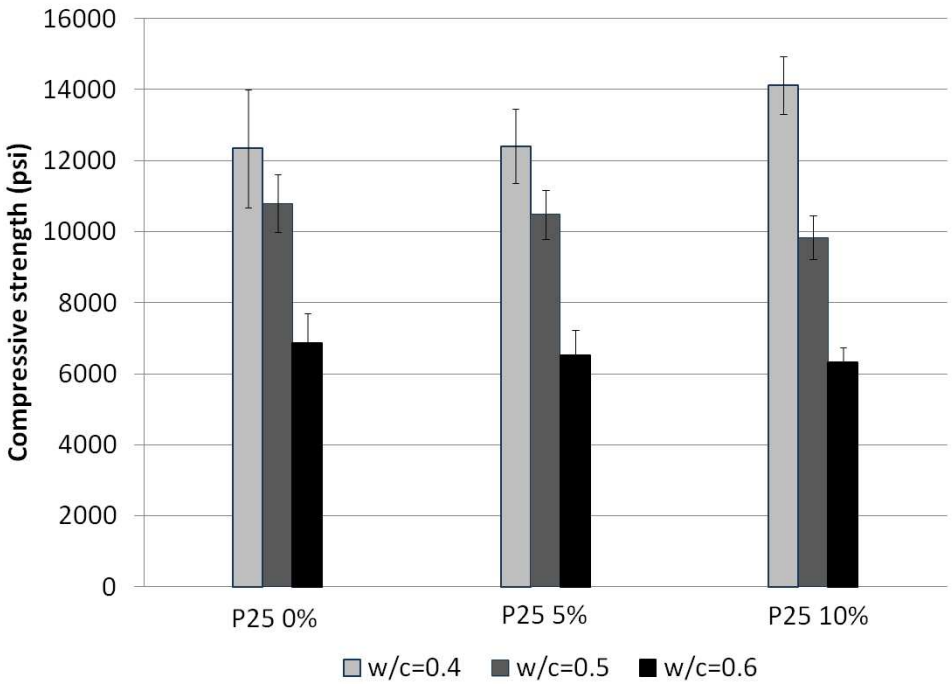

Figure 3.6 – Compressive strength of w/c = 0.40, 0.50, and 0.60 samples at 28 days

3.3.5 Microhardness

Figure 3.7 shows the surface microhardness of the 0%, 5%, and 10% TiO_2 (P25) containing cement paste samples at 1, 3, 7, 14, and 28 days of age. For all the samples, the hardness increased significantly until 14 days and reached a plateau, which is similar to the compressive strength development trend. However, unlike strength development, there is a considerable difference between samples with different TiO_2 usage rates. Specifically, the surface hardnesses of 5% and 10% TiO_2-cement samples were less than neat cement samples by 26% and 44% at 28 days of age. This reduction in surface hardness is significant, particularly considering the percentage of TiO_2 particles that replaced the cement.

In addition, the hardness development rate, or the slope of curve, is observed to be different. In all of the cases examined, an initial hardness of 8-9 was measured at 1 day. But the hardness of 0% case increased at a faster than the others, with the 10% case showing the slowest hardness development rate. It is likely that the lesser cement content in the paste with higher TiO_2 percentage could have affected the hardness. Some other factors such as poor bonding strength between TiO_2 powder and hydrated cement phases might have also influenced the overall hardness of the material.

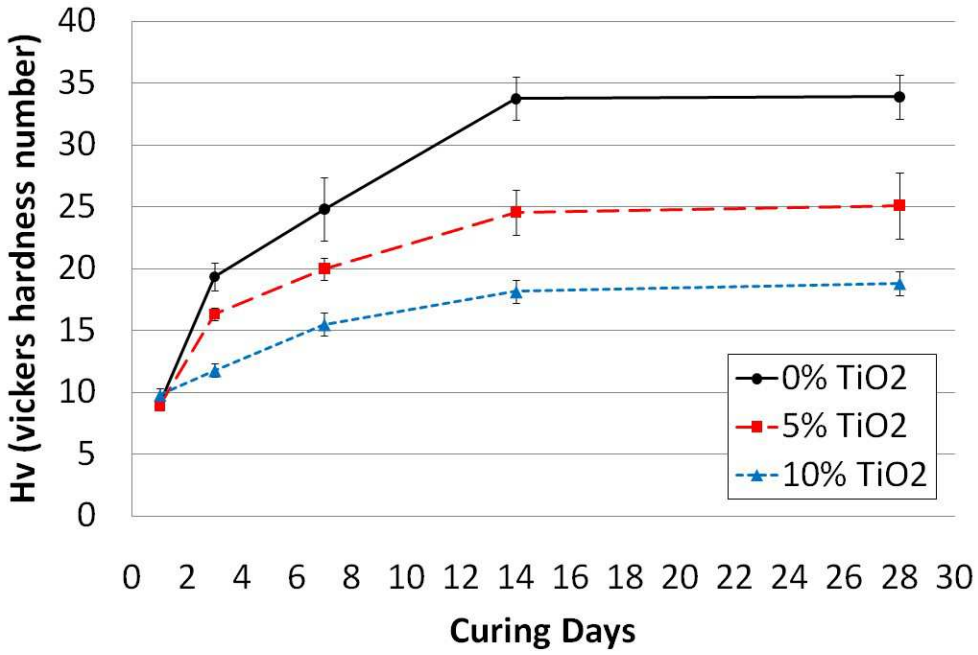

Figure 3.7 – Microhardness of 0%, 5%, and 10% TiO_2-cement samples

It is generally understood that microhardness of a cementitious materials is directly related to compressive strength [130, 140-142]. However, in this study, it is interesting to note that the lower hardness values associated with TiO_2 replacement are not predicted by comparing the compressive strength results for these pastes. Further, Vassou et al. reported that the abrasion resistance of concrete is directly related to the microhardness of a matrix [143]. This indicates that the samples with lower microhardness, such as in 10% TiO_2 case, may have poor abrasion resistance as concrete. However, there is also a general agreement that abrasion resistance increases with higher compressive strength [30, 144, 145], suggesting that the samples will have similar abrasion resistance.

In light of these conflicting indications regarding abrasion resistance, these results suggest that a more comprehensive investigation on abrasion resistance is warranted for

TiO_2 modified cement-based materials. To generally improve abrasion resistance, it is recommended that low w/c be used for high compressive strength and high hardness. Also, following proper finishing procedures and proper curing procedures should enhance abrasion resistance of TiO_2 modified cementitious materials [145].

3.4 Conclusions

TiO_2-containing cement paste samples were experimentally examined to assess early age behavior and hardened mechanical properties. Two different TiO_2's (P25 and PC50) were examined and their early age behavior was compared at different cement replacement rates. Based on the results of this study, the following conclusions are drawn:

- Early age (up to 80 hours) heat of hydration and chemical shrinkage data suggest that early hydration reaction rates were accelerated in the presence of TiO_2 nanoparticles. Higher TiO_2 dosages resulted greater acceleration (up to ~3.5 hrs) and increased degree of hydration (up to nearly 50% increase) compared to ordinary cement. From this study, the P25 accelerated the hydration more than the PC50, and also produced higher degree of hydration than PC50 modified cement samples, likely due to its greater dispersability.
- All of the TiO_2-modified cements examined exhibited shorter final setting time than the control. In terms of initial setting time, P25 samples had shorter setting time than control while 5% and 10% of PC50 samples had longer setting time. This suggests that setting behavior is again controlled by dispersability or particle size distribution.

- Use of TiO_2 nanoparticles (P25) in cementitious materials does not compromise compressive strength when added up to 10% weight replacement of cement at w/c of 0.50 and 0.60. Further, compressive strength increases with TiO_2 addition up to 10% in case of w/c=0.40.
- The microhardness of cement was heavily affected by TiO_2 dosage rates, unlike compressive strength. 10% weight replacement resulted 44% decreased hardness than control at 28 days. It is recommended that this type of materials be used in places where the chance of scratching or indenting is low. Relationship between hardness and surface roughness should also be investigated along with strength.

Observations such as above suggest that TiO_2 nanoparticles can be used in cementitious materials to alter various properties such as hydration rate, setting time, strength development, and hardness. These data suggest that the dosage rate and particle size distribution of TiO_2 nanoparticles, and perhaps other inert particles, can be optimized to achieve specific early age behavior as well as hardened properties.

3.5 References

12. Chen, J. and C.S. Poon, *Photocatalytic construction and building materials: From fundamentals to applications.* Building and Environment, 2009. **44**(9): p. 1899-1906.

13. Cassar, L., et al. *White cement for architectural concrete, possessing photocatalytic properties.* in *11th Int. Congr. on the Chemistry of Cement*, 2003. Durban.

14. Poon, C.S. and E. Cheung, *NO removal efficiency of photocatalytic paving blocks prepared with recycled materials.* Construction and Building Materials, 2007. **21**(8): p. 1746-1753.

15. Husken, G., M. Hunger, and H. Brouwers. *Comparative study on cementitious products containing titanium dioxide as photo-catalyst*. in *RILEM Int. Symp. on Photocatalysis, Environment and Construction Materials*, 2007. Italy.

16. Beeldens, A. *Air purification by road materials: Results of the test project in Antwerp*. in *International RILEM Symposium on Photocatalysis, Environment, and Construction Materials*, 2007. Florence, Italy.

17. Maggos, T., et al., *Photocatalytic degradation of NO_x in a pilot street canyon configuration using TiO_2-mortar panels.* Environmental Monitoring and Assessment, 2008. **136**(1-3): p. 35-44.

18. Fujishima, A. and X.T. Zhang, *Titanium dioxide photocatalysis: present situation and future approaches.* Comptes Rendus Chimie, 2006. **9**(5-6): p. 750-760.

21. Chen, J. and C.S. Poon, *Photocatalytic activity of titanium dioxide modified concrete materials - Influence of utilizing recycled glass cullets as aggregates.* Journal of Environmental Management, 2009. **90**(11): p. 3436-3442.

22. Ramirez, A.M., et al., *Titanium dioxide coated cementitious materials for air purifying purposes: Preparation, characterization and toluene removal potential.* Building and Environment, 2010. **45**(4): p. 832-838.

30. Li, H., M.H. Zhang, and J.P. Ou, *Abrasion resistance of concrete containing nano-particles for pavement.* Wear, 2006. **260**(11-12): p. 1262-1266.

32. Lee, B.Y. and K.E. Kurtis, *Influence of TiO_2 Nanoparticles on Early C_3S Hydration.* Journal of the American Ceramic Society, 2010. **93**(10): p. 3399-3405.

43. Strini, A., S. Cassese, and L. Schiavi, *Measurement of benzene, toluene, ethylbenzene and o-xylene gas phase photodegradation by titanium dioxide dispersed in cementitious materials using a mixed flow reactor.* Applied Catalysis B-Environmental, 2005. **61**(1-2): p. 90-97.

44. Wang, S., H.M. Ang, and M.O. Tade, *Volatile organic compounds in indoor environment and photocatalytic oxidation: State of the art.* Environment International, 2007. **33**: p. 694-705.

92. Thomas, J.J., *A new approach to modeling the nucleation and growth kinetics of tricalcium silicate hydration.* Journal of the American Ceramic Society, 2007. **90**(10): p. 3282-3288.

120. Lackhoff, M., et al., *Photocatalytic activity of semiconductor-modified cement-influence of semiconductor type and cement ageing.* Applied Catalysis B-Environmental, 2003. **43**(3): p. 205-216.

121. Fujishima, A. and Z. Zhang, *Titanium dioxide photocatalysis: present situation and future approaches.* Comptes Rendus Chimie 8, 2005.

122. Husken, G., M. Hunger, and H.J.H. Brouwers, *Experimental study of photocatalytic concrete products for air purification.* Building and Environment, 2009. **44**(12): p. 2463-2474.

123. Folli, A., et al., *Engineering photocatalytic cements: Understanding TiO_2 surface chemistry to control and modulate photocatalytic performances.* Journal of the American Ceramic Society, 2010. **93**(10): p. 3360-3369.

124. Lee, B.Y., et al., *Influence of TiO_2 Nanoparticles on Early C_3S Hydration*, in *ACI Convention*, K. Sobolev and M.R. Taha, Editors. 2009, ACI SP 267-4: New Orleans, LA. p. 35-44.

125. Hassan, M.M., et al., *Evaluation of the durability of titanium dioxide photocatalyst coating for concrete pavement.* Construction and Building Materials, 2010. **24**(8): p. 1456-1461.

126. ASTM, *C 191 Standard test methods for time of setting of hydraulic cement by vicat needle*, 2008.

127. ASTM, *C 1702 Standard test method for measurement of heat of hydration of hydraulic cementitious materials using isothermal conduction calorimetry*, 2008.

128. ASTM, *C 1608 Standard test method for chemical shrinkage of hydraulic cement paste.* 2007.

129. ASTM, *C 187 Standard test method for normal consistency of hydraulic cement*, 2004.

130. Igarashi, S., A. Bentur, and S. Mindess, *Microhardness testing of cementitious materials.* Advanced Cement Based Materials, 1996. **4**(2): p. 48-57.

131. Trtik, P. and P.J.M. Bartos, *Micromechanical properties of cementitious composites.* Materials and Structures, 1999. **32**(219): p. 388-393.

132. Cross, W.M., et al., *Microhardness testing of fiber-reinforced cement paste.* Aci Materials Journal, 2000. **97**(2): p. 162-167.

133. Hossain, K.M.A. and M. Lachemi, *Strength, durability and micro-structural aspects of high performance volcanic ash concrete.* Cement and Concrete Research, 2007. **37**(5): p. 759-766.

134. ASTM, *C 1327 Standard test method for Vickers indentation hardness of advanced ceramics.* 2008.

135. Bensted, J. and P. Barnes, *Structure and performance of cements*. 2nd ed. 2002, London: Spon Press.

136. Chernet, T., *Effect of mineralogy and texture in the TiO_2 pigment production process of the Tellnes ilmenite concentrate.* Mineralogy and Petrology, 1999. **67**: p. 21-32.

137. Nazari, A., et al., *Assessment of the effects of the cement paste composite in presence TiO_2 nanoparticles.* Journal of American Science, 2010. **6**(4): p. 43-46.

138. Goldman, A. and A. Bentur, *The influence of microfillers on enhancement of concrete strength.* Cement And Concrete Research, 1993. **23**(4): p. 962-972.

139. Isaia, G.C., A.L.G. Gastaldini, and R. Moraes, *Physical and pozzolanic action of mineral additions on the mechanical strength of high-performance concrete.* Cement and Concrete Composites, 2003. **25**(1): p. 69-76.

140. Beaudoin, J.J. and R.F. Feldman, *A study of mechanical properties of autoclaved calcium silicate systems.* Cement and Concrete Research, 1975. **5**(2): p. 103-118.

141. Feldman, R.F. and H. Cheng-Yi, *Properties of portland cement-silica fume pastes 2. Mechanical properties.* Cement and Concrete Research, 1985. **15**(6): p. 943-952.

142. Hossain, K.M.A., *Macro- and microstructural investigations on strength and durability of pumice concrete at high temperature.* Journal of Materials in Civil Engineering, 2006. **18**(4): p. 527-536.

143. Vassou, V.C., N.R. Short, and R.J. Kettle, *Microstructural investigations of fiber-reinforced into the abrasion resistance concrete floors.* Journal of Materials in Civil Engineering, 2008. **20**(2): p. 157-168.

144. Naik, T.R., S.S. Singh, and M.M. Hossain, *Abrasion resistance of high-strength concrete made with class C fly ash.* Aci Materials Journal, 1995. **92**(6): p. 649-659.

145. ACI, *201.2R-08: Guide to Durable Concrete,* 2008, American Concrete Institute.

CHAPTER 4

INFLUENCE OF TiO_2 NANOPARTICLES ON EARLY ALITE AND BELITE HYDRATION

4.1 Introduction

In this research, the influence of addition of chemically inert nano-anatase titanium dioxide (TiO_2) particles on early age hydration of tricalcium silicate (C_3S, or alite) and dicalcium silicate (C_2S, or belite) was examined. Tricalcium silicate ($3CaO \cdot SiO_2$ or C_3S) is the largest component by mass (~50-70%) of ordinary portland cement, followed by dicalcium silicate ($3CaO \cdot SiO_2$ or C_2S). These phases hydrate to form calcium silicate hydrate (C-S-H), as well as calcium hydroxide. Because C-S-H is the primary binding component in cement-based materials, improved understanding of the hydration kinetics of C_3S and C_2S is central to understanding behavior of cementitious composites [80, 146-148].

Worldwide, applications of photocatalytic TiO_2, such as the nano-anatase form examined here, are increasing [14, 16, 50, 149], due to its ability to impart smog-abating, self-cleaning, and biocidal capacities to ordinary cement-based materials. The photocatalytic reactions are especially efficient in nano-crystalline form [8, 18]. A recent preliminary study [50] has suggested that the inert TiO_2 nanoparticles may accelerate portland cement hydration, but the mechanism for this effect was not examined. The modification of the rate of hydration forms the basis for anticipating the influence of such

chemically inert nanoparticles on setting time, rate of strength gain, dimensional stability, and durability.

In terms of the C_2S hydration, the proposed acceleratory effect could further affect the amount of carbon dioxide (CO_2) emissions and contribute to sustainable development. Cement production produces about 5% of the total global anthropogenic CO_2 [150]. Production of clinkers that are relatively rich in belite (β-C_2S), at the expense of the typically more common alite (C_3S), can be part of a comprehensive strategy to decrease CO_2 emissions associated with cement manufacture both by allowing firing at lower temperatures (saving energy and CO_2 emissions associated with energy production) and by reducing the amount of $CaCO_3$ decomposed [151]. Because the reaction rate of belite is slow compared to alite, many researchers have been interested in improving strength development rate of belite-rich cements at early ages. The influence of reactive agglomerated dry nanoalumina particles and reactive colloidal nanoalumina on belite cements was examined by Campillo et al. [34]. The mechanical strength of mortar samples increased by 142% and 84% at 7 days and 119% and 113% at 28 days for dry alumina and colloidal alumina respectively compared to control sample, likely due to a refinement of the microstructure and the formation of additional phases. The influence of silica (SiO_2) nanoparticles to ordinary portland cement has been examined by several researchers [26, 27, 152], and nano-SiO_2 was found to improve the mechanical properties of cement-based materials.

In this study, the effect of addition of chemically inert TiO_2 nanoparticles on C_3S and C_2S hydration is examined. The objective of this research is to investigate whether the additional surface area provided by nano-sized TiO_2 influences the C_3S and C_2S

hydration examined by isothermal calorimetry, and if it could be captured by mathematical modeling in case of C_3S. The aim is to better understand the influence of the nanoparticles on hydration of portland cement. Additionally, results here could potentially extend the contributions of photocatalytic titania nanoparticles with respect to sustainable development.

The first part of this study experimentally investigates the hydration rate of the C_3S and C_2S in the presence of nano-TiO_2 by isothermal calorimetry method. The later part of this study uses C_3S calorimetry data and examines kinetics of C_3S hydration by mathematical modeling.

4.2 Theoretical Background

The early hydration kinetics of cement are of fundamental importance to understanding the behavior of cement-based materials, as they influence nano/microstructural evolution, setting time, dimensional stability, strength development, and durability. Despite the practical importance of the kinetics of cement hydration, early age reactions of cement-based materials remain imperfectly understood [78-80]. Several mathematical models have been applied however, to characterize the hydration kinetics of the principal component of portland cement, C_3S. Here, the "Avrami" nucleation and growth model [81-83] (sometime also denoted as the "JMAK" model [84]) and the boundary nucleation model (BN model) [85] will be considered for both the C_3S and C_2S hydration.

4.2.1 Avrami Nucleation and Growth Model

Among others, the Avrami nucleation and growth model [81-83] has been most widely accepted to describe the early age hydration rate for tricalcium silicate [86-89]. The theory was first treated by Kolmogorov [90], Johnson and Mehl [91], and Avrami [81-83] to explain the kinetics of phase change of metals. The main assumptions made were that the new phase is nucleated by germ nuclei and that the grain centers of the new phase are randomly distributed throughout the matrix. Due to its simple mathematical form, the theory has been widely adapted for C_3S hydration [86-89]. Only the final forms of the equations will be introduced here.

The transformed volume fraction X as a function of time can be written as,

$$X = 1 - \exp\left[-(k_{avr}t)^n\right] \tag{4.1}$$

where the effective rate constant k_{avr}, as proposed by Avrami, is a function of constant linear growth rate, G, and either of the rate of nucleation per unit of untransformed volume, I_v, or the number of nuclei per unit volume, N_v^0, and n is an exponent that depends on the dimensionality of the product that forms.

The hydration rate, which can be obtained by differentiating Equation (4.1) with respect to time, can be written as,

$$R = \dot{A}nk_{avr}^n(t-t_0)^{n-1}\exp(-[k_{avr}(t-t_0)]^n) \tag{4.2}$$

where R is the hydration rate, Ȧ is a normalization constant to match isothermal calorimetry data, and t_0 is the time delay between the time of mixing and the start of nucleation and growth kinetics. While the Avrami model has been used widely to describe C_3S hydration, the deceleration period of the rate curve is not accurately described by this model. The heterogeneous nucleation process that occurs during cement hydration may not be best described by a random or homogeneous nucleation assumption [92, 93].

4.2.2 Boundary Nucleation Model

Thomas [92] recently proposed a mathematical C_3S hydration model based on the boundary nucleation model (BN model) developed by Cahn [85]. The theory, which was used originally to describe a solid-solid phase transformation in a polycrystalline material, has been shown to give a better approximation of early age hydration kinetics of C_3S than the Avrami model. The key assumption is that nucleation is permitted to occur only on grain boundaries, unlike the Avrami model which assumes that nucleation occurs at randomly distributed locations everywhere within the untransformed volume. Experimental observations [94, 95] of the outward growth of hydration products from the hydrating cement grains confirm heterogeneous nucleation. The BN model also accounts for effect of the surface area of the starting material, which in the case of hydrating cement or C_3S is known to have a strong effect on the hydration kinetics [96, 97]. For the BN model, the transformed volume fraction as a function of time, *X*, is given by:

$$X = 1 - \exp\left[-2O_v^B \int_0^{Gt} \left(1 - \exp\left(-Y^e\right)\right) dy \right] \tag{4.3}$$

where $$Y^e = \frac{\pi I_B}{3} G^2 t^3 \left[1 - \frac{3y^2}{G^2 t^2} + \frac{2y^3}{G^3 t^3} \right] \quad \text{(if } t > y/G\text{)}$$

$$Y^e = 0 \quad \text{(if } t < y/G\text{)}$$

Note that y and Y^e are temporary variables that disappear after integration. In Equation (4.3), X depends on just three well-defined physical parameters: G, the linear growth rate of transformed phase, I_B, the nucleation rate per unit area of untransformed boundary, and O_v^B, the boundary area per unit volume.

In order to apply the BN model to C_3S hydration rate data, some slight modifications must be made [92]. The integration in Equation (4.3) must be performed numerically, and then Equation (4.3) should be differentiated numerically with respect to time to obtain the transformation rate, dX/dt. Here, the normalization constant Ȧ and the time constant t_0, described above in conjunction with the Avrami model (Equation (4.2)), are also introduced. Note that this is a modified version of Thomas's equation [92] so that time delay t_0 can be introduced.

The three physical parameters O_v^B, I_B, and G are correlated such that the kinetic profile is described by two independent rate constants k_B and k_G as proposed by Thomas [92]:

$$k_B = \left(I_B O_v^B\right)^{1/4} G^{3/4} \tag{4.4}$$

$$k_G = O_v^B G$$

$$k_B / k_G = \frac{(I_B/G)^{0.25}}{(O_v^B)^{0.75}}$$

If any one of the physical parameters in Equation (4.4) are known independently, then the other two can be calculated from the fitted values of the rate constants. For the case of a hydrating C_3S paste, the value of O_v^B can be calculated by dividing the measured surface area of the powders by the calculated volume occupied by the hydration products after complete hydration, allowing G and I_B to be determined from the fits.

Each of the rate constants represents different physical behavior: k_B describes the rate of transformation on the grain boundaries (the surface of particles), whereas k_G describes the rate of transformation in the bulk matrix (the pore space between the particles). The ratio of these two rate constants (k_B/k_G) determines the shape of the rate curve and can be used to identify the type of kinetic behavior. Unlike the curve from Avrami model which is symmetrical in shape, the k_B/k_G ratio of BN model gives a "skewness" to the curve, which better approximates actual kinetic behavior, especially in the deceleration period. As k_B/k_G approaches zero, it can be predicted that the hydrated products will form evenly throughout the paste, approaching the conditions of the Avrami model. As k_B/k_G increases, it can be predicted that the hydrated products will be densely populated on or very near the nucleation sites (i.e., the C_3S surface in the case of C_3S hydration). Figure 4.1 shows graphically the influence of k_B/k_G value of 0.1, 1.3, and 3 on product formation during C_3S hydration.

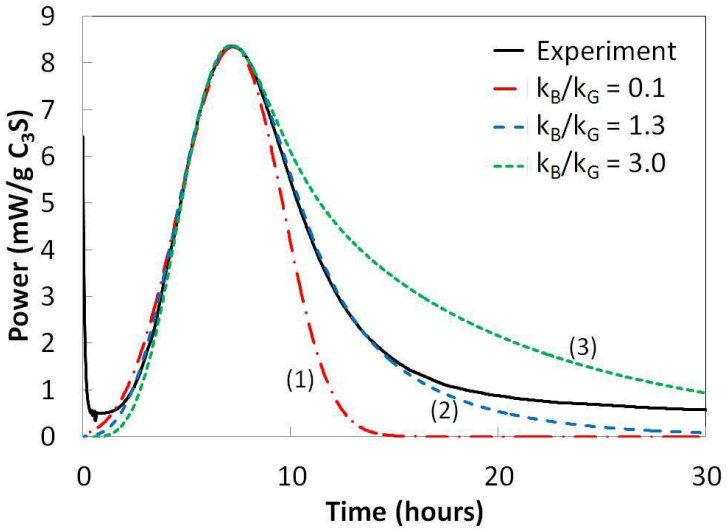

Figure 4.1 — Boundary nucleation model fits to experimental rate curve at (1) $k_B/k_G = 0.1$, (2) $k_B/k_G = 1.3$, and (3) $k_B/k_G = 3$

4.3 Materials and Experimental Procedure

Pure tricalcium silicate (C_3S) powder was obtained from Mineral Research Processing in Meyzieu, France. Sample purity was determined to be 99.68% by quantitative x-ray diffraction (QXRD) under Cu-Kα radiation (Figure 4.2). Pure belite (β-C_2S) powder, stabilized by boron trioxide (B_2O_3), was obtained from CTLGroup in Skokie, IL; this is the form of dicalcium silicate (C_2S) typically found in portland cement. Sample purity was 100.00% determined by QXRD under Cu-Kα radiation (Figure 4.3). The belite powder was ground to 100% passing No.325 sieve (45μm). The anatase titanium dioxide used (AMT-100 from Tayca Corp) was 93% pure, with an average crystal size of 6 nm and a pH of 7.0, as stated by the manufacturer. A neutral form of TiO_2 was utilized for this study to avoid any possible effect of acidity on hydration rate. ASTM C 150 Type I portland cement was used for a comparative study, the potential

Bogue composition of which was 51.30% C_3S, 19.73% C_2S, 8.01% C_3A, and 9.41% C_4AF. (Note that the cement chemistry notations of these oxides are defined as C=CaO, S=SiO_2, F=Fe_2O_3, and A=Al_2O_3.)

The nitrogen BET surface area of the C_3S, C_2S and the TiO_2 were measured at -196°C using a surface area and porosimetry analyzer (ASAP 2020, Micromeritics, Norcross, GA). The samples were degassed at 200°C for 18 hours. The BET surface area of the C_3S, C_2S and the TiO_2 was measured to be 1.59 m^2/g, 2.81m^2/g, and 611.54m^2/g respectively. Particle size distribution of TiO_2 was measured in water by Zetasizer Nano (Malvern Instruments, UK) (Figure 4.4). In order to better disperse the TiO_2 particles, superplasticizer was used and the solution was ultrasonicated for 1 hour prior to the measurement. Note that the measured particle size of TiO_2 is in micro-scale, which is likely due to agglomeration.

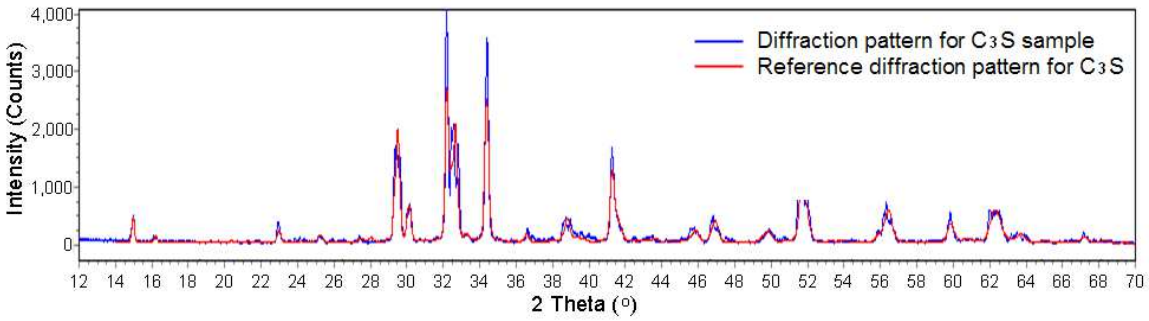

Figure 4.2 — Diffraction pattern for C_3S sample compared to reference pattern for C_3S

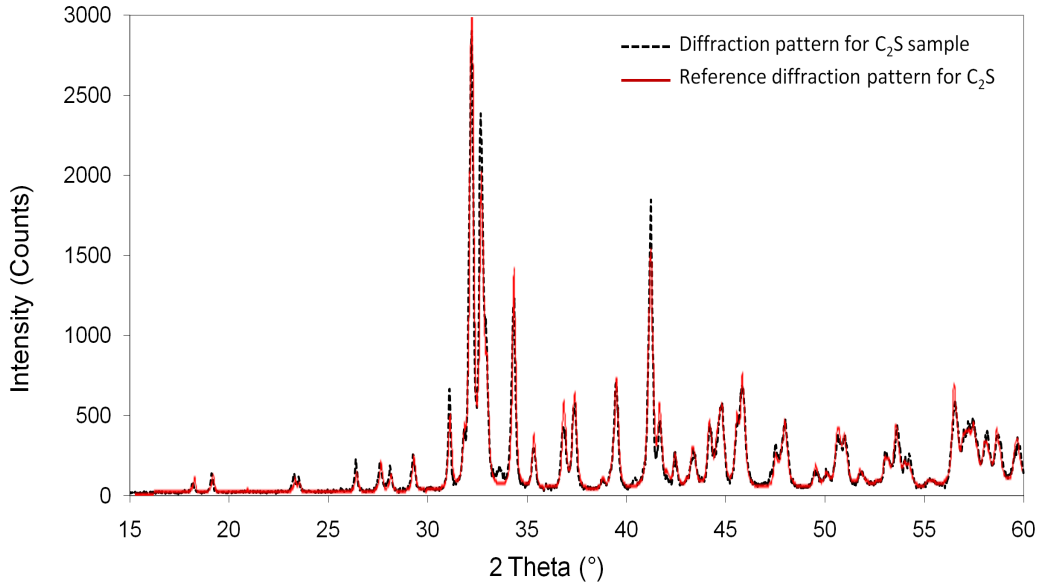

Figure 4.3 — Diffraction pattern for C_2S sample compared to reference pattern for C_2S

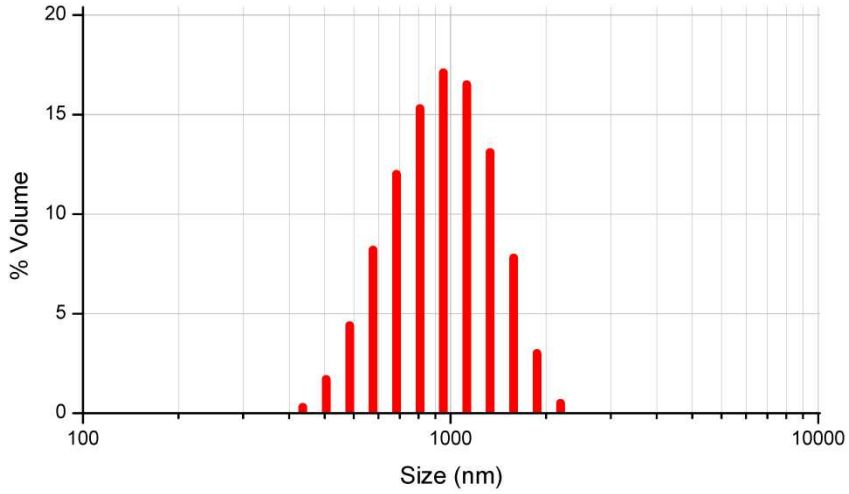

Figure 4.4 — Particle size distribution of TiO_2 powder

Four different C_3S pastes were prepared at 0, 5, 10, and 15% addition rate of TiO_2 by mass. It should be noted that the TiO_2 was dosed in addition to, not by weight replacement for, C_3S. This approach simplifies interpretation of calorimetry data by keeping the C_3S content constant – and hence the cement surface area constant – amongst

the samples, while allowing for the examination of increasing amounts of chemically inert TiO_2. The water-to-cement ratio (w/c) was kept constant at 0.50, which resulted in a stiffer mix as more of the high surface area TiO_2 was added.

Similarly, three different C_2S pastes were prepared. Three C_2S pastes were prepared at 0%, 5%, and 10% addition of TiO_2 by mass of C_2S, each added with 2% calcium chloride ($CaCl_2$) to accelerate the reaction [153-156]. The accelerator addition was made in an attempt to make results available at an earlier age. Again, TiO_2 was added to, rather than in replacement for, C_2S to better understand and compare the effect of addition of chemically non-reactive nanoparticles. Additionally, one C_2S paste was prepared without either TiO_2 or $CaCl_2$ as a control. All the pastes were mixed at water-to-cement ratio (w/c) of 0.50.

To prepare the samples, all materials and mixing equipment were equilibrated at 20°C for 24h before the testing. In case of the C_2S pastes, the $CaCl_2$ solution was first made with deionized water at 4% mass aqueous solution. It resulted in a 2% mass addition of $CaCl_2$ with respect to the mass of C_2S for the corresponding samples. Then, TiO_2 powder was added to the solution and hand mixed for 1 min for dispersion. Next, C_3S or C_2S powder was added and hand mixed for another 2 min. Samples were put in plastic ampoules and placed into the calorimeter less than 5 minutes after mixing with C_3S or C_2S. The calorimetry data from the initial 15 minutes after mixing were excluded as some time is required for the samples to become equilibrated within the instrument. The identical procedure was performed on ordinary portland cement pastes with 0, 5, 10, and 15% TiO_2 addition for the comparative study. The heat of hydration was measured by isothermal calorimetry (TAM AIR, TA instruments, New Castle, DE) at 20°C, with a

precision of ±20μW and accuracy greater than 95%.

When operating the calorimeter, special handling was employed for the C_2S pastes, because of very slow and subtle hydration reaction. Each channel of the isothermal heat conduction calorimeter is constructed in twin configuration with one side for the sample and the other side for a static reference. The heat evolution is measured by comparing the difference between the heat flow of the sample and reference ampoules. In order to ensure a stable base line and to accurately acquire long term heat data, an inert material with approximately the same heat capacity as the sample was placed in the reference ampoule [157, 158]. Heat capacity of reference ampoules were matched with sample ampoules by using deionized water of equivalent heat capacity in reference ampoules as sample pastes. This method facilitates more accurate measurements of the heat of early C_2S hydration as compared to using empty reference ampoules. The specific heat of fresh C_2S paste containing TiO_2 powder (C_p^{paste}) can be calculated according to simple law of mixtures [159] as:

$$C_p^{paste} = x^{water} C_p^{water} + x^{C_2S} C_p^{C_2S} + x^{TiO_2} C_p^{TiO_2} \quad (4.5)$$

where x^{water}, x^{C2S}, x^{TiO2}*: mass fraction of water, C_2S, and TiO_2 in paste respectively;* C_p^{water}, C_p^{C2S}, C_p^{TiO2}*: specific heat of water, C_2S, and TiO_2 respectively.* For this study, 4.18 J/(gK) was used for C_p^{water}, 0.74 J/(gK) was used for C_p^{C2S} [160] after linear interpolation, and 0.71 J/(gK) was used for C_p^{TiO2}, all at 20°C. The calculated specific heat of C_2S pastes that were used were 1.89 J/(gK), 1.85 J/(gK), and 1.81 J/(gK) for 0%,

5%, and 10% TiO_2-C_2S pastes respectively. The effect of addition of $CaCl_2$ was neglected in this calculation due to its small contribution.

4.4 Results and Discussion

4.4.1 C_3S Calorimetry Data

Figure 4.5 (a) and (b) show the rate of hydration per gram of C_3S and ordinary portland cement respectively, for the first 30h after mixing for each of the pastes examined; corresponding cumulative heat data for the first 60h is presented in Figure 4.6 (a) and (b). Recall that the C_3S/cement content and w/c for each paste remains constant, while the dosage of TiO_2 nanoparticles varies among 0, 5, 10, and 15% by mass of C_3S or cement.

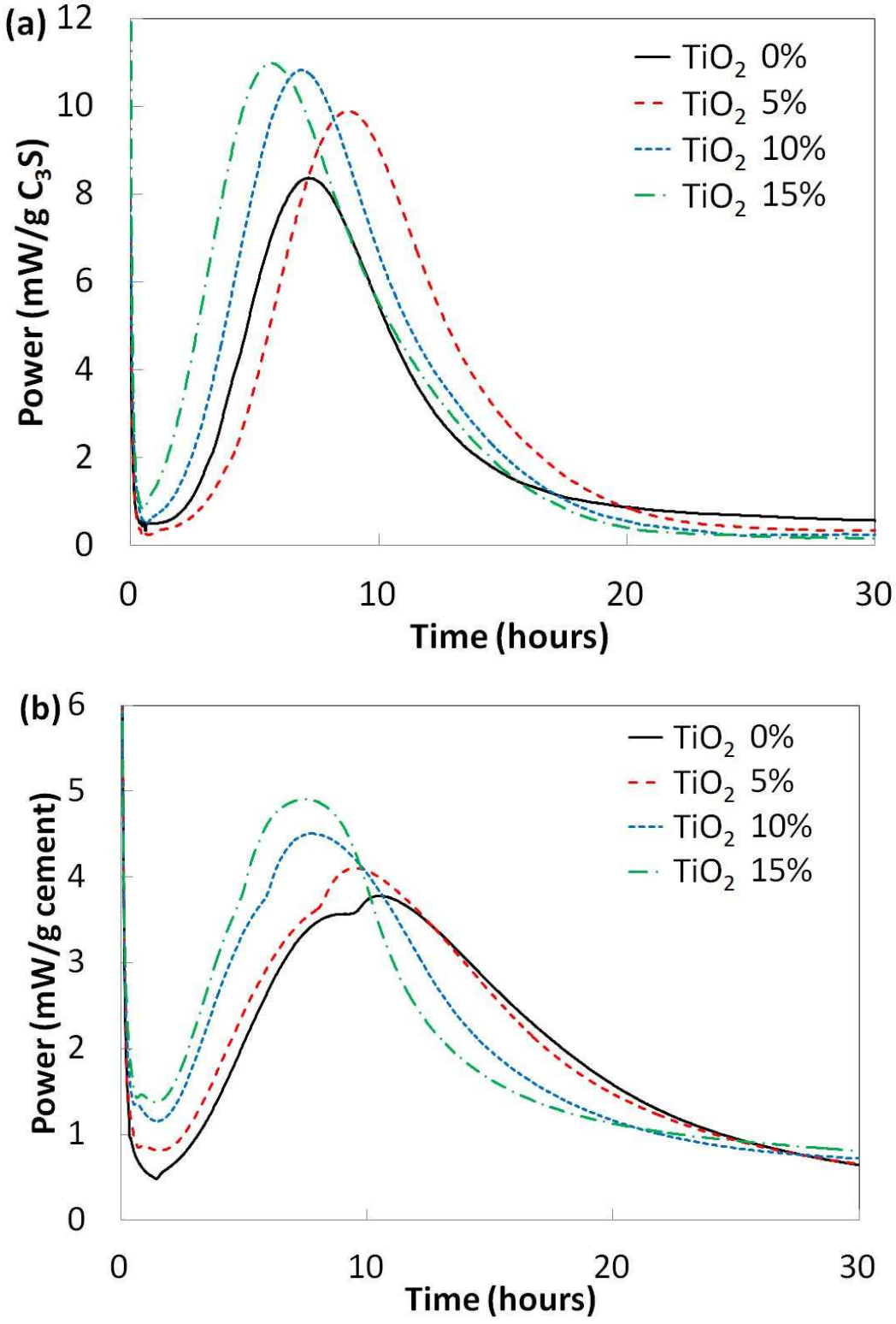

Figure 4.5 — (a) Hydration rate of TiO_2-blended C_3S pastes

(b) Hydration rate of TiO_2-blended cement pastes

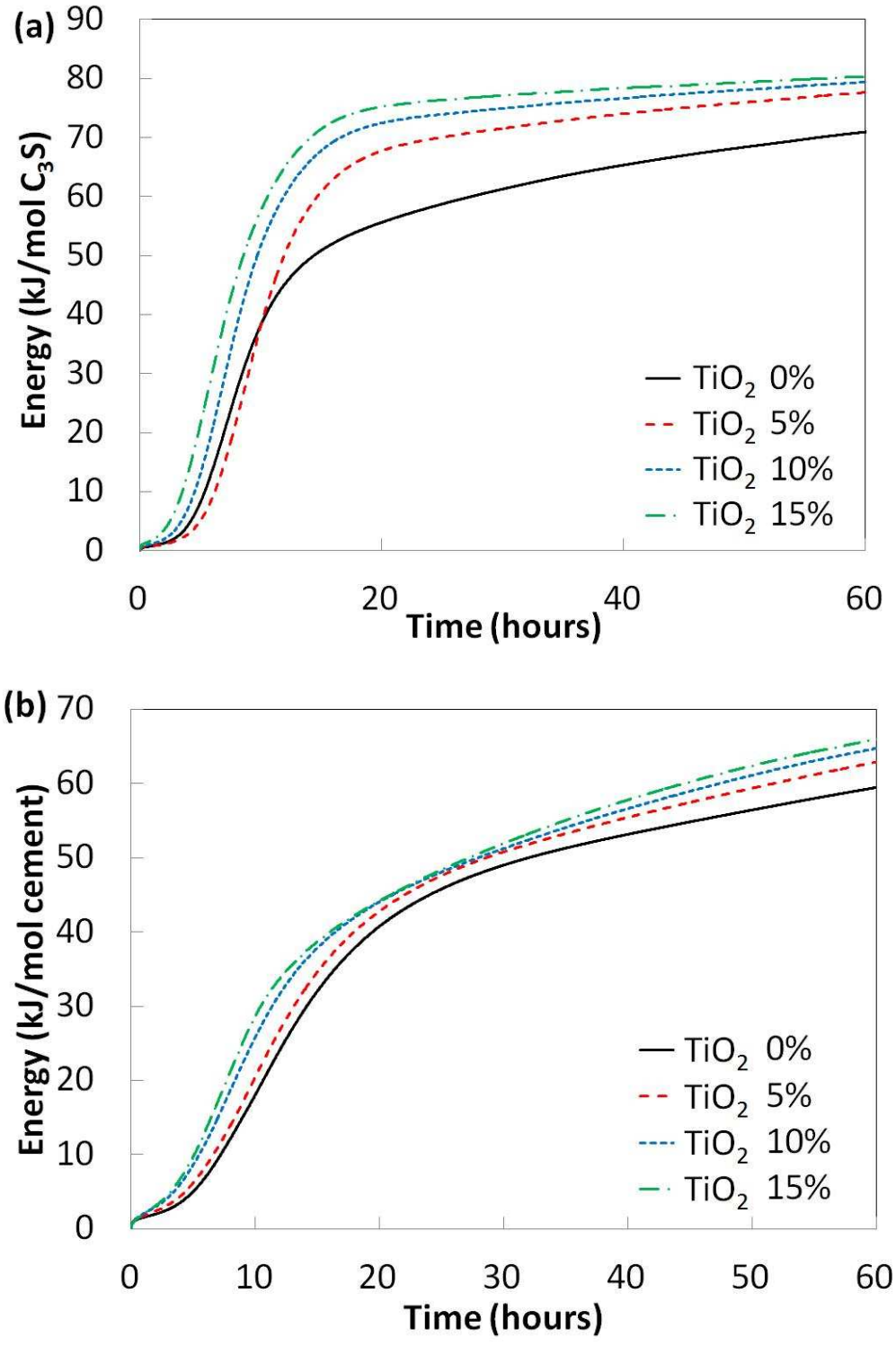

Figure 4.6 — (a) Cumulative heat of hydration of TiO_2-blended C_3S pastes

(b) Cumulative heat of hydration of TiO_2-blended cement pastes

These calorimetry data for C_3S pastes show that the rate peak heights (or greatest power evolved with time) were increased with the addition of the inert TiO_2 nanoparticles. The increases in peak height were 18, 29, and 31%, when comparing the 5, 10, and 15% TiO_2 cases to pure C_3S paste. The increases were greater than in case of cement pastes, where C_3S comprised ~50% of the cement by mass. Increases of 9, 19, and 30% in peak height at 5, 10, and 15% TiO_2 addition were found when compared to the ordinary cement paste.

When examining the time at which the peak heights occur, differences in behavior are noticed depending upon the amount of TiO_2 introduced to the paste. The peaks in the C_3S rate curve occur at 7.18, 8.78, 6.87, and 5.67 hrs after mixing, respectively, for 0, 5, 10, and 15% TiO_2 cases. That is, for the 10 and 15% TiO_2 pastes, the occurrences of these peaks were accelerated by 19 and 91 minutes. In contrast, a 96-minute delay in reaching this peak height was observed in the 5% TiO_2 paste. This delay in the 5% TiO_2 case also resulted in a lengthening of the duration of the "induction period [161]." It should be noted that this delay was not seen with ordinary portland cement pastes with TiO_2 or in the C_3S cases with higher fractions of TiO_2.

The apparent initial retardation effect – where a longer induction period is found but without a reduction rate peak heights – for the 5% TiO_2 case warrants further consideration. Most inorganic hydration retarding admixtures function by forming protective layers at the cement grain surface, limiting the rate of early dissolution. Specifically, such admixtures function by adding anions such as SO_4^{2-}, CO_3^{2-}, PO_4^{3-}, and F^-, which will form calcium salts of sufficiently low solubility; when these precipitate on the surface of cement or, in this case, C_3S grains, early hydration is slowed [161].

Knowing that the “sulfate process” is one of the most common manufacturing methods to extract and purify TiO_2 from ore [136], it may be hypothesized that sulfate ions present on the surface of TiO_2 could be dissolved into the mixing water and later adsorbed onto C_3S particles or precipitated into insoluble calcium sulfate where the calcium ions would be provided during the initial dissolution of the C_3S. In ordinary portland cement pastes, this retardation effect is likely insignificant because the sulfate ions are preferably consumed by the also rapidly reacting tricalcium aluminate (C_3A) phase. Thus, it is proposed that the retardation observed in this study with the 5% TiO_2 addition can be considered as an artifact of a highly simplified system, containing C_3S only. Furthermore, it is proposed that at the higher addition rates (10 and 15%), the additional nucleation sites provided (as will be discussed further below) promote hydration reactions, and counteract or overwhelm the retardation effect, showing a net acceleration.

A simple experiment was performed using ICP-OES (Optima 7300 DV, Perkin Elmer) to detect the presence of ions which could act to retard hydration. TiO_2 was mixed with deionized water with the same mass proportion as the 10% TiO_2-C_3S mix and ultrasonicated for 30 minutes. The TiO_2 water was then filtered to 0.2 μm (MF75 series filter, Nalgene). Analysis of the filtrate by ICP-OES detected 36 mg/L of sulfur (peak wavelength of 180.669 nm). Another simple experiment was performed to examine if the sulfur present was the source of sulfate ions. The filtered TiO_2 water, same as the one used for the ICP-OES, was mixed with 10% wt. barium chloride solution. As soon as the barium chloride solution was poured to the TiO_2 water, the solution became foggy and white precipitate settled down with time, which is insoluble barium sulfate. This method is known for detection of sulfate ions, and this confirms that the sulfate ions are present

on the surface of TiO_2 particles. The presence of the sulfates is presumed to result from the extraction and purification of the TiO_2 and is presumed to be the source of the retardation observed in the 5% addition case.

While this delay in 5% TiO_2 paste hydration results in a lower cumulative heat evolution during the first few hours relative to the pure C_3S paste (Figure 4.5(a)), an equivalence with the ordinary paste is achieved by 10.1 hrs. In fact, all the pastes containing TiO_2 experience greater heat evolution than the control C_3S paste before the rate of energy evolution begins to slow. This is also true for the portland cement pastes containing TiO_2; all the pastes experienced greater heat evolution than the control cement paste (Figure 4.5(b)). However, it should be noted that the effect of addition of TiO_2 is greater in case of C_3S pastes, presumably due to high content C_3S and its relatively greater reactivity at early ages than other phases present in portland cement.

The degree of hydration, α, of a C_3S paste can be calculated by dividing the heat of hydration at a given time by the enthalpy of reaction of C_3S (ΔH=-121kJ/mol [78]). The values of α at 12 and 24 hrs for each paste are listed in Table 4.1. The increasing α with higher addition rates of TiO_2 further quantify the acceleratory effect of the nanoparticle addition. In particular, increases in 12-hr. α by 14, 35, and 46%, respectively, for 5, 10 and 15% TiO_2 when compared to the reference paste are notable. By 24 hrs, the acceleratory effect of the TiO_2 is less than at 12 hrs; increases in α at 24 hrs are 21, 27 and 31%, respectively, at 5, 10 and 15% TiO_2, when compared to the reference C_3S paste. These data suggest that the addition of TiO_2 nanoparticles to C_3S paste meaningfully affects early age hydration, potentially decreasing the time to set and increasing the rate of early strength development. Although the increases in the degree of

hydration of portland cement pastes are not as significant as C_3S pastes as can be seen from Figure 4.5, these data suggest that the setting time and early strength development can be tailored, if desired, using TiO_2 nanoparticles.

Table 4.1 — Cumulative heat of hydration and degree of hydration, α, of TiO_2-blended C_3S pastes at 12 and 24h.

TiO_2 added (%)	Cumulative heat (12h) (kJ/mol)	α (12h)	Cumulative heat (24h) (kJ/mol)	α (24h)
0	45.15	0.37	58.15	0.48
5	50.23	0.42	69.70	0.58
10	60.26	0.50	73.73	0.61
15	64.94	0.54	76.18	0.63

4.4.2 C_2S Calorimetry Data

The rates of heat evolution of the various C_2S pastes are shown in Figure 4.7 per gram of C_2S up to 90 days. Corresponding cumulative heat data is presented in Figure 4.8. The data were obtained every minute up to initial 5 hours, every hour up to 10 days, and every 24 hours after that until the end of experiment.

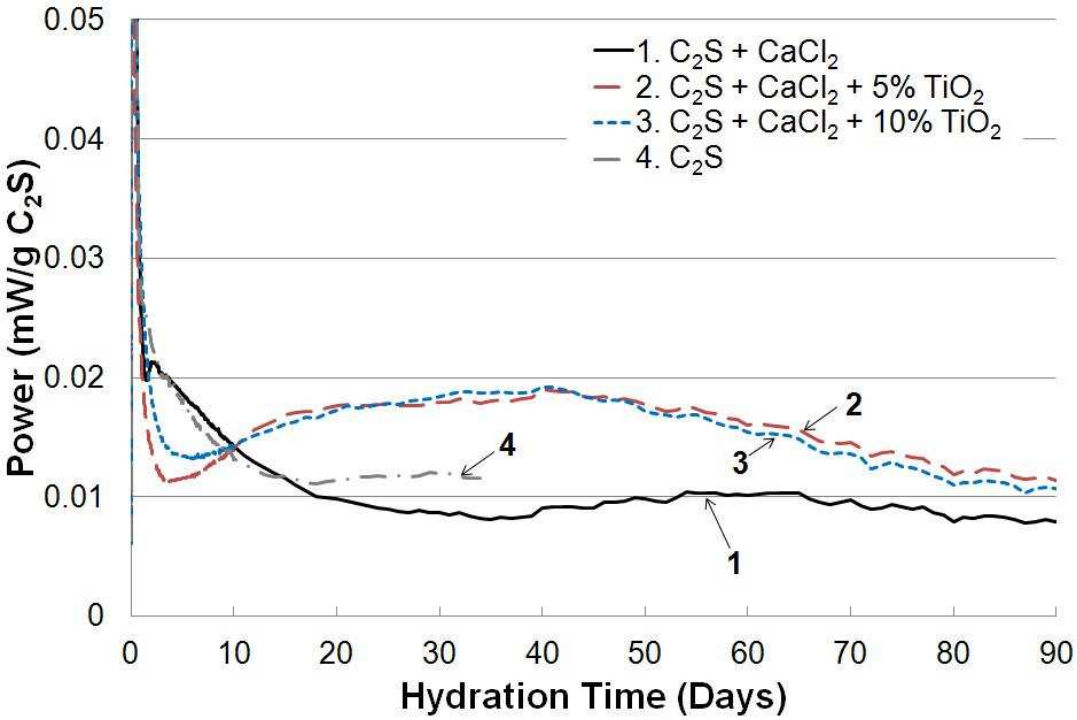

Figure 4.7 — Hydration rate of TiO_2-blended C_2S pastes

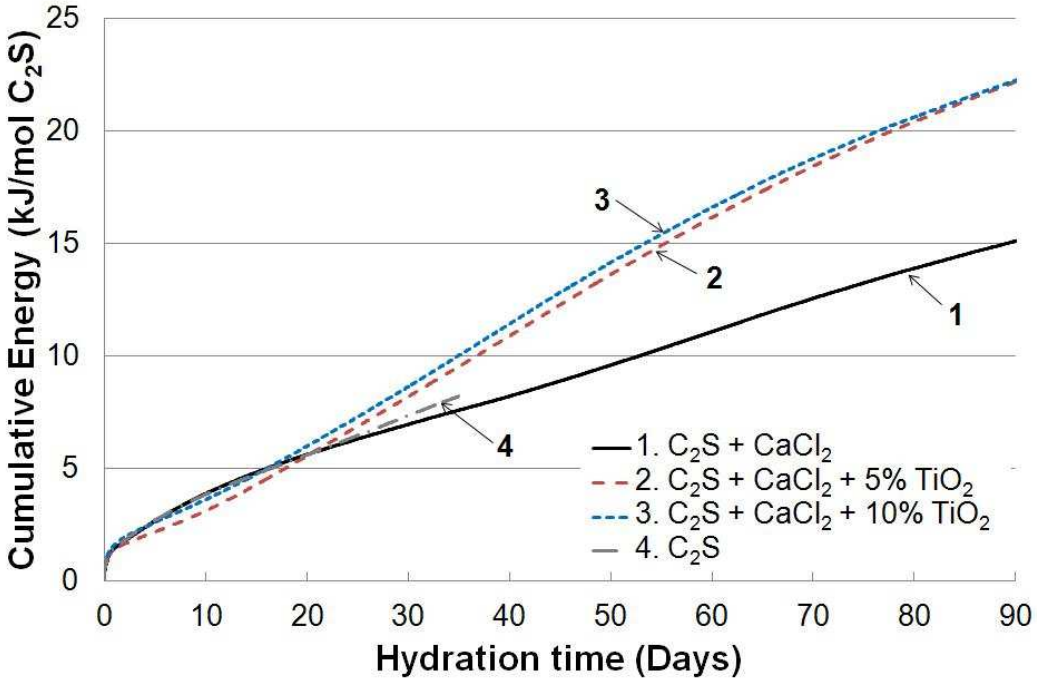

Figure 4.8 — Cumulative heat of hydration of TiO_2-blended C_2S pastes

Comparing the rate of hydration of the neat C_2S pastes with and without $CaCl_2$ in Figure 4.7, it seems that $CaCl_2$ resulted in retardation in the rate of C_2S hydration, rather than the desired acceleration. While for the pure C_2S paste, data is only available through 35 days, it does appear that an induction or latent period, visualized as the period surrounding a local minima in Figure 4.7, may be observed to occur at about 15-20 days. For the C_2S paste with $CaCl_2$, this occurs later, at about 30-40 days. Following the induction period, the rate peak occurs at about 30 days for pure C_2S paste and 60 days for C_2S paste with $CaCl_2$, showing 30 days of delay. This is contrary to the general findings [153-156] where researchers found that $CaCl_2$ accelerates the rate of β-C_2S hydration. However, Singh et al. [162] reported that $CaCl_2$ retards the highly reactive β-C_2S that is prepared at 900°C from decomposition of calcium silicate hydrate, possibly due to adsorption of calcium chloride on the surface of β-C_2S, making the surface less reactive. Palou et al. [163] have observed a retardation effect of $CaCl_2$ on calcium sulfoaluminate belite cement due to the increase of pH of pore solution. The effect of $CaCl_2$ on the rate of C_2S hydration needs to be further studied. Nonetheless, despite the regrettability of the $CaCl_2$ addition, the general trends in hydration rate with increasing nanoparticle addition can be examined by comparing among the pastes containing $CaCl_2$, where the titania dosage varied from 0%, 5%, and 10%.

While the neat C_2S paste with $CaCl_2$ shows long induction period and a subtle increase in the heat of hydration, both pastes containing TiO_2 nanoparticles clearly show induction periods occurring at ~3 days, followed by increasing rate of hydration reaching a rate peak (or local maxima) at about 40 days. These calorimetry data show that the hydration was accelerated about ~20 days with the addition of the inert TiO_2

nanoparticles. This acceleratory effect in the presence of the nanoparticles is in agreement with prior results by the authors [32], where the hydration of C_3S was accelerated with the addition of same type of TiO_2.

In addition, because the authors understand that the specific manufacturing process used could result in minor amounts sulfate ions (SO_4^-) being present on the TiO_2 nanoparticles, some simple experiments were performed to explore the possibility that those sulfates could affect the rate of belite reaction. To determine if the concentration of sulfate from the TiO_2 could be significant enough to affect hydration, the same TiO_2 powder was introduced to water at the same mass proportion as used in the 10% TiO_2 experiments in this manuscript. Using inductively coupled plasma optical emission spectrophotometry (ICP-OES), sulfur concentrations of ~36 ppm were measured at the 10% TiO_2 dosage rate. The amount of sulfate present, then, is extremely small. For example, during early cement hydration sulfate concentrations of ~350 mMol (or 2 orders of magnitude greater) would be expected [164].

However, the possibility of the formation of calcium sulfate precipitates through interaction of the sulfates with calcium ions deriving from belite or $CaCl_2$ was further explored. To assess this, a simple experiment was performed by mixing 20.0g $CaCl_2$ and 0.08g sodium sulfate (Na_2SO_4) in 500g of deionized water, using the same mass proportions as in 10% TiO_2-cement mix. The sample was filtered to 0.2μm and the residue dried and weighed. The mass of the dried residue was 0.05g, where 0.077g of calcium sulfate would be expected to precipitate upon full reaction with calcium. Thus, in the presence of $CaCl_2$, minor amounts (~0.1 g/L) of calcium sulfate may precipitate at the highest TiO_2 dosage rate examined.

Precipitation of any calcium sulfate might affect the surface area of particulates in the system, particularly if formed on the nanoparticle surface. There are two possibilities in this case: (1) increase in surface area by the formation of additional products on the nanoparticle surface (or elsewhere in the system), or (2) a net reduction in area by precipitates which block internal porosity. Specific surface areas of dried and ground titania particle slurries and companion slurries where $CaCl_2$ was introduced at the same rate as the experiments here were examined by nitrogen BET analysis (ASAP2020, Micromeritics, Norcross, GA). The results indicate that there was ~20% increase in the surface area, which provides support for case (1) above. This suggests that the addition of $CaCl_2$ to a system that contains this type of TiO_2, could further increase the surface area available for the nucleation of hydration products and thus could further accelerate the reaction. However, it should be noted that the grinding process, which was necessary for sample preparation, could have limited assessment of case (2); further, any more complex interactions between sulfates and hydrating cementitious phases were not measured in this case.

Interestingly, not much difference is observed in the C_2S hydration rate between pastes containing 5% and 10% of TiO_2. The author believes that this is the result of "diminishing returns" with increasing nanoparticle addition. That is, the rate of nuclei or hydration product formation is slow enough in the case of C_2S, that the added surface area of TiO_2 beyond the level of 5% does not have a noticeable effect on acceleration. Further, the authors believe that increasing nanoparticle agglomeration with increasing dosage rate – dispersion is a well-known challenge with the use of nanoparticles in cementitious systems [27, 32] – could reduce the effective surface area available for

nucleation with increasing dosage rate. The sulfate ions coming from TiO_2 can take part in more complex interactions particularly at higher dosage rates and could contribute to case (2) above, if precipitates form on the nanoparticles or agglomerates and "block" previously accessible surface area. However, given the low concentrations of the sulfates in these cases, it is not clear how significant this potential effect could be. Overall, the authors believe the greater dosage of TiO_2 produces "diminishing returns," as previously stated. Further work needs to be performed to examine the effect of different addition rates of TiO_2 to better understand these complex interactions.

Cumulative heat of hydration data in Figure 4.8 shows that degree of hydration of the pastes containing TiO_2 nanoparticles start to advance beyond those of the neat C_2S pastes at about 17-20 days. The degree of hydration, α, was calculated at 30, 60, and 90 days for all the pastes for comparison, by dividing the total heat of hydration at a given time by the enthalpy of reaction of C_2S (ΔH=45kJ/mol) [165]. The values are listed in Table 4.2. The result for the C_2S paste is relatively in agreement with Odler et al. [166], where the degree of hydration of pure β-C_2S at ~90 days was measured to be about 40% by quantitative X-ray diffraction analysis. At 90 days, a 47% increase in degree of hydration is measured for both 5% and 10% cases as compared to the neat C_2S paste with $CaCl_2$.

Table 4.2— Cumulative heat of hydration and degree of hydration, α, of TiO_2-blended C_2S pastes at 30, 60, and 90 days

TiO_2 added (%)	30 days		60 days		90 days	
	Cumulative heat (kJ/mol)	α	Cumulative heat (kJ/mol)	α	Cumulative heat (kJ/mol)	α
0	6.94	0.15	11.06	0.25	15.09	0.34
5	8.18	0.18	16.14	0.36	22.17	0.49
10	8.62	0.19	16.59	0.37	22.24	0.49

However, generally when interpreting the calorimetry data in both Figures 4.7 and 4.8, the results should be treated qualitatively to see a trend rather than examining the exact values, especially at later ages. Due to the inherent limitation of isothermal calorimetry, it is difficult to capture slowly released heat such as C_2S hydration. Heat can be absorbed to the equipment or dissipated before it can reach a sensor, eventually recording lower rate of heat evolution. Also, it is known that specific heat of hydrating cement paste decrease as a function of degree of hydration [159, 167]. This yields higher heat capacity in reference ampoule than sample ampoule, which in turn decreases sensitivity of the system.

Overall, these data do suggest that the addition of TiO_2 nanoparticles to C_2S paste notably accelerate the early hydration reaction rate, possibly by providing more nucleation sites, due to their smaller particle size. This finding is relevant to setting time and early strength development of C_2S-rich cement which has potential for further optimizing the performance of lower-CO_2 and lower-energy cement compositions containing belite.

4.4.3 C_3S Model Fits

It should be recalled that the TiO_2 particles added to these pastes are not known to react with water or calcium silicates. Therefore, an alternative explanation for the observed increase in early age C_3S reaction in the presence of these nanoparticles must be sought. Here, hydration behavior of the C_3S pastes examined are compared to existing models to provide additional insight into the mechanism by which TiO_2 nanoparticles influence early age reaction rate.

Visual representations of the hydration of different TiO_2 pastes at 12 hrs are presented in Figure 4.9. These include depictions of the initial C_3S and TiO_2 solids, as well as capillary porosity at 0 hrs hydration, which are based upon the initial volumetric proportions in the pastes examined. In addition, Figure 4.9 depicts the formation of hydration products (and corresponding decreases in C_3S and porosity) at 12 hrs, where these early hydration products are shown to form on the C_3S surface as well as on the TiO_2 surface, in accordance with the BN theory. The area fractions of each component were calculated based on Powers model [168] using the temporal degrees of hydration obtained from the experimental data, which are listed in Table 4.3. Based on the simple stereological principles, area fractions obtained for a 2D cross-section are equal to volume fractions for the 3D real structure when materials have a completely random and isotropic nature [169]. It can be seen from Figure 4.9 and Table 4.3 that the increasing TiO_2 content promotes higher degree of hydration at a given time. The decrease in relative capillary porosity and more spatially uniform distribution of hydration products with higher TiO_2 dosage at 12 hrs might lead to higher early strength and lower permeability.

Table 4.3 — Area fractions of C_3S, TiO_2, hydration products, and porosity at 0 and 12 hrs.

TiO_2 content (% mass)	0 hr				12 hrs			
	0	5	10	15	0	5	10	15
C_3S (%)	38.39	37.79	37.21	36.65	24.18	21.92	18.61	16.86
TiO_2 (%)	0	1.56	3.06	4.52	0	1.56	3.06	4.52
Hydration products (%)	0	0	0	0	28.41	31.74	37.21	39.58
Porosity (%)	61.61	60.65	59.73	58.82	47.41	44.78	41.12	39.03

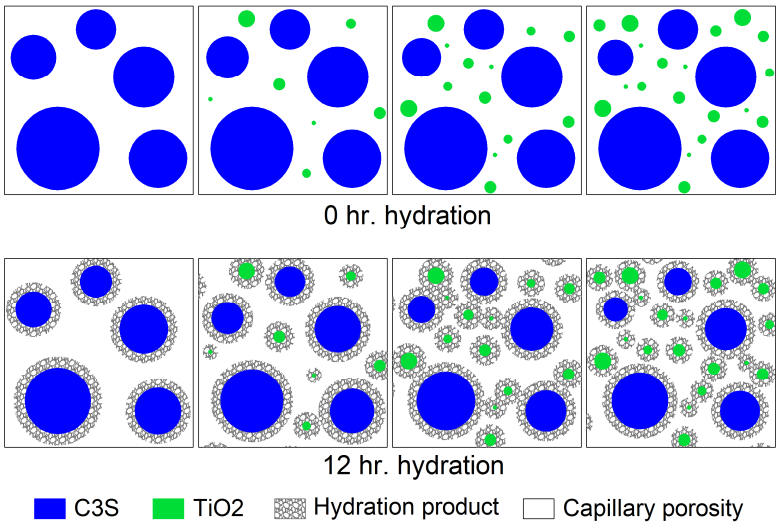

Figure 4.9 — 0%, 5%, 10%, and 15% TiO_2 at 0, 12 hrs hydration; α=37, 42, 50, and 54% respectively

Both the Avrami model and the BN model were applied to the experimental data for each of the four sample types (see Figures 4.10 (a), (b), (c), and (d)). Fitting was performed manually to obtain the closest fit around the rate peak. The O_v^B values for the BN model for each of the mix were calculated from the surface area of the C_3S and TiO_2 powder (Table 4.5), by dividing the total surface area per gram of mixed powder by the volume occupied by the hydration products after complete hydration. Although the

nucleation rate or hydration product growth rate on C_3S or TiO_2 surface would likely to be different, it is assumed here that the surface characteristics of C_3S and TiO_2 to be the same due to absence of data describing those variations and for simplicity in this initial investigation. The hydration volume of C_3S is 0.662 cm^3/g C_3S [92] and the volume of TiO_2 was incorporated based on density of $4.23g/cm^3$, considering it is chemically non-reactive. The increase in O_v^B with higher TiO_2 dosage in the BN model is expected and indicates increasing surface area for potential C-S-H nucleation. The fit parameters are listed in Table 4.4 for the Avrami model, and in Table 4.5 for the BN model.

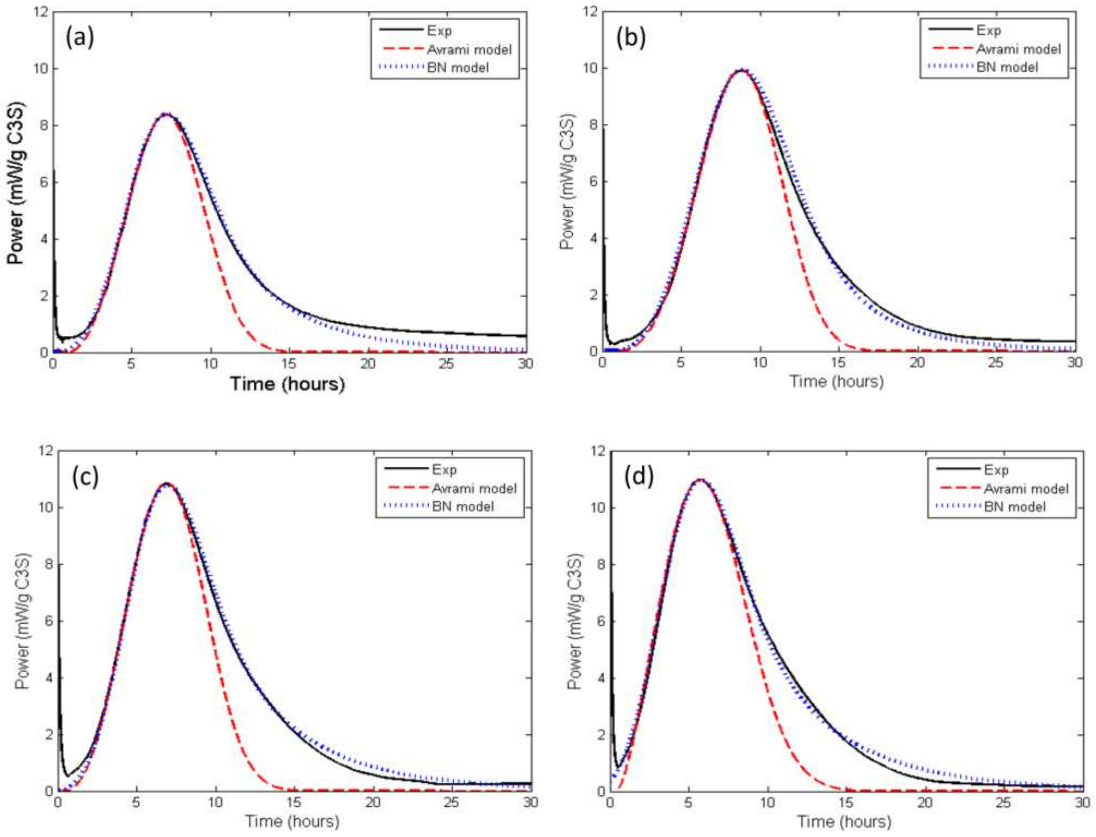

Figure 4.10 — Rate of hydration: Experiment vs. Avrami and BN models

(a) 0% TiO_2, (b) 5% TiO_2, (c) 10% TiO_2, and (d) 15% TiO_2

Table 4.4 — Fit parameters **Ȧ**, t_0, k_{avr}, and n for Avrami model

TiO_2 (%)	Ȧ (kJ/mol)	t_0 (h)	k_{avr} (h^{-1})	n
0	49	1.3	0.141	3.1
5	65	1.2	0.113	3.5
10	67	1.0	0.138	3.0
15	71	0.9	0.153	2.5

Table 4.5 — Fit parameters O_v^B, **Ȧ**, t_0, G, I_B, k_B, k_G, and k_B/k_G for boundary nucleation model

TiO_2 (%)	O_v^B (μm^{-1})	Ȧ (kJ/mol)	t_0 (h)	G (μm/h)	I_B $(\mu m^{-2}h)^{-1}$	k_B (h^{-1})	k_G (h^{-1})	k_B/k_G
0	2.40	69	-0.25	0.0379	1.47	0.118	0.091	1.295
5	50.00	85	0.17	0.0021	239.62	0.103	0.105	0.977
10	91.51	93	-0.50	0.0009	2887.37	0.117	0.082	1.433
15	133.80	96	-1.67	0.0006	6732.14	0.117	0.079	1.477

Both of the models give good fits to the experimental hydration rate data in the acceleration period for all of the pastes. However, the BN model clearly provides a closer approximation than the Avrami model in the deceleration period for all of the pastes. This was previously shown for C_3S hydration under different conditions by Thomas [92]. The divergence with the Avrami model in the deceleration period suggests that the conditions of random nucleation assumed by that model do not apply to hydration of these systems. This indicates that nucleation is spatially nonrandom and is likely related to the surface area of the solid phases available for product nucleation and growth.

The t_0 parameter in both the Avrami model and the BN model graphically shifts the curves either to the right or to the left, depending on the sign. A positive t_0 value can be interpreted as an induction period, shifting the curve to the right. On the other hand, a negative t_0 value found in the BN model fits shifts the curve to the left, which suggests that the TiO_2 particles have an effect of promoting the reaction rate at a very early age. The 0.42 hrs delay in t_0 value for the 5% TiO_2 case compared to the 0% case suggests that there has been retardation. In contrast, the t_0 values of 10 and 15% TiO_2 cases were accelerated by 0.25 and 1.42 hrs respectively, indicating that the greater surface area provided by additional TiO_2 overcomes the retardation effect. These observations are comparable to the time of rate peaks, which resulted in 1.60 hrs of retardation and 0.31 and 1.51 hrs of acceleration at 5, 10, and 15% TiO_2 cases respectively, in regard to the 0% case. However, the t_0 parameters of the Avrami model do not seem to relate to the rate of hydration. Specifically, the decreasing t_0 with increasing TiO_2 dosage does not capture the retardation observed in the 5% case. Thus, it can be concluded that the better indicators of acceleration or retardation of rate of early hydration are found in the t_0 parameters of BN model.

From the resulting parameters of the BN model (Table 4.5), some interesting observations can be made. As more TiO_2 is added, the decrease in linear growth rate, G, was observed. In conjunction with the increasing degree of hydration, this suggests that the hydrated product in fact is growing on a larger surface area, such as on C_3S and on added TiO_2 particles (as suggested in Figure 4.9). The increasing I_B with increasing O_v^B suggests that more nucleates are formed in pastes with greater TiO_2 addition, indicating that added surface area of TiO_2 acts as nucleation sites. It should be noted here that due to

the assumption made on the O_v^B parameter and G, the data should be treated qualitatively to see a trend rather than examining the exact values. Further, an increase in the k_B/k_G of the BN model is found at 10 and 15% TiO_2 dosage with regard to 0% paste. This suggests that the presence of sufficient additional surface area provided by the increasing amounts of TiO_2 promotes hydration product formation, which occurs on or near the surfaces of the particles according to the model assumptions. The decrease in the k_B/k_G of the 5% TiO_2 case can again be explained by the retardation effect, that the formation of hydration products are slowed, likely by the presence of calcium sulfate salts on the surface of C_3S and/or TiO_2 particles. It is also proposed that by providing additional nucleation sites away from the reacting C_3S particles, the start of diffusion-controlled hydration kinetics is delayed, increasing the amount of early nucleation and growth hydration, as has been proposed for other nucleating materials [78]. Such behavior would account for both the acceleration in reaction rate and the increase in peak height observed in the presence of TiO_2 nanoparticles.

4.5 Conclusions

The early hydration behavior of C_3S and C_2S pastes containing up to 15% and up to 10% additions of high surface area TiO_2 respectively, was investigated. Two nucleation and growth models – the Avrami model and the boundary nucleation model – were applied to the experimental C_3S calorimetry data. Based on the results of this study, the following conclusions are drawn:

- The addition of high surface area TiO_2 powder provided additional nucleation sites for hydration product formation, resulting in acceleration in the hydration reaction; higher rate peaks and higher total heat of hydration was observed in both C_3S pastes and portland cement pastes.
- For the C_3S pastes, a delay in the rate of hydration was found in 5% TiO_2 pastes. Preliminary experimental results suggest that the retardation in this case results from surface residues present on the TiO_2 nanoparticles and are likely an artifact of the pure C_3S system. Further experiments, however, are necessary to determine if such effects may be observed in portland cements of varying composition.
- The calorimetry results show that the hydration rates of C_2S pastes containing TiO_2 nanoparticles were accelerated compared to neat C_2S pastes. The degree of hydration of TiO_2 containing C_2S pastes was observed to be greater than neat C_2S paste by 20 days, and was measured to be ~50% greater by 90 days. The results suggest that the use of nanoparticles can increase the rate of C_2S hydration.
- The BN model is capable of representing the kinetic behavior of C_3S paste mixed with TiO_2 nanoparticles and provides a better fit to the rate data than the Avrami model for all pastes tested.
- The increase in the ratio of the rate constants from the BN model (k_B/k_G) with higher percentages of TiO_2 suggests that the formation of hydration products is linked to the increase in available nucleation sites (i.e., increase in solid surface area) provided by the TiO_2 nanoparticles. The decreasing linear growth rate (G) and increasing nucleation rate (I_B) also suggest that hydration products are formed on greater surface areas, which support the BN model.

Observations such as these which show that the rate of hydration can be altered through the addition of chemically non-reactive TiO_2 particles suggest that the setting behavior, strength development, and permeability of photocatalytic and other portland cements can be optimized by controlling compositional variables and particle size. This could also potentially promote the practical use of higher-C_2S cements, contributing to sustainability.

4.6 References

8. Carp, O., C.L. Huisman, and A. Reller, *Photoinduced reactivity of titanium dioxide.* Progress in Solid State Chemistry, 2004. **32**(1-2): p. 33-177.

14. Poon, C.S. and E. Cheung, *NO removal efficiency of photocatalytic paving blocks prepared with recycled materials.* Construction and Building Materials, 2007. **21**(8): p. 1746-1753.

16. Beeldens, A. *Air purification by road materials: Results of the test project in Antwerp*. in *International RILEM Symposium on Photocatalysis, Environment, and Construction Materials*, 2007. Florence, Italy.

18. Fujishima, A. and X.T. Zhang, *Titanium dioxide photocatalysis: present situation and future approaches.* Comptes Rendus Chimie, 2006. **9**(5-6): p. 750-760.

26. Hui, L., H.G. Xiao, and J.P. Ou, *A study on mechanical and pressure-sensitive properties of cement mortar with nanophase materials.* Cement and Concrete Research, 2004. **34**(3): p. 435-438.

27. Jo, B.W., et al., *Characteristics of cement mortar with nano-SiO_2 particles.* Construction and Building Materials, 2007. **21**(6): p. 1351-1355.

32. Lee, B.Y. and K.E. Kurtis, *Influence of TiO_2 Nanoparticles on Early C_3S Hydration.* Journal of the American Ceramic Society, 2010. **93**(10): p. 3399-3405.

34. Campillo, I., et al., *Improvement of initial mechanical strength by nanoalumina in belite cements.* Materials Letters, 2007. **61**(8-9): p. 1889-1892.

50. Jayapalan, A.R., B.Y. Lee, and K.E. Kurtis. *Effect of nano-sized titanium dioxide on early age hydration of portland cement*. in *Nanotechnology in Construction 3*, 2009. Prague, Czech Republic.

78. Thomas, J.J., H.M. Jennings, and J.J. Chen, *Influence of nucleation seeding on the hydration mechanisms of tricalcium silicate and cement.* Journal of Physical Chemistry C, 2009. **113**(11): p. 4327-4334.

79. Bishnoi, S. and K.L. Scrivener, *Studying nucleation and growth kinetics of alite hydration using μic.* Cement and Concrete Research, 2009. **39**(10): p. 849-860.

80. Damasceni, A., et al., *A novel approach based on differential scanning calorimetry applied to the study of tricalcium silicate hydration kinetics.* Journal of Physical Chemistry B, 2002. **106**(44): p. 11572-11578.

81. Avrami, M., *Kinetics of phase change I - General theory.* Journal of Chemical Physics, 1939. **7**(12): p. 1103-1112.

82. Avrami, M., *Kinetics of phase change 2 - Transformation-time relations for random distribution of nuclei.* Journal of Chemical Physics, 1940. **8**: p. 212-24.

83. Avrami, M., *Granulation, phase change, and microstructure - Kinetics of phase change. III.* Journal of Chemical Physics, 1941. **9**(2): p. 177-184.

84. Fanfoni, M. and M. Tomellini, *The Johnson-Mehl-Avrami-Kolmogorov model: A brief review.* Il Nuovo Cimento. D, 1998. **20**: p. 1171-1182.

85. Cahn, J.W., *The kinetics of grain boundary nucleated reactions.* Acta Metallurgica, 1956. **4**(5): p. 449-459.

86. Brown, P.W., J. Pommersheim, and G. Frohnsdorff, *A kinetic-model for the hydration of tricalcium silicate.* Cement and Concrete Research, 1985. **15**(1): p. 35-41.

87. FitzGerald, S.A., et al., *In situ quasi-elastic neutron scattering study of the hydration of tricalcium silicate.* Chemistry of Materials, 1998. **10**(1): p. 397-402.

88. Thomas, J.J. and H.M. Jennings, *Effects of D_2O and mixing on the early hydration kinetics of tricalcium silicate.* Chemistry of Materials, 1999. **11**(7): p. 1907-1914.

89. Ridi, F., et al., *Hydration process of cement in the presence of a cellulosic additive. A calorimetric investigation.* Journal of Physical Chemistry B, 2005. **109**(30): p. 14727-14734.

90. Kolmogorov, A.N., *A statistical theory for the recrystallization of metals.* Bulletin of the Academy of Sciences of the USSR: physics series, 1937. **1**: p. 355-359.

91. Johnson, W.A. and R.F. Mehl, *Reaction kinetics in processes of nucleation and growth.* Transactions of the American Institute of Mining and Metallurgical Engineers 1939. **135**: p. 416-442.

92. Thomas, J.J., *A new approach to modeling the nucleation and growth kinetics of tricalcium silicate hydration.* Journal of the American Ceramic Society, 2007. **90**(10): p. 3282-3288.

93. Garrault, S., T. Behr, and A. Nonat, *Formation of the C-S-H layer during early hydration of tricalcium silicate grains with different sizes.* Journal of Physical Chemistry B, 2006. **110**(1): p. 270-275.

94. Gauffinet, S., et al., *Direct observation of the growth of calcium silicate hydrate on alite and silica surfaces by atomic force microscopy.* Comptes Rendus De L Academie Des Sciences Serie Ii Fascicule a-Sciences De La Terre Et Des Planetes, 1998. **327**(4): p. 231-236.

95. Makar, J.M. and G.W. Chan, *Growth of cement hydration products on single-walled carbon nanotubes.* Journal of the American Ceramic Society, 2009. **92**(6): p. 1303-1310.

96. Brown, P.W., *Effects of particle-size distribution on the kinetics of hydration of tricalcium silicate.* Journal of the American Ceramic Society, 1989. **72**(10): p. 1829-1832.

97. Bentz, D.P., et al., *Effects of cement particle size distribution on performance properties of portland cement-based materials.* Cement and Concrete Research, 1999. **29**(10): p. 1663-1671.

136. Chernet, T., *Effect of mineralogy and texture in the TiO_2 pigment production process of the Tellnes ilmenite concentrate.* Mineralogy and Petrology, 1999. **67**: p. 21-32.

146. Berliner, R., et al., *Quasielastic neutron scattering study of the effect of water-to-cement ratio on the hydration kinetics of tricalcium silicate.* Cement and Concrete Research, 1998. **28**(2): p. 231-243.

147. Tarrida, M., et al., *An in-situ raman-spectroscopy study of the hydration of tricalcium silicate.* Advanced Cement Based Materials, 1995. **2**(1): p. 15-20.

148. Fujii, K. and W. Kondo, *Kinetics of hydration of tricalcium silicate.* Journal of the American Ceramic Society, 1974. **57**(11): p. 492-497.

149. Kawakami, M., T. Furumura, and H. Tokushige, *NO_x removal effects and physical properties of cement mortar incorporating titanium dioxide powder.* Proc. International RILEM Symposium on Photocatalysis, Environment, and Construction Materials, 2007: p. 163-170.

150. Hendriks, C.A., et al. *Emission reduction of greenhouse gases from the cement industry*. in *Proceedings of the 4th International Conference on Greenhouse Gas Control Technologies*, 1998. Interlaken, Austria.

151. Gartner, E., *Industrially interesting approaches to "low-CO_2" cements.* Cement and Concrete Research, 2004. **34**(9): p. 1489-1498.

152. Li, G.Y., *Properties of high-volume fly ash concrete incorporating nano-SiO_2.* Cement and Concrete Research, 2004. **34**(6): p. 1043-1049.

153. Odler, I. and J. Skalny, *Pore structure of hydrated calcium silicates 2. Influence of calcium chloride on pore structure of beta-dicalcium silicate* Journal of Colloid and Interface Science, 1971. **36**(3): p. 293-297.

154. El-Didamony, H., et al., *Hydration characteristics of beta-C_2S in the presence of some accelerators.* Cement and Concrete Research, 1996. **26**(8): p. 1179-1187.

155. *Concrete admixtures handbook: properties, science, and technology*. 2nd ed. Building materials science series, ed. V.S. Ramachandran. 1995, Park Ridge, N.J., U.S.A. :: Noyes Publications.

156. *Handbook of thermal analysis of construction materials*. Construction materials science and technology series, ed. V.S. Ramachandran. 2003, Norwich, N.Y. :: Noyes Publications/William Andrew Pub.

157. Gosselin, C., E. Gallucci, and K. Scrivener, *Influence of self heating and Li_2SO_4 addition on the microstructural development of calcium aluminate cement.* Cement and Concrete Research, 2010. **40**(10): p. 1555-1570.

158. Riding, K., D.A. Silva, and K. Scrivener, *Early age strength enhancement of blended cement systems by $CaCl_2$ and diethanol-isopropanolamine.* Cement and Concrete Research, 2010. **40**(6): p. 935-946.

159. Bentz, D.P., *Transient plane source measurements of the thermal properties of hydrating cement pastes.* Materials and Structures, 2007. **40**(10): p. 1073-1080.

160. Todd, S.S., *Low-temperature heat capacities and entropies at 298.16 degrees K of crystalline calcium orthosilicate, zinc orthosilicate and tricalcium silicate.* Journal of the American Chemical Society, 1951. **73**(7): p. 3277-3278.

161. Taylor, H.F.W., *Cement chemistry*. 2nd ed. ed. 1997, London: Thomas Telford.

162. Singh, N.B., S. Rai, and N. Singh, *Highly reactive beta-dicalcium silicate.* Journal of the American Ceramic Society, 2002. **85**(9): p. 2171-2176.

163. Palou, M.T. and J. Majling, *Effects of sulphate, calcium and aluminum ions upon the hydration of sulphoaluminate belite cement.* Journal of Thermal Analysis, 1996. **46**(2): p. 549-556.

164. Gartner, E.M., et al., *Structure and Performance of Cements*. 2nd ed, ed. J. Bensted and P. Barnes. 2002, London: Spon Press.

165. *Lea's chemistry of cement and concrete*. 4th ed, ed. P.C. Hewlett. London: Arnold.

166. Odler, I. and J. Schüppstuhl, *Combined hydration of tricalcium silicate and β-dicalcium silicate.* Cement and Concrete Research, 1982. **12**(1): p. 13-20.

167. Deschutter, G. and L. Taerwe, *Specific-heat and thermal-diffusivity of hardening concrete.* Magazine of Concrete Research, 1995. **47**(172): p. 203-208.

168. Powers, T.C. *Physical properties of cement paste*. in *4th International symposium on the chemistry of cement*, 1960. Washington.

169. Russ, J.C. and R.T. Dehoff, *Practical Stereology*. 2nd ed. 2000, New York, USA: Kluwer Academic Press.

CHAPTER 5

PHOTOCATALYTIC CEMENT EXPOSED TO NITROGEN OXIDES: EFFECT OF OXIDATION AND BINDING

5.1 Introduction

In this chapter, the effect of TiO_2-cement on oxidation and binding of nitric oxide (NO) and nitrogen dioxide (NO_2) gases is examined. To assess photocatalytic efficiency, standards such as ISO standard [99] and JIS standard [98] have been established for advanced ceramics, where photocatalyst is added by coating, impregnation, and mixing. However, both of these standards utilize only NO gas in their experimental procedures. As a result, significantly more effort has been put toward measurements of NO gas oxidation than NO_2 gas oxidation by photocatalytic materials. Yet, NO_2 gas is a major air pollutant that threatens human health and also participates in the formation of photochemical smog and ozone (O_3) [5], ultimately contributing to global warming. Once the NO gas is emitted primarily from the combustion source, the part of NO gas is converted into NO_2 gas, and they coexist in equilibrium in the atmosphere through reactions described in Equation (1.1). The NO/NO_2 ratio is thus determined by the intensity of solar radiation and the concentration of ozone. It was reported, that the annual average on-road NO_2/NOx ratio was 28% [170], meaning that the harmful NO_2 gas is as much as 39% of the NO gas. Taking into consideration the severity of the NO_2 gas and its quantity fraction, there is a need to investigate the photocatalytic behavior of cementitious materials under NO_2 as well as NO exposure.

In addition to the relative dearth of information regarding the photocatalytic efficiency of cementitious materials under NO_2 exposure, some preliminary work has suggested that NO_2 can be bound into cementitious materials without the benefit of photocatalysis. Vallee et al. [45] performed de-polluting experiments exposing photocatalytic surfaces to NO_2 gas, and mentioned the possibility that NO_2 can be adsorbed into cementitious materials in the absence of UV-radiation that is later oxidized in the day time. Yoshio et al. [171] also tested TiO_2 coated cement on NOx removal, and mentioned that NO_2 gas can be adsorbed on the porous surface structure of cement. The potential of cementitious materials to decrease the amount of the NO_2 in the atmosphere is important, then, for a comprehensive assessment of the potential environmental impact of cement-based infrastructure. For example, NOx binding in the cementitious structure in the absence of photocatalysis (i.e., in the absence of UV-radiation) could potentially facilitate subsequent photocatalytic reaction by providing nitrogen oxides near the TiO_2 particles. Although researchers report that the NO_2 gas can possibly be adsorbed in cement-based materials [45, 171], relatively minimal effort has been made to quantify NOx binding capacity of the variations in these materials in the published literature. Thus, a detailed examination of NOx binding – including examination of NO and NO_2 binding – in cementitious system is warranted.

The objectives of this research are to examine and compare the photocatalytic efficiency and NOx binding capacity of TiO_2-containing cement-based materials under both NO and NO_2 gas. The effect of different water-to-cement ratios (w/c) of the cementitious materials on the photocatalytic efficiency is also studied.

5.2 Materials and Experimental Procedure

Hardened cement pastes at varying w/c and containing varying amounts of photocatalytic TiO_2 nanoparticles were prepared. Tests were performed to assess photocatalytic binding of NO and NO_2, with UV-radiation (i.e., "photocatalysis series"). Additional tests were performed to examine the potential for NO and NO_2 binding in the absence of UV-radiation (i.e., "NOx binding series").

5.2.1 Materials

The cement used was ASTM C 150 Type I portland cement with potential Bogue composition of 54% C_3S, 18% C_2S, 7% C_3A, and 10% C_4AF. (The cement chemistry notations of these oxides are defined as C=CaO, S=SiO_2, F=Fe_2O_3, and A=Al_2O_3.) The TiO_2 used was selected as one more commonly used in the concrete industry (Aeroxide TiO_2 P25, Evonik Industries), which consisted of 80% anatase and 20% rutile titania. The average crystal size is 21nm, the surface area is 50±15 m^2/g, and the sample purity is 99.5%, as stated by the manufacturer. NO and NO_2 gas were obtained at 100 ppm each and were mixed with ultra pure zero air (~80% nitrogen and ~20% oxygen) to reach the desired concentration.

5.2.2 Sample Preparation

Two series of cement paste samples were prepared. For the photocatalysis series, pastes were prepared at water-to-cement ratios (w/c) of 0.40, 0.50, and 0.60, all with 5% TiO_2 replacement by mass of cement. For the NOx-binding series, samples were prepared

with a consistent composition at w/c of 0.60 with 10% TiO_2 replacement by mass of cement.

To prepare the samples, the TiO_2 particles were mixed with deionized water for 1 minute using a hand-held mixer at a low speed. Cement was then added to the TiO_2 slurry and mixed for 1 additional minute at a low speed and another 1 minute at a medium speed. Samples were cast in plastic molds with dimension of 4.8cm x 4.8cm x 0.8cm. They were allowed to cure in a 100% relative humidity and at 23±2°C for the initial 24 hours, and continued to be cured in lime water after demolding at 23±2°C. For the photocatalysis series, samples were taken out from the lime water at 47 days of age, progressively polished to 15 microns using 600 grit wet sandpaper, and conditioned in a 30°C oven until the mass change was less than 0.5% within 24 hours. For the NOx binding series, samples were prepared and cured in the same manner, except they were cured for 28 days of age and polished up to 5μm, and dried for 3 days. They were exposed to multiple cycles of wetting, drying, and NOx exposure under UV light to simulate field weathering conditions (as part of another series of experiments, presented in Chapter 6). In order to investigate the influence of moisture state on binding and to better understand the binding mechanisms, samples were conditioned to be either either ‘wet’ or ‘dry’ during NO or NO_2 exposure. Wet samples were fully immersed in deionized water for 3 hours under vacuum, and kept wet in plastic bags until tested. Saturation was confirmed by breaking a control sample and visually examining the broken surface. Dry samples were conditioned in 40ºC oven until mass change less than 0.1% within 24 hours.

5.2.3 Methodology

Both of series utilized a UV reactor that was designed to largely conform to the ISO and JIS standards [98, 99] for measurements of removal of nitric oxide during photocatalysis. The inner width of the reactor was manufactured to be 8cm compare to 5cm in the standards to accommodate for larger samples. Also, for simplicity, height adjusting plate was not utilized, meaning that test gas could not only pass above the sample surfaces but also through the sides. Figure 5.1 shows the picture of the UV reactor with the UV light on, and Figure 5.2 is a schematic of the entire test set-up. The test set-up was designed to maintain a constant concentration of test gas flow into the reactor, and which then flows over the sample surfaces (which may be illuminated with UV light), and exits on the other side of the chamber where gas concentration is measured with time. Samples were placed in the reactor with only one face exposed to the UV light and the test gas. Two 40W UV fluorescent lamps (GE) with peak emission at 368nm were used to produce the UV light. The power density of the UV light at the sample surface was maintained at 10W m^{-2} by adjusting the distance between the light source and sample plane.

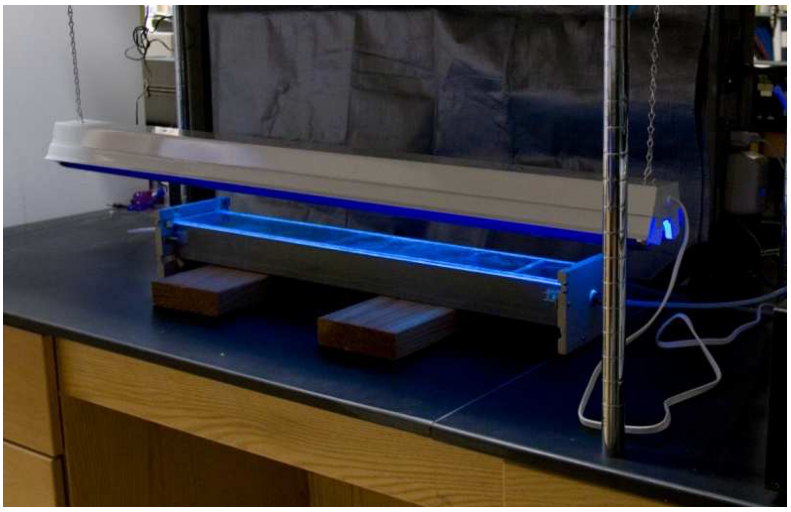

Figure 5.1—NOx reactor with UV light on

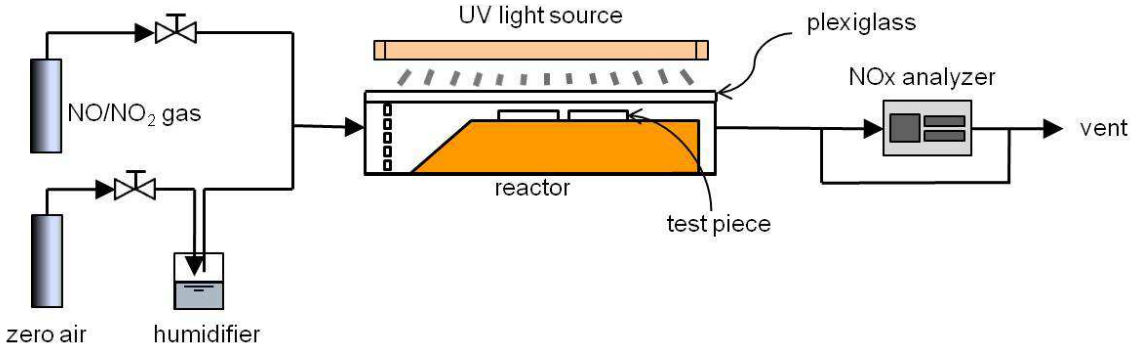

Figure 5.2—Experimental set-up showing NO/NO_2 flow and UV reactor

5.2.3.1 Photocatalysis Series with NO and NO_2 gases

For the photocatalysis series, experimental conditions were kept constant among tests with only the type of test gas (either NO or NO_2) varying. The test gas concentration was adjusted to a targeted value of 1000ppb in the reactor with 5 cement samples already installed, which is equivalent to $115cm^2$ effective surface areas. Note that the starting concentration was measured at the outlet of the experimental chamber just before the UV light is turned on, which can be lower than the actual input concentration due to gas

adsorption on experimental setup and test samples. The gas flow rate was fixed at 500ml/min. Once the gas concentration was stabilized, the UV light exposure was begun and continued for 3 hours. After the UV light was turned off, the gas was allowed to stabilize again with measurements continuing during this period. Further, additional measurements of gas concentration were after the samples were removed to confirm the air tightness and passivity of the chamber itself. Photocatalytic reactivity was determined by the percentage drop in gas concentration compared to the initial concentration (~1000ppb) using the total sample surface area exposed to the UV light, which is ~115cm^2. This is a simplified method which does not account for flow rate or sample surface area, since all of these parameters were kept constant.

5.2.3.2 NO and NO_2 Binding Series

To investigate the binding capabilities of the cementitious materials in the absence of photocatalysis, a continuous concentration of test gas was maintained using the same reactor used for the NOx oxidation series. However, in this series, the UV light was not utilized. This way the binding can be examined apart from the effect of photocatalytic NOx oxidation. The input NO and NO_2 concentration was controlled to be consistent at ~1000ppb at flow rate of 500ml/min before samples were inserted. Once the gas was stabilized, the reactor was opened and five of either wet or dry samples were inserted in less than 5 minutes and were maintained in the reactor for 5 hours. Then, the samples were removed and the gas concentration in the reactor was again stabilized before terminating the experiment. The gas concentration was measured with and without samples throughout the experiment, again to validate the passivity of the reactor itself.

As previously describes, samples were prepared either in dry condition or wet condition to examine the mechanism of the NOx binding in cementitious materials. That is, this variation in moisture state will allow assessment of whether the test gas is adsorbed on hardened cement paste solids directly or may be first absorbed into the cement pore solution. The test set-up was modified from the first series by removing a humidifier so that no moisture inflow was allowed. The rate of gas binding can be determined by the changes in the level of gas stabilization in the reactor before and after the samples are inserted.

5.3 Results and Discussion

5.3.1 Photocatalysis Series under NO and NO_2

The influence of water-to-cement ratio on photocatalytic efficiency in the presence of NO and NO_2 gas was examined. Because it is well-known that varying the w/c of the material alters the pore structure (i.e, pore volume, size distribution, interconnectivity) of cementitious materials [172], the amount of effective surface area available for photocatalytic oxidation may also be affected [21, 22].

Figures 5.3 and 5.4 show the influence of water-to-cement ratio during photocatalysis of cement pastes exposed to NO and NO_2 gas, respectively. Photocatalytic efficiency at 1 hour intervals up to 3 hours after UV irradiation were calculated and presented in Table 5.1. The 3 hour duration of the test was determined from observation of the changes in NO and NO_2 concentration over time. For the size of cement paste samples examined, a relative stasis in gas concentration at ~700 ppb was achieved during a 3-hour exposure period.

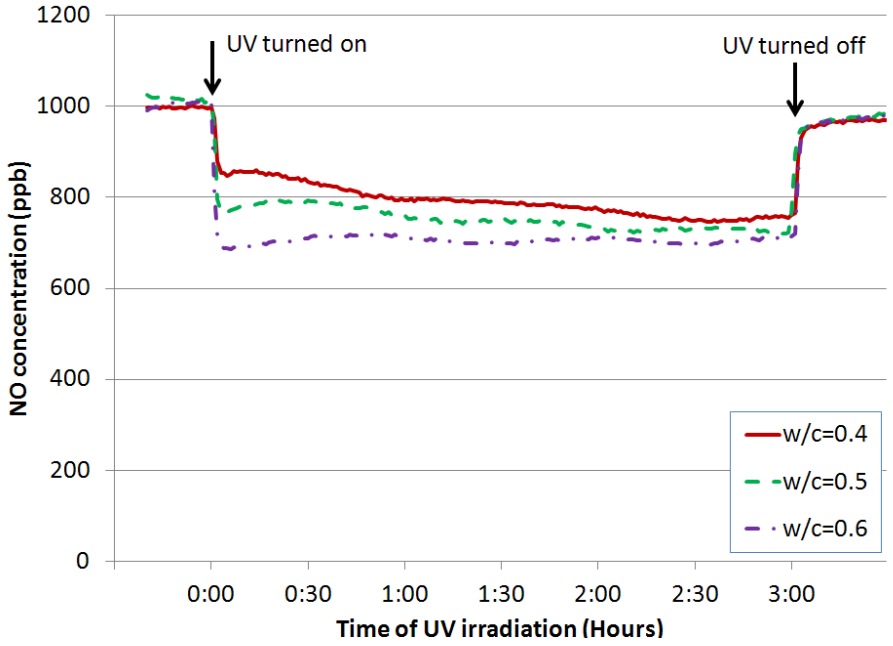

Figure 5.3—NO test data with samples with w/c=0.40, 0.50, and 0.60, each with 5% TiO_2 by mass of cement

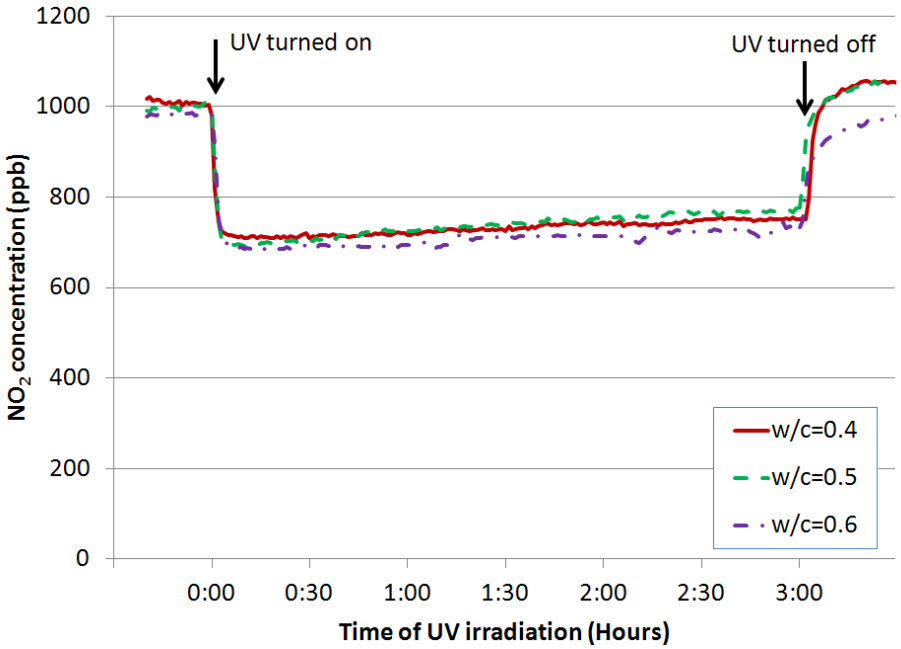

Figure 5.4—NO_2 test data with samples with w/c=0.40, 0.50, and 0.60, each with 5% TiO_2 by mass of cement

Table 5.1-- Photocatalytic efficiency of samples at different times

	Experiment Conditions					
	NO Gas			NO_2 Gas		
w/c	0.4	0.5	0.6	0.4	0.5	0.6
Initial drop (%)	14.0	22.4	31.0	27.7	30.6	30.3
1hr drop (%)	20.5	24.5	29.2	26.9	27.3	29.2
2hr drop (%)	22.4	27.6	29.2	24.2	24.4	27.2
3hr drop (%)	23.6	24.4	28.9	23.5	22.0	25.2

As can be seen from Figures 5.3 and 5.4, the photocatalytic cement is capable of oxidizing both NO and NO_2 gas instantaneously upon initial UV illumination. This is an expected behavior because NO_2 is one of the transitional products in the NO oxidation process [65, 69]. For both of the cases, photocatalytic activity continued throughout the 3-hr test period. When the UV light was turned off, the gas concentration generally recovered back to ~1000ppb, as expected. Overall, by the end of the test, the photocatalytic efficiency values seem to converge to mid 20s for both the NO and NO_2 cases. This trend suggests that similar amounts of NO and NO_2 gases were oxidized at 3 hours when constant concentration (~1000ppb) of gas was provided, regardless of variations in w/c in the range examined.

However, it is worth noting that some differences in photocatalytic efficiency were observed in the NO experiment for the different w/c's examined. While the variation in w/c in the NO_2 experiment did not result in large variations in early oxidation behavior, higher w/c in the paste generally resulted in a greater initial drop in the case of the NO experiment, producing a more rapid rate of oxidation. Specifically, while the w/c=0.4 samples oxidized 14.0% of the gas initially, a 31.0% drop was measured for the

w/c=0.6 pastes. The photocatalytic efficiency of the w/c=0.4 and 0.5 samples increased over time, resulting in comparable values to the w/c=0.6 sample at 3 hours. However, the w/c=0.60 was the most effective, oxidizing 28.9% of the initial NO gas at 3hours, compared to 23.6% and 24.4% for the w/c=0.40 and 0.50 cases respectively. It is proposed that the variations in pore structures among the samples are a main reason for the different behavior among different w/c samples under the NO. That is, other parameters remaining the same, a higher w/c sample has higher porosity, greater degree of pore connectivity, and thus higher surface area where the gas can be sorbed [21, 22, 172], which increases the amount of gas that that can potentially be oxidized. In case of the NO_2 experiment, the effect of variations in w/c and pore structures is not apparent, the possible reason for which is going to be discussed later in this chapter.

To better quantify the influence of w/c on structure, surface area analysis was performed using nitrogen Brunauer-Emmett-Teller (BET) method on these samples using an accelerated surface area and porosimetry system (Micromeritics ASAP2020, Micromeritics, Norcross, GA). Samples were crushed to pass #8 sieve and retained in #16 sieve. Degassing was done at 105°C for 24 hours, and the sample used was ~1g each. The BET surface area was measured to be 19.53 m^2/g, 37.81 m^2/g, and 54.84 m^2/g for the w/c=0.4, 0.5, and 0.6 sample respectively, showing an increase in surface area as w/c increases, as expected. It is hypothesized that the photocatalytic efficiency depends to some extent on the rate of gas sorption within the cementitious system. Thus, at higher w/c, cementitious materials have a greater capacity for NO binding and this facilitates oxidation upon exposure to UV light. The greater complexity of the pore structure at the lower w/c of 0.40 and 0.50 may control the rate at which NO may be bound, thus

producing an increasing photocataltyic efficiency with time, but further investigation is necessary to evaluate this potential effect of w/c.

While the variation in specific surface area with w/c may account for the difference in NO sorption among the samples examined, the difference in sorptivity in the NO and NO_2 experiments must also be examined. Specifically, no apparent differences in efficiency were observed with different w/c in case of the NO_2 case, when comparing Figure 5.3 and 5.4. To better understand the interactions between the cement pastes of varying surface area and the NO and NO_2 gases, it is useful to understand the nature of the gases themselves. The NO molecule is smaller than the NO_2 molecule, having 115pm compared to 221pm. Both the NO and NO_2 molecules are polar, meaning that the dipole-dipole intermolecular forces align the molecules, increasing their attraction to surfaces and reducing potential energy. The dipole moment of the NO and NO_2 are 0.157 D [173] and 0.316 D [174] respectively.

Therefore, it is hypothesized that the more polar NO_2 molecule is more efficiently and more rapidly sorbed within the cementitious structure and that the rate at which this occurs is so rapid that it appears to occur independently of sample porosity for this test setup. As a result, in this case, the rate of sorption does not limit the photocatalytic efficiency in the presence of NO_2, and it is proposed that due to this characteristic, the reaction rate in the presence of NO_2 was steady throughout the experiment.

After the photocatalytic oxidation experiment for the w/c=0.6 case for both the NO and NO_2 gases, the samples were taken out of the UV reactor and the concentration of gases were continued to be measured in the absence of the samples. This “blank experiment” was performed as a preliminary step to examine the sorptivity of the NOx on

cement paste samples. From Figure 5.5 (a) and (b), gas concentration is shown to decrease rapidly at time of ~10 min. when the reactor is opened to remove the samples in both cases. After the samples were removed, the concentration of NO did not change much; the NO concentration quickly recovered to ~925ppb, which is the same level as when the samples were in the reactor. On the other hand, the NO_2 concentration jumped up from ~965ppb to ~1285ppb when the samples were taken out, which is 33% increase. This increase in NO_2 concentration represents the additional flux in gas flow rate necessary to compensate for binding within the cementitious materials while maintaining the desired concentration in the chamber of ~1000ppb. This clearly demonstrates that cementitious materials have a high potential to sorb (or bind) NO_2 compared to NO, and the consistency in the rate of sorption suggests that this effect could also be used to diminish NO_2 levels in the atmosphere.

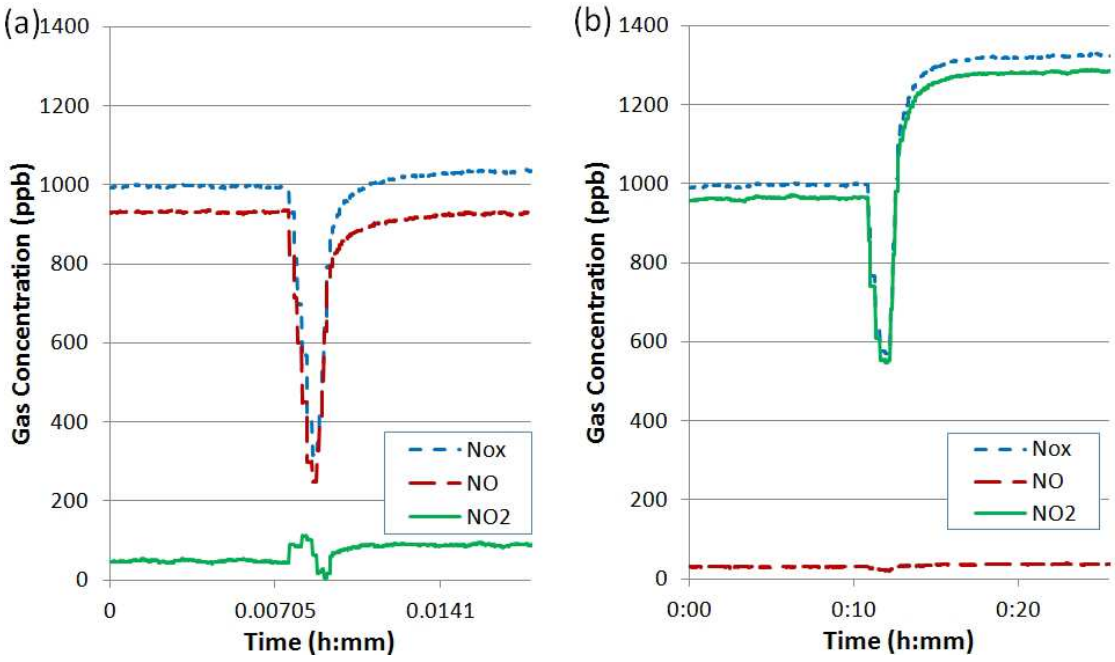

Figure 5.5—Blank concentration: gas concentration after samples taken out of the reactor (a) NO experiment, (b) NO_2 experiment

5.3.2 NO and NO_2 Binding Series

The prior demonstration of NO_2 binding in cementitious materials has not been a subject to much research despite the known coexistence of NO_2 with NO in the atmosphere. To further examine the binding of NO_2 within cementitious materials, an additional series of experiments were undertaken with a goal of better understanding the NOx binding process. Of particular interest is an improved understanding of the potential binding pathways (e.g., gas adsorption to solid surfaces, gas absorption or dissolution in pore solution, etc.) and how these may differ for NO and NO_2. To this end, cement paste samples were introduced to NO or NO_2 environments in either dry or wet states, as previously described.

Results from the NO binding experiment in cementitious materials when the samples were wet and dry are shown in Figures 5.6 (a) and (b) respectively, while Figures 5.7(a) and (b) show the corresponding results from the NO_2 experiment. Rapid decrease in gas concentration near the start and the end of the experiment indicate when the reactor was opened to insert and take out samples. Note that in these experiments, no UV-exposure was used. Interactions between the gases and the cementitious materials result from phenomena other than photocatalysis. For all of the figures, both the NO and NO_2 concentrations were plotted as well as the NOx. This way it is visually clear that the test gas is stable and that the concentration changes in the test gas is not the result of transformation to other type of gas (for instance NO to NO_2 or vice versa).

Comparing Figures 5.6 and 5.7, the results suggest that the NO_2 in general is bound in cementitious materials much more than NO gas as expected, based upon the results from the photocatalysis series. The NO_2 concentration was decreased by 38% and

36% for the wet and dry samples respectively, after 2 hours. The NO concentration was decreased more modestly, by 9% and 2% for the wet and dry samples respectively, after 2 hours. Comparing wet and dry samples, not much difference was observed either for the NO or NO_2 cases after 2 hours: the NO was bound in wet samples 7% more than in dry samples, and the NO_2 was bound in wet samples 2% more than in dry samples. From these results, it was found that the NOx bound in cement paste is slightly higher for the wet samples than the dry samples in both of the cases, which suggests that the pore solution takes part in binding NO and NO_2 through absorption. However, it can be suggested that the effect of gas absorption into pore solution is negligible compared to gas bound on hardened cement paste. Comparing Figures 5.7 (a) and (b), it should be noted that in case of the dry samples of the NO_2 case, as shown in Figure 5.7 (b), the rate of NO_2 concentration recovery after the samples have been inserted is lower than the other cases. This indicates that the rate of adsorption of the NO_2 gas at the early sample exposure is faster than the wet sample case, suggesting that the NO_2 gas is adsorbed faster to hardened cement paste than into pore solution.

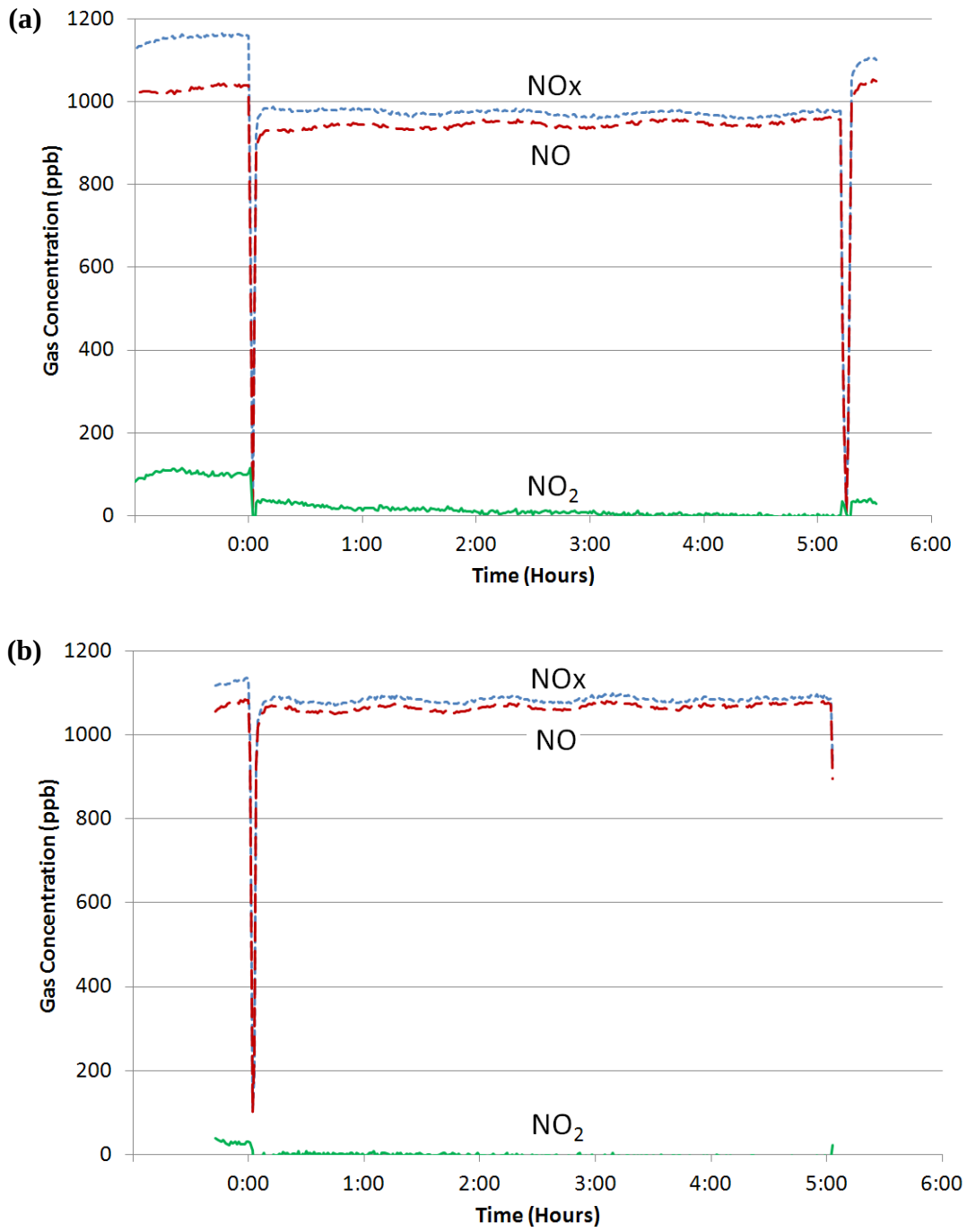

Figure 5.6 — (a) NO gas absorption in wet cement paste samples,

(b) NO gas absorption in dry cement paste samples

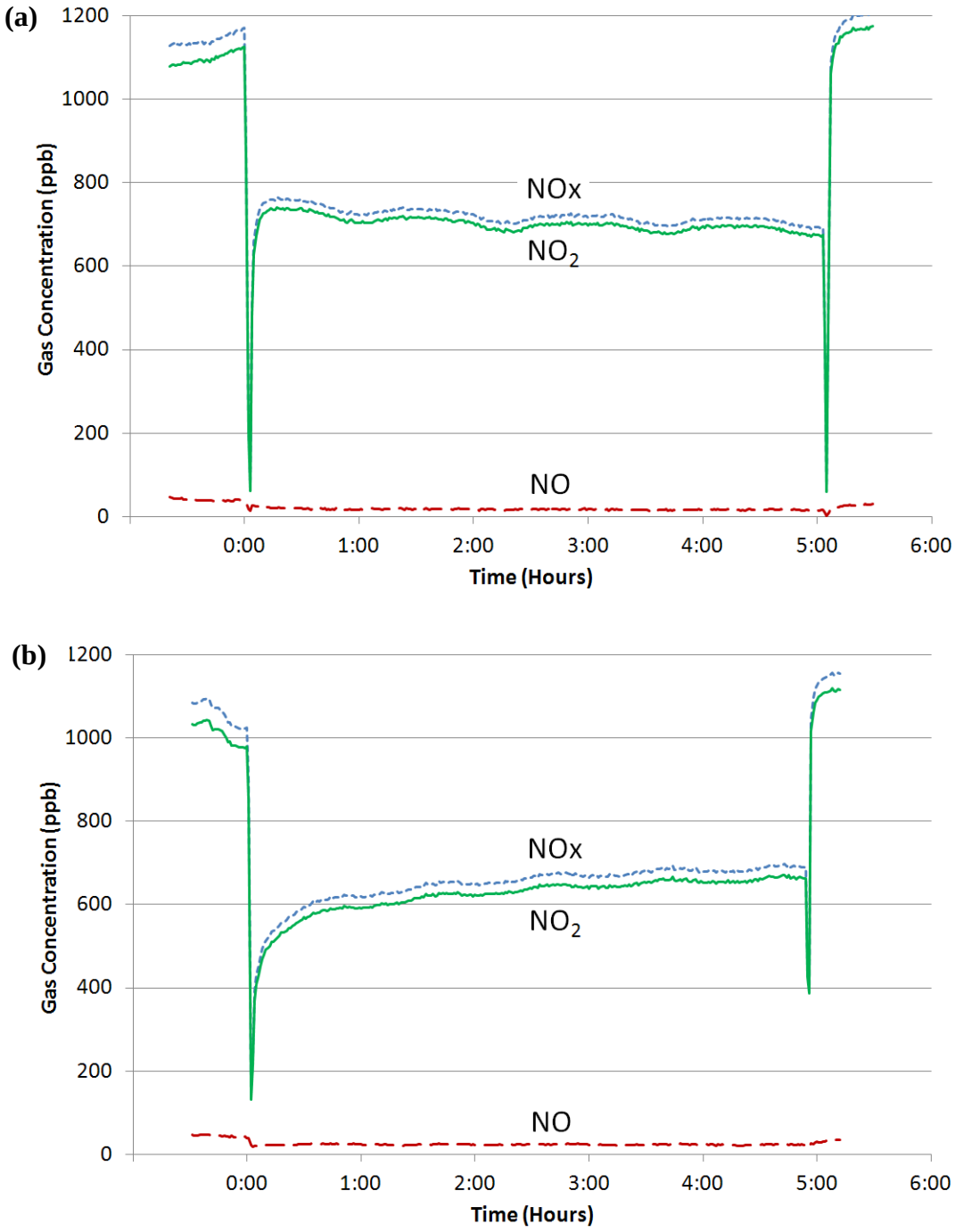

Figure 5.7 — (a) NO_2 gas absorption in wet cement paste samples,

(b) NO_2 gas absorption in dry cement paste samples

The results from Figures 5.6 and 5.7 again suggest that the NO_2 has a greater potential to be bound into cementitious substrate than the NO gas, despite of its larger molecular size. It is proposed that it can be explained by differences in polarity of the two molecules, as stated previously. The NO_2 gas has about twice higher dipole moment than the NO gas, which suggests higher attractive force to surfaces with a net surface charge and to other polar molecules. Thus, it can be envisioned that in addition to sorbing to the cementitious solids, the NO_2 gas can be stacked in layers, resulting higher amount of adsorption compared to the NO gas.

To examine the effect of pore solution alone on the decreases in NOx gas, a simple experiment was performed in the presence of synthetic cement pore solution. The experimental set up was identical to NOx binding series, except a shallow bath of synthetic cement pore solution, composed of saturated calcium hydroxide solution plus 0.7M sodium hydroxide [175], was used in place of cement paste samples. About 65g of solution was used in a shallow plastic dish for each experiment, with an effective surface area of 200cm^2. The solution was exposed to each gas concentration at ~1000ppb for more than 15 hours. Figures 5.8 (a) and (b) show the gas concentration changes when the solution is installed for the NO and NO_2 respectively.

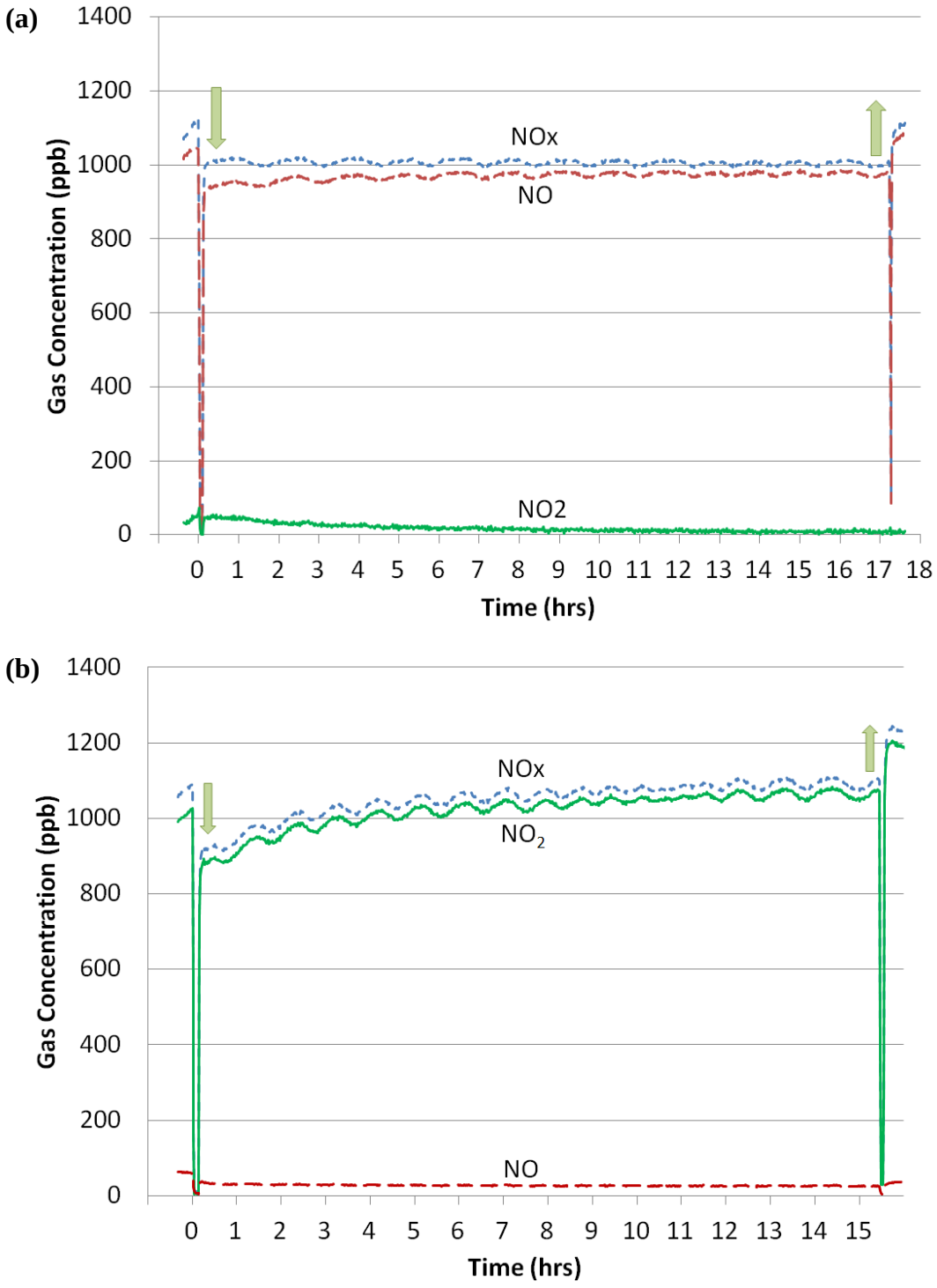

Figure 5.8— (a) NO gas absorption in synthetic pore solution,

(b) NO_2 gas absorption in synthetic pore solution

The concentration of NO and NO_2 dropped by approximately 10% of the initial gas concentration, or ~100ppb and ~130ppb respectively, on average during the period of the experiment. The rate of this decrease, thus the difference between the base NOx supply and the concentration with the pore solution, was relatively consistent throughout the experiment which lasted more than 15 hours. This suggests that some of the NO and NO_2 gas molecules were absorbed constantly into pore solution, with the NO_2 gas being absorbed in greater quantities by 30 ppb. The decreased amount of NO and NO_2 in pore solution during the full length of experiment were calculated and it was determined to be 31μmol and 43μmol per kilogram of synthetic solution respectively. However, this absorption rate exceeds the conventional solubility of NO and NO_2 in water. Henry's constant for the NO and NO_2, thus their solubility in water, were reported to be 0.0019 mol/kg·bar [176] and 0.012-0.041 mol/kg·bar [177, 178]. It can be calculated that 1100 kg and 65-220 kg of water are needed to absorb same amount of NO and NO_2 as in the pore solution experiment. This suggests that composition and high ionic concentration of the synthetic pore solution might have played a role in additional chemical reaction between gas molecules. Kameoka et al. [179] observed similar increases in NO_2 solubilities in industrial-type solutions such as sodium sulfite. Also, the alkaline pH of the solution and low gas concentration (1ppm) could have affected the solubility of gases. However, it should be noted that the amount, chemical composition, and accessibility of pore solution in actual cement-based materials would be totally different from a bath of synthetic pore solution, and these results should be understood qualitatively. From this experiment, it can be concluded that NO and NO_2 can be absorbed in cement pore

solution, suggesting that absorption is one of the mechanisms that the NOx be bound in cementitious system.

The hypotheses made in this chapter on NO_2 sorption mechanisms are visually presented in Figure 5.9. The NO_2 gas molecules are more easily adsorbed on dry hardened cement paste than absorbed to pore solution. The NO_2 molecules are easily stacked in layers to hardened cement paste due to its high dipole moment, thus having a high potential to adsorb the NO_2. The NO_2 is also absorbed into pore solution, where it remains as nitrates.

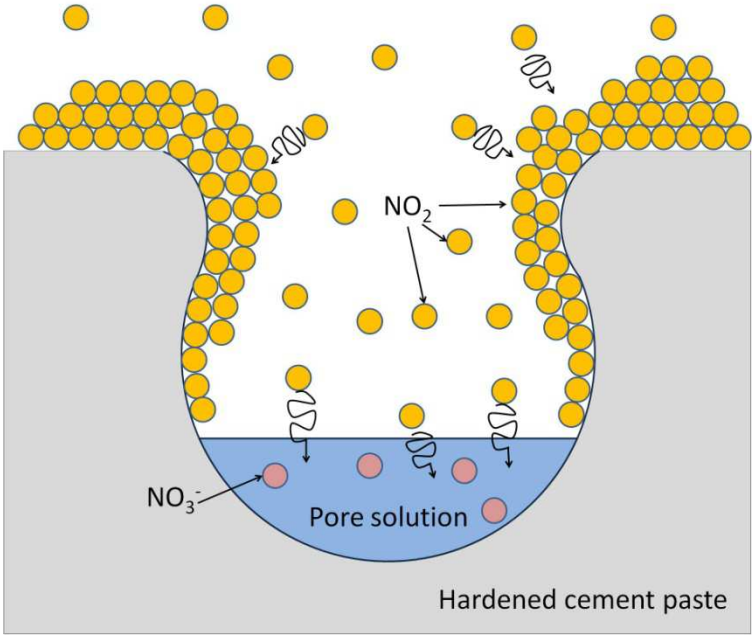

Figure 5.9— NO_2 sorption on hardened cement paste as well as into pore solution

Focusing on the NO_2 case, it is interesting to compare the results from the NO_2 binding series (Figure 5.7) to the photocatalytic series (Figure 5.4). The NO_2 drop due to binding was ~37% from the initial ~1000ppb when the cement samples were inserted.

The NO_2 photocatalytic efficiency was ~25-30%. Although these data cannot be compared quantitatively due to the differences in the experimental procedures (i.e., the measurements in the photocatalytic series were started only once the gas is fully stabilized or after the gas was bound in cementitious material), even a qualitative comparison allows for the observation that the amount of NO_2 bound in cement paste is on the order of the amount that is oxidized due to the TiO_2 photocatalytic reaction. It should also be noted from Figure 5.7 that the NO_2 is sorbed into cement paste continuously throughout 5 hour experimental period. This suggests that, even in the absence of photocatalysis, cement pastes can bind large amount of NO_2 and that this binding can continue over relatively long exposure times.

5.4 Conclusions

In this chapter, the photocatalytic efficiency and NOx binding capacity of TiO_2-containing cement-based materials under NO and NO_2 gas were experimentally examined.

In the photocatalysis series, similar amounts of NO and NO_2 gases were oxidized at 3 hours, regardless of variations in w/c, suggesting that the TiO_2 bearing cementitious materials are capable of oxidizing both gases efficiently at long time exposure. However, some variations were observed between different w/c for the NO case at early exposure, and it is proposed that the high surface area for the high w/c affects the amount of gas that can be sorbed, and thus can potentially be oxidized. This was not observed for the NO_2 case, and it is hypothesized that the more polar NO_2 is sorbed more rapidly and sample porosity does not limit the oxidation rate.

In the NO and NO_2 binding series, the NO_2 gas had a greater potential to be bound into cementitious materials than the NO gas, again it is proposed this is due to the higher dipole moment. It was found that the cement pore solution absorbs part of the NO and NO_2 gas, but the amount was negligible compared to the gas bound on hardened cement paste. It was also found that the rate of NO_2 binding was faster at early exposure in case of dry samples than in wet samples, suggesting that the NO_2 gas was more easily bound to hardened cement paste than into pore solution.

Comparing both series for the NO_2 case, it can be concluded that the amount of NO_2 bound into cementitious material is comparable to the amount oxidized by photocatalytic reaction. The great potential of the NO_2 gas to bind into cement-based materials suggests, on the basis of its contribution to reductions in atmospheric NOx, that concrete itself can be considered as an environmentally friendly construction material. This is especially beneficial because the NO_2 directly affects human respiratory tract compared to NO. Furthermore, when used with TiO_2, its binding ability supports the oxidation reaction by providing sufficient supply of gas molecules. Overall, these experiments indicate that the TiO_2 containing cementitious materials are an efficient way of decreasing NOx level in the atmosphere, not only through photocatalysis, but also through binding NOx within the cementitious materials. It is suggested, from this research, that higher w/c up to w/c=0.6 is favorable to be used for both NO and NO_2 gas oxidation, so that the material can be efficient under both gases.

5.5 References

5. WHO, *Air quality guidelines, Global update 2005.* World Health Organization, 2005.

21. Chen, J. and C.S. Poon, *Photocatalytic activity of titanium dioxide modified concrete materials - Influence of utilizing recycled glass cullets as aggregates.* Journal of Environmental Management, 2009. **90**(11): p. 3436-3442.

22. Ramirez, A.M., et al., *Titanium dioxide coated cementitious materials for air purifying purposes: Preparation, characterization and toluene removal potential.* Building and Environment, 2010. **45**(4): p. 832-838.

45. Vallee, F., et al. *Innovative self-cleaning and de-polluting facades surfaces.* in *CIB World Building Congress*, 2004. Toronto, Canada.

65. Devahasdin, S., et al., *TiO_2 photocatalytic oxidation of nitric oxide: transient behavior and reaction kinetics.* Journal of Photochemistry and Photobiology a-Chemistry, 2003. **156**(1-3): p. 161-170.

69. Laufs, S., et al., *Conversion of nitrogen oxides on commercial photocatalytic dispersion paints.* Atmospheric Environment, 2010. **44**(19): p. 2341-2349.

98. JIS, *Fine ceramics (advanced ceramics, advanced technical ceramics) - Test method for air purification performance of photocatalytic materials* in *Part 1: Removal of nitric oxide*2004.

99. ISO, *Fine ceramics (advanced ceramics, advanced technical ceramics) - Test method for air-purification performance of semiconducting photocatalytic materials*, in *Part 1: Removal of nitric oxide*2007.

170. Yao, X., et al., *The use of tunnel concentration profile data to determine the ratio of NO_2/NOx directly emitted from vehicles.* Atmospheric Chemistry & Physics Discussions, 2005. **5**(6): p. 12723-12740.

171. Yoshio, T., et al., *NOx removal with titanium dioxide coating on acoustic material composed of waste polystyrene foam and cement.* Journal of Japan Society for Atmospheric Environment, 2003. **38**(4): p. 227-235.

172. Powers, T.C., *Structure and physical properties of hardened portland cement paste.* Journal of the American Ceramic Society, 1958. **41**(1): p. 1-6.

173. Hoy, A.R., J.W.C. Johns, and A.R.W. McKellar, *Stark Spectroscopy with the CO Laser: Dipole Moments, Hyperfine Structure, and Level Crossing Effects in the Fundamental Band of NO.* Canadian Journal of Physics, 1975. **53**(19): p. 2029-2039.

174. Hodgeson, J.A., E.E. Sibert, and R.F. Curl, *Dipole moment of nitrogen dioxide.* The Journal of Physical Chemistry, 1963. **67**(12): p. 2833-2835.

175. Kurtis, K.E., et al., *Imaging of ASR gel by soft X-ray microscopy.* Cement And Concrete Research, 1998. **28**(3): p. 411-421.

176. Armor, J.N., *Influence of pH and ionic strength upon solubility of nitric oxide in aqueous solution.* Journal of Chemical & Engineering Data, 1974. **19**(1): p. 82-84.

177. Chameides, W.L., *The photochemistry of a remote marine stratiform cloud.* J. Geophys. Res., 1984. **89**(D3): p. 4739-4755.

178. Lee, Y.N. and S.E. Schwartz, *Reaction kinetics of nitrogen dioxide with liquid water at low partial pressure.* The Journal of Physical Chemistry, 1981. **85**(7): p. 840-848.

179. Kameoka, Y. and R.L. Pigford, *Absorption of nitrogen dioxide into water, sulfuric acid, sodium hydroxide, and alkaline sodium sulfite aqueous solutions.* Industrial & Engineering Chemistry Fundamentals, 1977. **16**(1): p. 163-169.

CHAPTER 6

DURABILITY OF PHOTOCATALYTIC CEMENT AFTER NITROGEN OXIDES – WET – DRY CYCLING

6.1 Introduction

In chapter 5, the photocatalytic cement was shown to effectively oxidize both NO and NO_2 gases under UV light, thus improving air quality. However, there has not been much study regarding the effect of the product of the oxidation reaction (nitrates and nitrites) on cementitious materials. Since cement-based materials undergo chemical reactions throughout their lifetime, it is crucial to investigate any changes that might occur in relation to products of NOx oxidation in order to assure long-term durability.

It is possible that damaging acid attack, salt crystallization, and/or carbonation can occur as ancillary reactions during photocatalysis of TiO_2 on the surface of cementitious materials. Chapter 2 presents an overview of the potential reaction pathways and the influence of these reactions on cement-based materials. The objectives of this study were to examine whether the oxidation of NOx during the photocatalysis could influence the durability of cementitious substrate, and to investigate the NOx oxidation efficiency in the long term. To this end, TiO_2-containing cement pastes were exposed to environmental conditions meant to simulate and also accelerate environmental exposures that could possibly lead to degradation of this material, through acid attack and salt crystallization. Both NO and NO_2 gases were utilized for this study, and samples were exposed to cycles of NOx and UV (i.e., surface photocatalysis) along with wetting and

drying conditions. To quantify the influence of these surface reactions on the cement substrate, the surface of each set of samples was examined by scanning electron microscopy (SEM), Vickers microhardness, surface roughness, and x-ray diffraction analysis. In addition, photocatalytic efficiency and mass changes were monitored throughout the experiment

6.2 Experiment

The overall experiment follows a process shown in Figure 6.1. Once the samples are prepared, which will be explained into more detail in 6.2.1, surfaces of test samples were examined prior to the exposure to NOx and UV in order to establish a base measurement. Then, the samples were subjected to multiple cycles of environmental exposures, termed as “cycling” in this paper. One cycle starts with exposure to NOx test gas and UV light for the photocatalytic reaction, followed by wetting and drying, and then the next cycle starts again by exposure to NOx and UV. These cycling were designed to simulate real world situation where photocatalytic materials go through various weather conditions, such as rain/dew and dry weather, which could possibly affect long term durability of the cementitious substrate as stated in Chapter 2. During the course of these cycling, sample surfaces were examined after the drying step of every 5 and 4 cycles for the NO and NO_2 experiments respectively, in order to capture any gradual changes in their physical, mechanical, and chemical properties. Specific details on the methodology of the cycling and surface examination are discussed in 6.2.2 and 6.2.3 respectively.

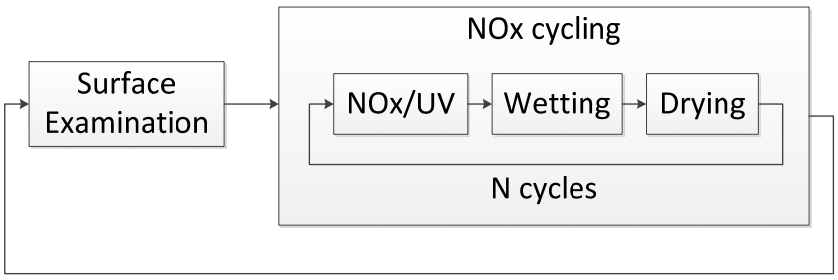

Figure 6.1—Diagram of the experimental process

In the first part of the study, nitric oxide (NO) was selected as the test gas for the experiment, as described in most of the standard testing [98, 99]. Upon analyzing results from the NO experiment, it was concluded that the exposure condition planned was not strong enough to generate distinctive changes on the samples in an acceptable amount of time. Thus, the second part of the study was planned again in an attempt to further accelerate any damages that might take due to combination of photocatalytic reactions and wet-drying. Most importantly, the test gas was changed to nitrogen dioxide (NO_2). It was hypothesized from several studies that the NO_2 is closer to the final products of photocatalytic oxidation than the NO [70], meaning that the rate of degradation as a result of these final oxidation products is going to be increased. While the NO needs to go through complicated process, such as being transformed to NO_2 when oxidized by TiO_2 particles, the reaction path is shorter for the NO_2, thus the NO_2 is a more direct source for the final products. In addition, other experimental parameters were also modified for the NO_2 experiment so that the samples are more susceptible to degradation and to possibly accelerate the rate of damage. The detailed experimental parameters of the NO and NO_2 experiments are going to be introduced into more detail, later in this chapter in 6.2.1 and 6.2.2 with a comparison listed in Table 6.1. The NO_2 experiment was performed basically

following the same procedure as the NO experiment, shown in Figure 6.1. Throughout this chapter, the first part of the study using the NO gas will be termed as "NO experiment" and the part using NO_2 gas will be termed as "NO_2 experiment."

6.2.1 Materials and Sample Preparation

6.2.1.1 NO Experiment

Cement paste samples containing nano-TiO_2 particles were prepared. The TiO_2 powder utilized was P25 (Aeroxide TiO_2 P25, Evonik Industries). The TiO_2 powder consisted of 80% anatase and 20% rutile with an average crystal size of 21nm. The surface area is 50±15 m^2/g, and the sample purity is 99.5% as stated by the manufacturer. The cement used was ASTM C 150 Type Ⅰ portland cement, and the Bogue potential composition of which was 51.30% C_3S, 19.73% C_2S, 8.01 C_3A, and 9.41% C_4AF. (The cement chemistry notations of these oxides are defined as C=CaO, S=SiO_2, F=Fe_2O_3, and A=Al_2O_3.)

The samples were prepared at w/c of 0.50 at 5% TiO_2 replacement by mass of cement. When mixing, TiO_2 particles were pre-mixed with deionized water for 1 minute using a hand-held mixer at a low speed. Cement was then added to the TiO_2 slurry and mixed for 1 additional minute at a low speed and another 1 minute at a medium speed. Samples were cast in plastic molds with dimensions of 4.8cm x 4.8cm x 0.8cm. They were allowed to cure in a 100% relative humidity environment at 23±2°C for the initial 24 hrs, and continued to be cured in limewater after demolding at 23±2°C. The samples were taken out of the limewater at 14 days of age, polished to 0.3 μm, and dried in the

oven at 30°C for 3 complete days. The samples were polished to better identify microhardness marks. The dried samples were stored in air-tight plastic bags until tested.

The NO gas was obtained at 100 ppm cylinder. It was mixed with ultra pure zero air (~80% nitrogen and ~20% oxygen) to a target value of 1200 ppb at the output of the UV reactor when the samples are installed. Mass flow controller was used for both the NO and the zero air to achieve desired concentration constantly.

6.2.1.2 NO_2 Experiment

Cement paste samples that contains TiO_2 nanoparticles were prepared, that are similar to the NO experiment. The same TiO_2 powder was utilized for this experiment, but the cement composition was changed inevitably because this part of the experiment was not planned initially and the original cement was unavailable. The new cement used was ASTM C 150 Type Ⅰ portland cement, and the Bogue potential composition of which was 54.00% C_3S, 18.00% C_2S, 6.70 C_3A, and 10.00% C_4AF.

Samples were made into the same dimensions as the NO experiment, but now they were prepared at w/c of 0.60 and at 10% TiO_2 replacement by mass of cement. The higher w/c was used to decrease compressive strength and to increase porosity. There is a general agreement that strength of a material is a critical factor for salt scaling, and Valenza et al. states in their paper that the salt scaling resistance of a material should be satisfactory as it reaches 40MPa [109]. From the compressive strength results in Chapter 3, it was shown that the w/c plays a significant role, such that higher w/c results in lower compressive strength (Figure 3.6). In case of the cement paste sample with w/c=0.6 and 10% TiO2 replacement, the strength was 43MPa, marginally reaching 40MPa at its lower

end. The increased porosity would allow more water and salts to penetrate into cement samples, if any, which would participate in salt crystallization upon multiple wetting and drying, ultimately generating salt crystallization pressure. Higher w/c samples would also be more susceptible to acid attack because the acidic solution could penetrate deeper into cementitious materials than lower w/c case due to high porosity and permeability. The higher percentage of TiO_2 was used to promote higher rate of photocatalytic reaction, thus expecting more final products to form. Samples were prepared and cured in the same manner as the NO experiment. However, the samples for the NO_2 experiment were cured until 28 days, as compared to 14 days for the NO experiment, giving the samples enough time for strength and hardness gain so that constant mechanical properties baseline can be achieved. The surfaces of the samples were polished only up to 5μm because this level was found to be sufficient for microhardness measurements. Then, the samples were dried in the oven at 30°C for 3 complete days, and stored in air-tight plastic containers until tested.

The NO_2 gas was obtained at 100 ppm cylinder, same concentration as the NO, from the same vendor. The NO_2 was mixed with ultra pure zero air, similar to the NO mixture, to a target value of 1000 ppb at the output of the UV reactor when the samples are installed. The mass flow controllers were also used.

6.2.2 Experimental Procedure

The general procedure for the cycling was already introduced in Figure 6.1. In this section, specific details of each of the steps, the NOx-UV experiment, wetting, and drying, are introduced. Each cycle starts with the NOx-UV experiment. This step uses the

same apparatus, or chamber, that is previously introduced in Chapter 5. The schematic of the test setup is shown in Figure 5.2. Before and between each cycle, the samples were stored in air-tight plastic bags in a dry condition. After the installation of the samples in the chamber, either a constant concentration of NO or NO_2 was injected until the gas concentration is stabilized, which takes at least one hour. Gas flow rate was decreased from 1000 ml/min in case of the NO experiment to 500 ml/min in case of the NO_2 experiment, in order to allow enough time for the oxidation reaction on the sample surfaces and thus expecting higher amounts of oxidation products to form. During the gas stabilization time, the UV light was turned on for 15 minutes with a shutter closed to warm it up. Once the gas was stabilized, the shutter was opened and the samples were exposed to the UV irradiation, meaning the onset of photocatalytic reaction. The NOx-UV exposure time for the NO experiment was 5 hours for all the cycles, which was increased to 24 hours in case of the NO_2 experiment in an attempt to increase the amount of oxidation and thus final products. After the designated time of UV exposure, the UV light was turned off and the gas concentration was kept recorded until the concentration is stabilized again, which took about one hour. Then, all the gas supply was stopped and the samples were collected and transported in an air-tight container for wetting. The humidity of the test gas was maintained at 50% RH. The photocatalytic oxidation efficiency was determined twice for each run; the first was measured by the drop of NOx concentration when the UV light was turned on, and the second was measured by the amount of NOx concentration recovery when the UV light was turned off. The results were normalized by the number of tiles, where the individual tile surface area was kept constant at ~23cm^2.

After the NOx-UV exposure, samples were subjected to wetting and drying process to simulate rain/dew and dry conditions which could contribute to the deterioration of these cementitious materials. For each sample, 0.75 g of deionized water was uniformly spread on top surface of a sample, which corresponds to 0.3mm of water layer, simulating dew or light rain. Only the top surfaces of the specimen were wetted where the photocatalytic reaction takes place. The samples were then stored in a 100% RH container for 4 and 3 hours for the NO and NO_2 experiment respectively. The wetting time was decreased for the NO_2 experiment because the samples were made at higher w/c, meaning that water could penetrate much faster than the lower w/c. During this time, the water and products of NOx oxidation could penetrate into cementitious materials that could possibly contribute to deterioration. Following the wetting, samples were dried in an oven at 40°C. The drying time was 15 hours for the NO experiment and 40 hours for the NO_2 experiment. The increased drying time in case of the NO_2 experiment was determined by the minimum time required to dry the samples until there is no mass changes. After the drying step, sample mass was measured and the next cycle was performed by exposing samples to the NOx-UV. This cycling was repeated for 20 cycles and 14 cycles for the NO and NO_2 cases respectively. Since there are large variations in the experimental parameters such as duration of NOx exposure, the number of cycles performed does not hold great importance. The key experimental parameters between the NO and NO_2 experiments are summarized in Table 6.1.

Table 6.1. Summary of the experimental conditions: NO and NO_2 experiments

Gas	Sample w/c	Curing time (days)	Initial gas concentration (ppb)	Gas flow rate (ml/min)	NOx+UV exposure duration (hr)	Wetting duration (hr)	Drying duration (hr)	N: Number of cycles between examination
NO	0.5	14	1200*	1000	5 hrs	4	15+	5
NO_2	0.6	28	1000*	500	24 hrs	3	40+	4

* The initial gas concentration measured at the outlet is lower than the actual input concentration due to gas adsorption on the setup and the samples.

6.2.3 Surface Examinations

Before and between cycling, sample surfaces were examined. For the NO experiment, the surface examination was done every 5 cycles and for the NO_2 experiment, it was done every 4 cycles. The NO_2 experiment was considered to be harsher so smaller interval was taken. Sample surfaces were examined by four different techniques: scanning electron microscopy (SEM), Vickers microhardness, surface roughness, and x-ray diffraction analysis.

Scanning electron microscopy was used to visualize and compare the surface morphology before and after the NOx-wet-dry cycling. This method is suitable for microcharacterization of the sample surface because of its high magnification. For the SEM, a sample was carefully broken into small pieces and conditioned in an oven at 30°C for three days before the analysis. Samples were neither surface-treated nor coated in an effort to preserve and capture the surface after possible changes.

Microhardness of the sample surfaces was examined by Vickers indenter per ASTM C 1327 standard [180] in order to evaluate any changes in the mechanical properties of the sample surfaces after repeated exposure to the NOx-UV and wet-drying. This technique is suitable for investigating microstructural mechanical properties on surface of a material, and has been used in several earlier studies on cement pastes, mortars, and concretes [130-132, 142]. Three samples were pre-selected for this purpose throughout the experiment, and ten indentations per each sample were made after designated number of cycles at locations free from any visible surface defects, for consistency. The hardness value is known to be irrespective of load, and loading was increased from 1000gf to 2000gf for the NO and NO_2 experiments respectively to read

indentation marks clearly. Vickers hardness numbers for the 30 indentations were averaged and standard deviations were calculated. A sample Vickers hardness mark is shown in Figure 6.2.

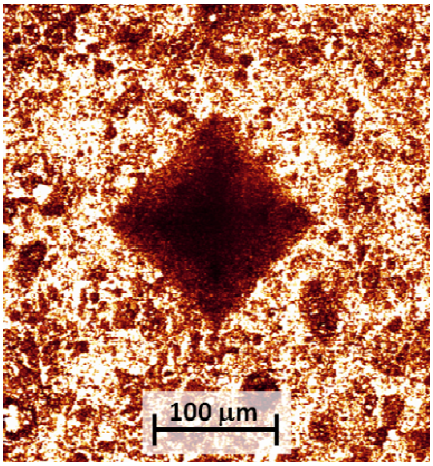

Figure 6.2—Vickers indentation mark obtained after 15 cycles on NO experiment

Surface roughness was examined to quantify any physical changes at the surface due to NOx-wet-dry cycling. One sample was selected for this purpose throughout each of the NO and NO_2 experiment. The same ten locations were examined throughout each of the experiment for comparison of changes with exposure. Laser confocal microscope was used at 20x magnification objective, and 3D images were reconstructed by scanning every 3 micrometer z-depth intervals. Here, surface roughness was calculated by dividing the actual surface of a specimen by projected area. The results from the 10 measurements were averaged and standard deviation was calculated. The example of a sample surface reconstructed by confocal microscope is presented in Figure 6.3.

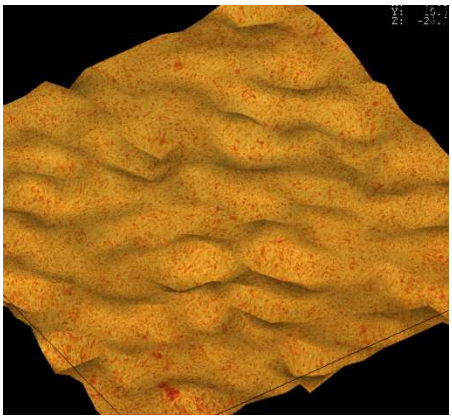

Figure 6.3—Surface reconstructed after 15 cycles on NO experiment using confocal microscope. Each direction measures 500 micrometers.

X-ray diffraction analysis was performed to qualitatively assess any chemical changes that might have occurred during the photocatalytic oxidation and wet-drying cycling near the surface of samples. Surface of a sample was scraped to ~1mm depth with a razor blade. The powder was then ground with mortar and pestle and analyzed under Cu-Kα radiation for 12.5 hours at 2θ from 5° to 65°. Diffraction patterns were normalized by the peak of TiO_2 at 2θ=25.43 for accurate comparison.

In addition to the surface examinations, sample mass was measured after each cycle with a precision of 0.01g.

6.3 Results and Discussion

6.3.1 Photocatalytic Efficiency

Photocatalytic efficiency of the NO and NO_2 experiments were determined at each NOx-UV cycle. For each experiment and with both gases, a sharp drop of gas

concentration was observed when the UV light was turned on, and a quick recovery of gas concentration level was observed when the UV light was turned off, similar to the results presented in Chapter 5. This is a well-known behavior of a photocatalytic reaction, such as on the surface of cement. Among all the NOx concentration plots from each cycle, the plots for the first cycle of the NO and NO_2 cases are presented in Figures 6.4 (a) and (b) respectively. The number of samples used for the NO and NO_2 experiment were 6 and 13 respectively, thus the results presented should be normalized by the exposed surface area of samples to get the photocatalytic efficiency. Note that the concentration of the NO_2 is plotted in the NO test and vice versa, so as to show the amount of gas conversion between NO and NO_2 during the test if any.

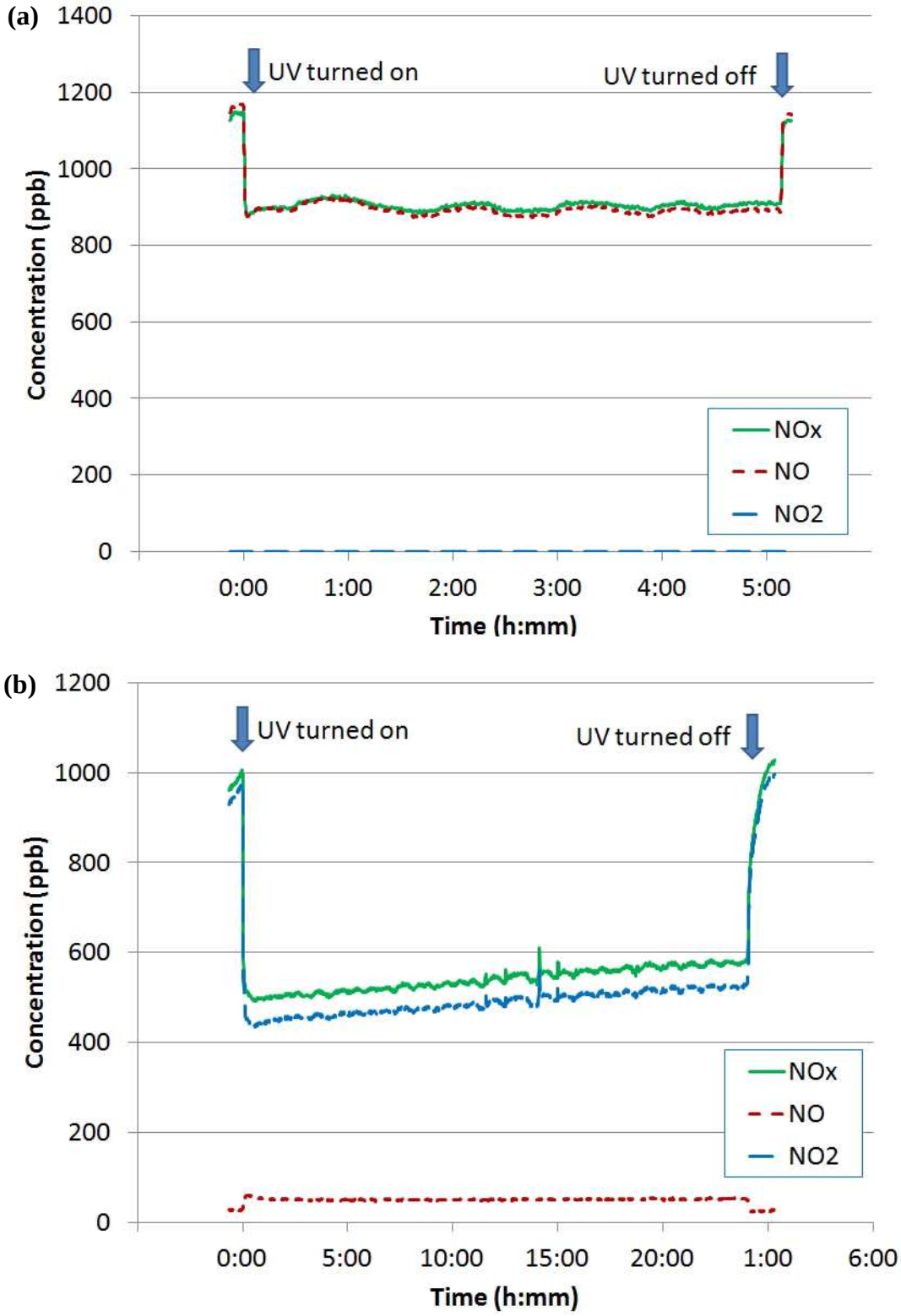

Figure 6.4—NOx, NO and NO_2 concentration at 1st cycle

(a) NO experiment (b) NO_2 experiment

Both the initial drop of NOx concentration when the UV light is turned on and the final increase of NOx concentration when the UV light is turned off were measured. For example, the initial drop and the final increase of NOx in case of the NO_2 experiment would be 493ppb and 444 ppb respectively (Figure 6.4 (b)). The results were divided by the number of tiles to facilitate comparison. For example, the photocatalytic efficiency per tile for NO_2 experiment when the UV light was turned on and when it was turned off would be 38ppb and 34ppb respectively. The photocatalytic efficiency per sample was calculated for each cycle for the NO and NO_2 experiments, and the results are shown in Figures 6.5 (a) and (b). It was observed, for the NO case, that the maximum NOx binding rate happened at 4^{th} – 6^{th} cycle with ~55ppb and reduced to ~25ppb at 20^{th} cycle (Figure 6.5 (a)). For the NO_2 gas case, the maximum NOx binding rate was observed at 1^{st} cycle with ~35-40ppb and reduced to less than 10ppb at 14^{th} cycle (Figure 6.5 (b)). Throughout both of the NO and NO_2 experiments, the amounts of initial NOx drop and final NOx increase for each cycle were similar, indicating that NOx binding rate was relatively steady throughout each NOx-UV exposure. The differences between the initial and final NOx concentration in each cycle varies up to 10ppb, which could be explained as an experimental error, such as due to sample storing condition, minor temperature changes, and NOx stabilization level. Interestingly for both cases, it was observed that the NOx binding rate decreased as number of cycles increased. That is, the repeated NOx exposure and wet-dry cycling caused negative effect on the photocatalytic oxidation. Considering that the TiO_2 particles are responsible for the reaction and they do not change during chemical reactions, this suggests that the sample surface has been modified due to photocatalytic NOx oxidation. Possible explanations are discussed later in this chapter.

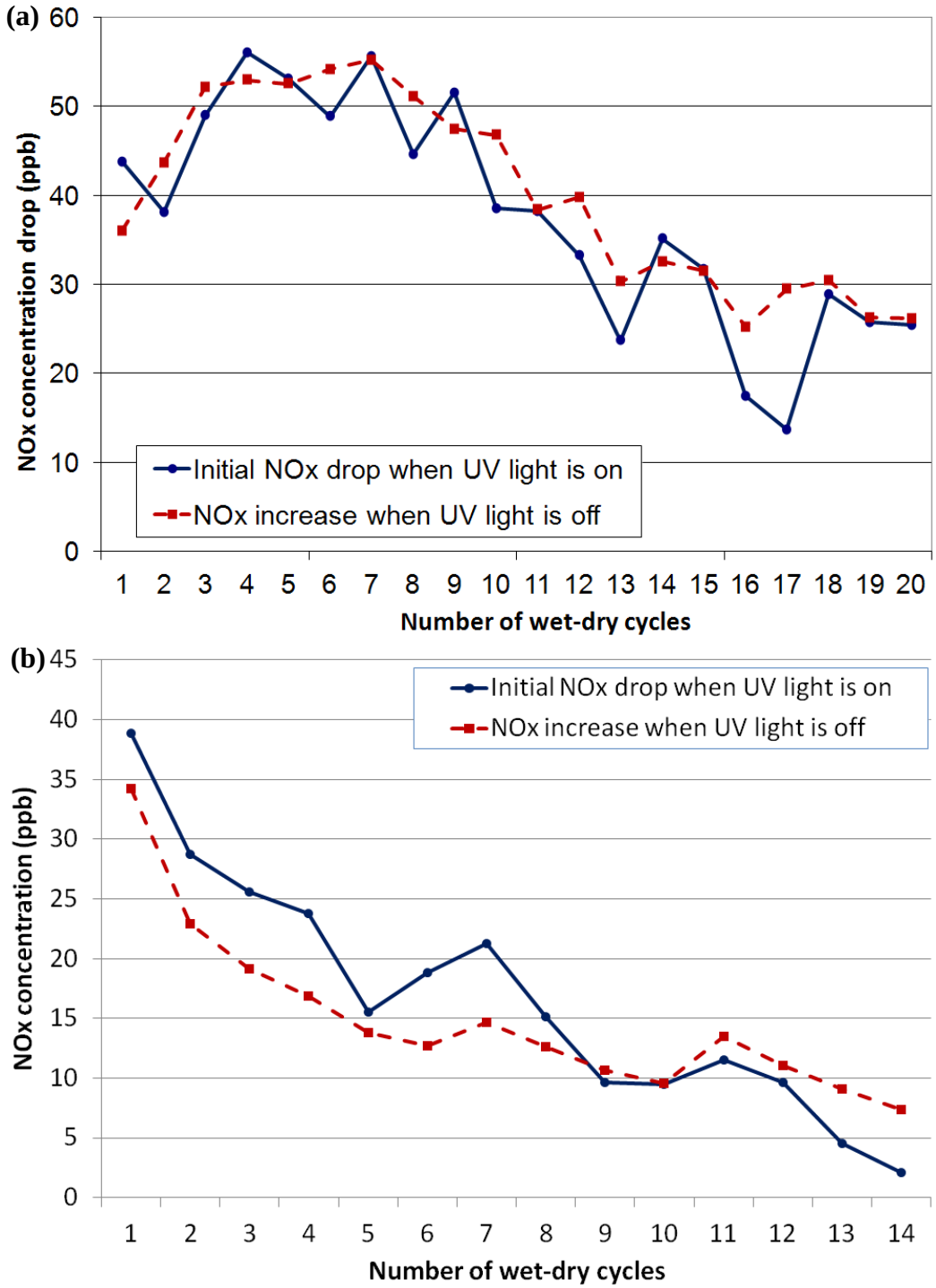

Figure 6.5—(a) NO experiment: NOx concentration changes per tile when UV light is on/off (b) NO_2 experiment: NOx concentration changes per tile when UV light is on/off.

6.3.2 Scanning Electron Microscopy

Scanning electron microscopy was used to closely examine the surface of a sample exposed to NOx-UV and wet-dry cycling. Figure 6.6 presents SEM images of samples under NO gas at 0 and 20^{th} cycle, and Figure 6.7 presents images of samples under NO_2 gas at 0 and 12^{th} cycle. From Figure 6.6 (a) and (b), it was observed that pits less than 1μm were created on the sample surface with exposure to NO-wet-dry cycling.

In Figure 6.7, changes are also apparent in the samples under NO_2 and wet/dry cycling. Visually, the surface after 12 cycles seems to be rougher compared to 0 cycle. However, these were not of sufficient size to be quantified by confocal microscopy, which is discussed in 6.3.4. As with the NO-exposed samples, pits were also found from the sample exposed to NO_2, but in this case they are larger in size reaching more than 20 μm in diameter and occur with greater frequency across the surface. This suggests that more severe damage has been occurred at the surface of the NO_2 exposed sample. It is not clear if these differences in the apparent damage are due to differences in mix design or environmental conditions, or perhaps a combination.

From both of the cases, the pits suggest that there has been either chemical deterioration by acid attack or leaching, or the TiO_2 particles could have been lost due to the deterioration. The TiO_2 particles might have been popped out of the surface due to the loss of bonding or because of the oxidation products accumulating on the surface of the TiO_2 particles, and possibly be lost. This can be related to the lower photocatalytic efficiency with continued cycling as shown in Figure 6.5. Higher w/b in case of the NO_2 case supports this idea. It is expected that further cycling will create more of these pits and develop current pits deeper and wider. Overall, the results suggest that the NOx-UV

exposure and wet-dry cycling do affect cementitious materials by deteriorating surfaces. Further research is needed to examine how the damage may progress with longer duration of exposure.

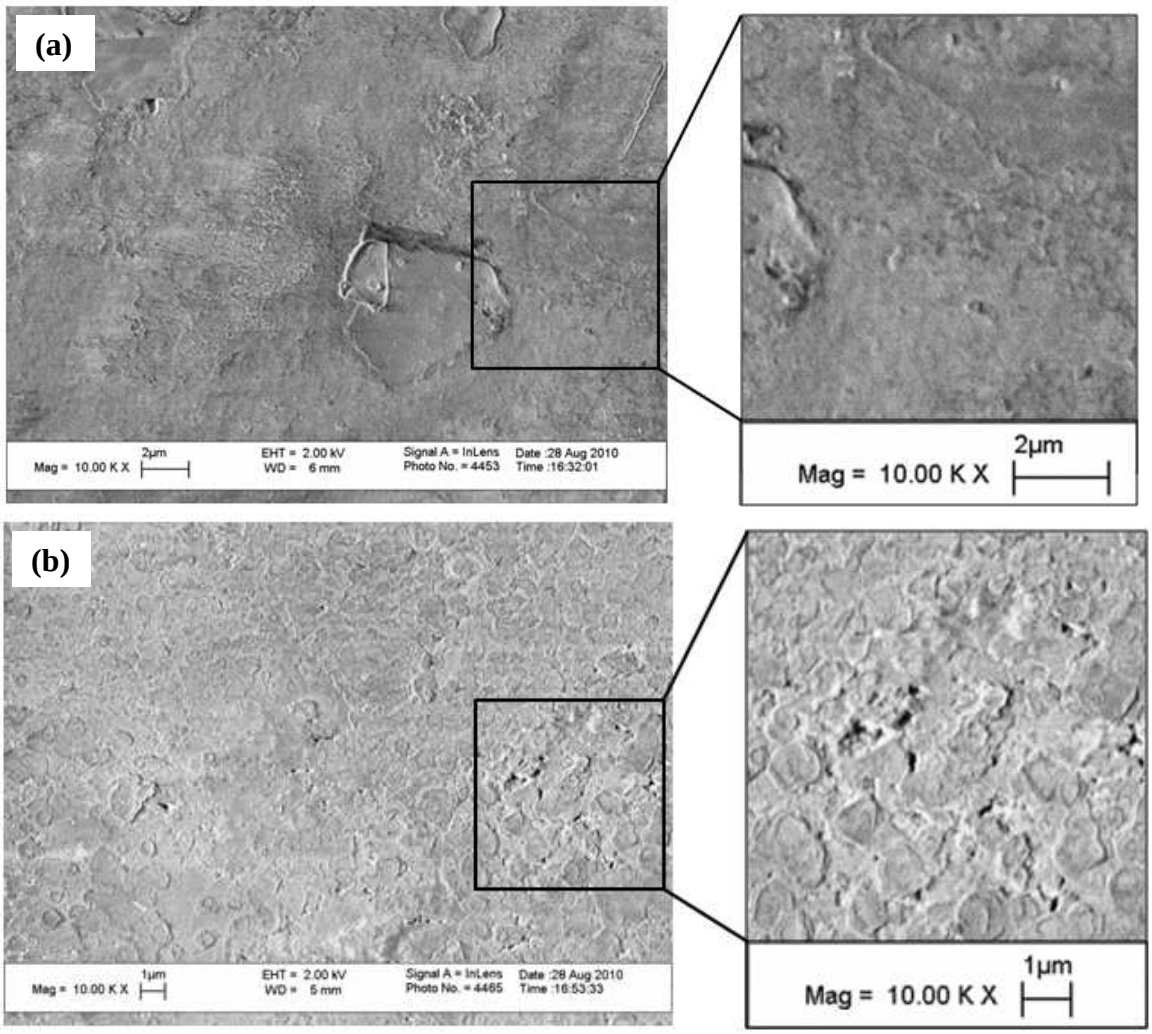

Figure 6.6—SEM image of a sample in NO experiment

(a) before exposure, (b) after 20 cycles of exposure

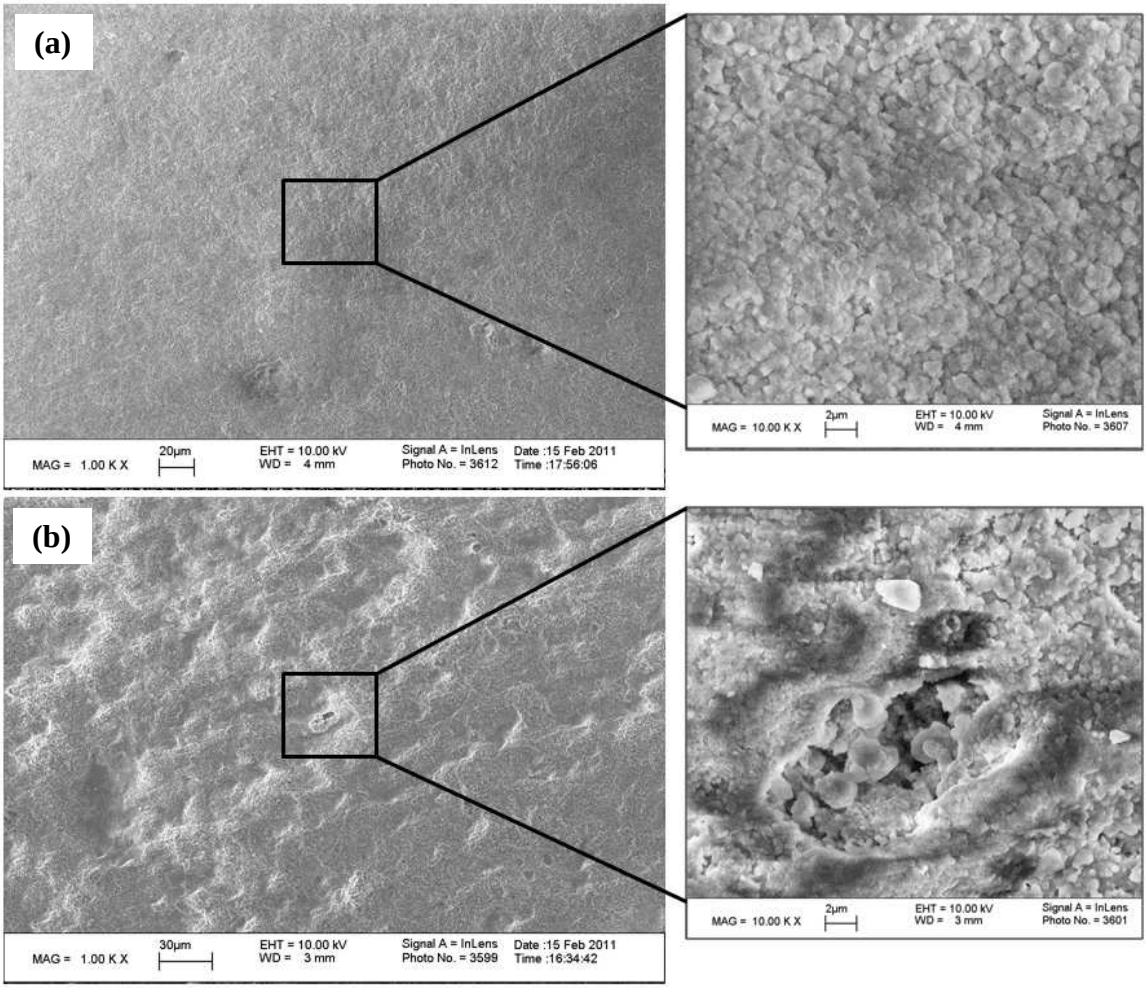

Figure 6.7—SEM image of a sample in NO_2 experiment

(a) before exposure, (b) after 12 cycles of exposure

6.3.3 Microhardness

Surface microhardness was measured by Vickers indentation method on samples periodically after every 5 and 4 cycles for the NO and NO_2 experiments respectively. As shown in Figure 6.8, at 0 cycles when the samples were not exposed to any environmental conditions, the microhardness was measured to be 45 and 38 for the samples to be exposed to NO and NO_2 respectively. This difference in the initial values

for the samples is primarily due to lower water-to-cement ratio used and lesser amount of TiO_2 replacement thus higher amount of cement for the samples to be exposed to NO. With UV and wet-drying cycling, the samples exposed to NO gas experienced a 40% increase in hardness whereas the samples exposed to NO_2 gas did not show much change in hardness. The increasing hardness in case of the NO experiment could be explained mostly likely by continued hydration of the cement. The samples used for the NO experiment were cured for just 14 days when the experiment started, and as a result, the wetting process could have promoted further cement hydration and thus the hardness might have increased. This is shown in the x-ray diffraction results section in more detail (6.3.5), where the amounts of C_3S and C_2S decreased after cycling. Compared to that, the samples used for the NO_2 experiment were cured for 28 days, resulting a more complete hydration, and thus the effect of continued cement hydration could be minimized.

While the NO_2-exposed samples appear to maintain a consistent hardness over the period of wetting/drying and NOx-UV exposure, single factor analysis of variance test (ANOVA) was performed on the NO_2 data to determine if the values measured were in fact the same, from a statistical perspective. With the significance level set to 5%, the average measured microhardness at 0^{th}, 4^{th}, 8^{th}, and 12^{th} cycles were compared. The P values were calculated to be 0.08, 0.15, and 0.03 between 0^{th}-4^{th}, 4^{th}-8^{th}, and 8^{th}-12^{th} cycle, implying that microhardness between 0^{th}-4^{th} and 4^{th}-8^{th} cycle are the same, while that of 8^{th}-12^{th} cycle is different. However, the P value calculated between 4^{th} and 12^{th} cycle was 0.43, suggesting that the microhardness measured at 4^{th} and 12^{th} cycle are the same. Thus, it can be concluded that the hardness of samples is constant during the cycling of NO_2 experiment and the lower hardness measured at 8^{th} cycle could be understood as an

experimental error. Higher water to cement ratio and longer curing time of the samples utilized in NO_2 experiment could have contributed to higher degree of hydration at the time of the experiment, thus not much hardness increase thereafter.

Overall in both cases, not a clear sign of decrease in hardness was observed. Thus it is suggested that the effect of acid attack and salt crystallization, if any, do not have a noticeable effect on microhardness of a cementitious materials.

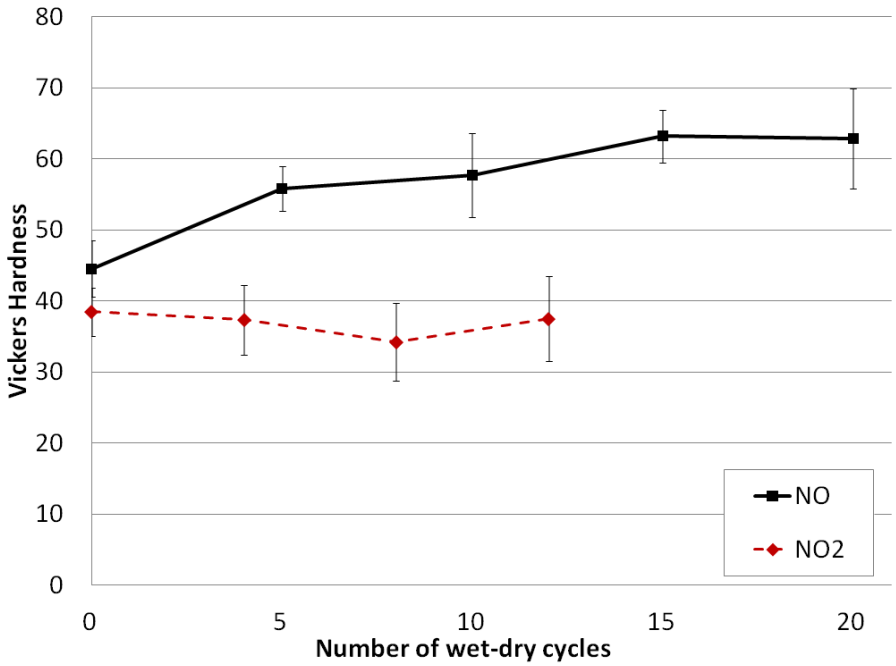

Figure 6.8—Vickers hardness of samples exposed to NO or NO_2 and wet-dry cycling

6.3.4 Surface Roughness

Surface roughness of samples after every 5 and 4 cycles for the NO and NO_2 experiments was examined to measured any changes due to leaching, acid attack or salt crystallization. The results are shown in Figure 6.9 for both of the NO and the NO_2 cases. Overall, the surface roughness of samples was constant over the period examined for both

sets of samples. In case of the NO experiment, a slight increase in roughness was observed between 0^{th} and 5^{th} cycle. This is believed to be due to excessive polishing that made the surface easily affected by, such as, continued hydration. However, roughness remained constant at ~11 after the 5^{th} cycle up to 20^{th} cycle. In case of the NO_2 experiment, the surface roughness was steady at ~13.5 for all cycles tested. The reason for the higher surface roughness in case of the NO_2 experiment could be due to coarser polishing. From both cases, the consistent roughness suggests that no considerable deterioration or build up was developed on surface of the samples during the scope of these experiments.

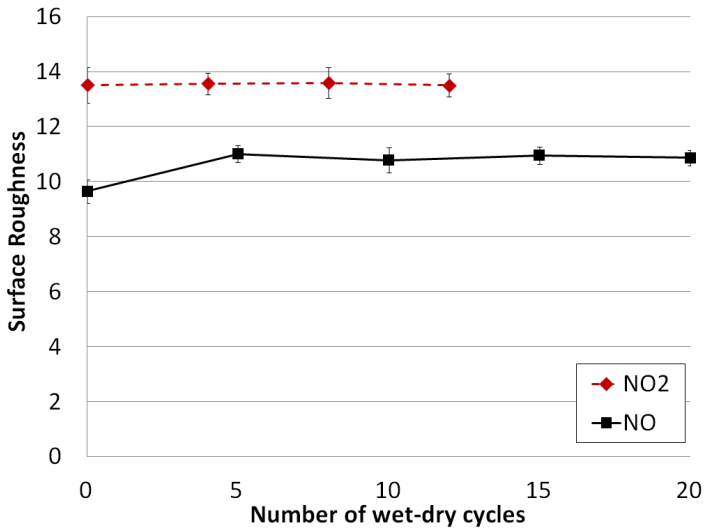

Figure 6.9—Surface roughness of samples exposed to NO or NO_2 and wet-dry cycling

6.3.5 X-ray Diffraction Analysis

After every 5 and 4 cycles for the NO and NO_2 experiments respectively, ~1mm of surface material was obtained from the sample and analyzed using x-ray diffraction.

Diffraction patterns were normalized by maximum peak of the anatase, because it is chemically inert and constant among samples of each type. The diffraction patterns are shown in Figures 6.10 (a) and (b) for the NO and NO_2 cases respectively.

Interestingly, neither $Ca(NO_3)_2$ nor $Ca(NO_2)_2$ salts of various forms of hydrates were detected using this technique. This could be understood in several circumstances. The amount of salts produced might be so little to be detected by this technique, or the salts might have transported into deeper pore structure during multiple wet-dry cycling. Other explanation could be that the nitrates and nitrites might have formed other types of salts or chemically bound in cement. Recently, Balonis et al. suggested that cement has the capability to bind nitrates and nitrites by substituting hydroxide, sulfate and carbonate from the AFm structures, forming “nitrate AFm” and “nitrite AFm” [181]. However, the main peaks of nitrate AFm at $2\theta=8.41°\text{-}10.20°$ and nitrite AFm at $2\theta=11.04°\text{-}11.23°$, as suggested by the author, were not found by this technique. It should be noted that the x-ray diffraction analysis is not capable of detecting substances that are less than 5% of the sample by volume.

It is observed, from both of the cases, that peaks of calcium carbonate ($CaCO_3$, designated with ★) increased as the number of wet-dry cycles increased. This is an indication of carbonation, which occurs to cementitious materials when exposed to atmospheric carbon dioxide (CO_2) and moisture, as previously stated in Chapter 2. The carbonation alters chemical composition of the paste which in turn may affect its porosity and microstructure. These changes can affect photocatalytic reactivity since carbonation also occurs on surface of a material. It has been experimentally determined that cement carbonation decreases the rate of photocatalytic oxidation [42, 120]. Lackoff et al.

examined the influence of carbonation on the degradation rate of atrazine, one of the organic compounds, and found reduction of photocatalytic activity possibly due to decreased specific surface area, decreased atrazine sorptivity, and calcite overgrowth on the cement surface [120]. Chen et al. also found reduced photocatalytic efficiency of NOx degradation after surface carbonation, possibly due to $CaCO_3$ deposition in pores and thus reducing total porosity [42]. This can also be the case in these experiments that the increased $CaCO_3$ affected the photocatalytic efficiency. The calcite could have filled the pores near the surface, perhaps contributing to increased hardness in the NO-exposed samples. The calcite growth might have covered the TiO_2 nanoparticles, hindering the photocatalytic oxidation reaction.

In case of the NO experiment, decreased amount of C_3S and C_2S is observed as more cycling was performed. It suggests that the unhydrated cement components were hydrated, producing C-S-H (which is largely amorphous) during the experiment, which in turn contributes to strength and hardness. This supports the microhardness data where the sample hardness was increased as more cycling was performed. On the other hand, not much C_3S or C_2S were found in the samples that are run in the NO_2 experiment, indicating that higher degree of hydration was reached before starting of the experiment and that hardness was not much affected (Figure 6.8). Also, it should be noted that the calcium hydroxide (CH) amount was decreased as more cycling was performed, in case of the NO_2 experiment. It can be understood that the CH might have been transformed to $CaCO_3$ during the carbonation process, or attacked by nitric acid. In case of the NO experiment, not much CH was found from the start of the experiment.

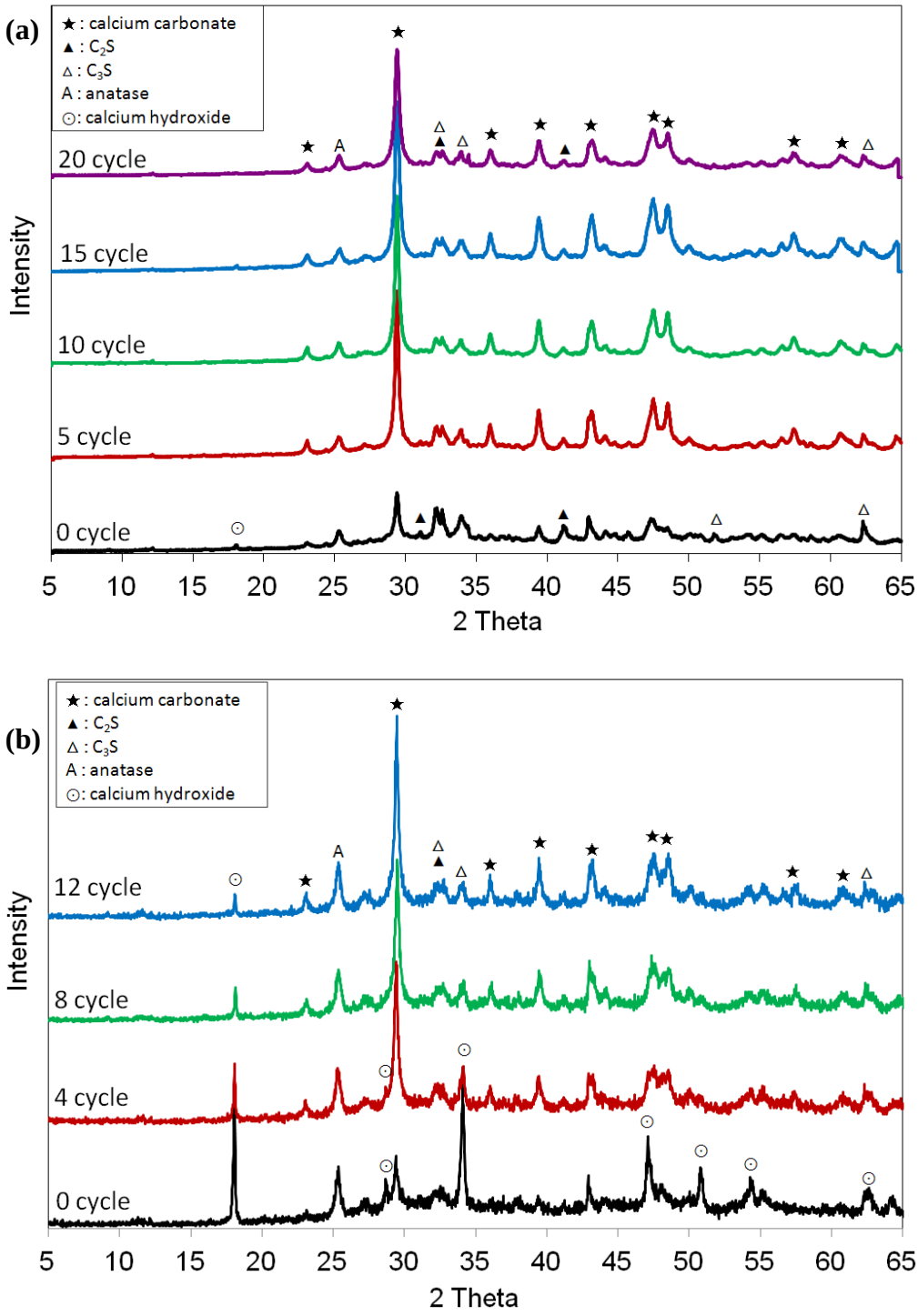

Figure 6.10—X-ray diffraction pattern of samples exposed to NOx wet-dry cycling

(a) NO experiment (b) NO_2 experiment

★: calcium carbonate, ⊙: calcium hydroxide, ▲: C_2S, △: C_3S, A: anatase

6.3.6 Mass Changes

Mass of three samples for each of the experiment was measured throughout the experiment in their dry state and averaged. The results are shown in Figure 6.11. It was observed that there is not a significant mass changes of the samples for either the NO and NO_2 experiments.

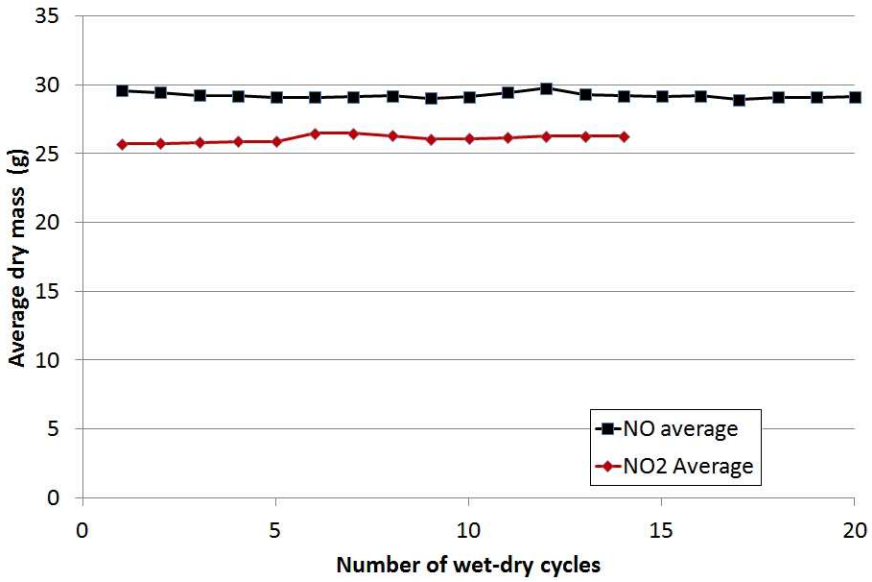

Figure 6.11—Mass changes of samples exposed to NO or NO_2 and wet-dry cycling

6.4 Conclusions

The durability and efficiency of photocatalytic cement, that might have gone through acid attack, salt crystallization, leaching, and carbonation by exposure to cycles of NOx-UV and wet-dry conditions, was experimentally investigated. Based on the results of this study, the following conclusions are drawn:

- Both NO and NO_2 gases were efficiently oxidized by the UV irradiation in the early exposure. However, with continued exposure to NOx and wet-dry cycling, the rate of photocatalytic oxidation decreased in both cases. This is thought to be a result of carbonation and continued hydration of C_3S and C_2S. It is believed that calcium carbonate and hydrated cement phases cover the TiO_2 particles in cement paste samples, thus hindering the photocatalytic reactions.
- The SEM results demonstrate that the sample surfaces were chemically deteriorated from both the NO and NO_2 experiments as evidenced by pits found from the sample surfaces. Larger and deeper pits were found from the NO_2 exposed samples, indicating that either the samples were weaker, were exposed to a harsher environmental condition, or both. The pits could possibly indicate that there was acid attack or leaching during the repeated NOx-wet-dry cycling. It suggests that the environmental condition used for this study could initiate degradation of cementitious materials and could further affect long term durability.
- The microhardness values increased in case of the NO experiment, and remained the same in case of the NO_2 experiment with the cycling, indicating that the NOx-wet-dry cycling did not decrease the hardness property of cement pastes. Rather, the hardness of the samples increased in case of the NO experiment, possibly due to continued hydration of cement and carbonation. The possible acid attack, as found from the SEM, or the salt crystallization was not able to be found by this technique.
- The surface roughness examined by confocal microscopy did not change throughout the experiments. The rougher surface as seen from the SEM could not

be quantitatively measured using confocal microscopy, likely due to the lower resolution of this instrument.

- The x-ray diffraction patterns indicate that formation of calcium carbonate was the most pronounced from both of the NO and NO_2 experiments. In case of the NO experiment, the amount of unhydrated C_3S and C_2S were decreased after cycling, meaning they were hydrated during the cycling. These results support results from microhardness. Any possible nitrate and nitrite salts were not detected using XRD, possibly because the amount produced was very little or those produced might have transported to inner pore structure.

6.5 References

42. Chen, J. and C.S. Poon, *Photocatalytic cementitious materials: Influence of the microstructure of cement paste on photocatalytic pollution degradation.* Environmental Science & Technology, 2009. **43**(23): p. 8948-8952.

70. Ohko, Y., et al., *Photocatalytic oxidation of nitrogen dioxide with TiO_2 thin films under continuous UV-light illumination.* Journal of Physical Chemistry C, 2008. **112**(28): p. 10502-10508.

98. JIS, *Fine ceramics (advanced ceramics, advanced technical ceramics) - Test method for air purification performance of photocatalytic materials* in *Part 1: Removal of nitric oxide*2004.

99. ISO, *Fine ceramics (advanced ceramics, advanced technical ceramics) - Test method for air-purification performance of semiconducting photocatalytic materials*, in *Part 1: Removal of nitric oxide*2007.

109. Valenza, J.J. and G.W. Scherer, *A review of salt scaling: I. Phenomenology.* Cement and Concrete Research, 2007. **37**(7): p. 1007-1021.

120. Lackhoff, M., et al., *Photocatalytic activity of semiconductor-modified cement-influence of semiconductor type and cement ageing.* Applied Catalysis B-Environmental, 2003. **43**(3): p. 205-216.

130. Igarashi, S., A. Bentur, and S. Mindess, *Microhardness testing of cementitious materials.* Advanced Cement Based Materials, 1996. **4**(2): p. 48-57.

131. Trtik, P. and P.J.M. Bartos, *Micromechanical properties of cementitious composites.* Materials and Structures, 1999. **32**(219): p. 388-393.

132. Cross, W.M., et al., *Microhardness testing of fiber-reinforced cement paste.* Aci Materials Journal, 2000. **97**(2): p. 162-167.

142. Hossain, K.M.A., *Macro- and microstructural investigations on strength and durability of pumice concrete at high temperature.* Journal of Materials in Civil Engineering, 2006. **18**(4): p. 527-536.

180. ASTM, *ASTM C 1327 Standard test method for Vickers indentation hardness of advanced ceramics*, 2008.

181. Balonis, M., M. Medala, and F.P. Glasser, *Influence of calcium nitrate and nitrite on the constitution of AFm and AFt cement hydrates*. Vol. 23. 2011, London, ROYAUME-UNI: Telford. 15.

CHAPTER 7

SALT CRYSTALLIZATION DAMAGE TO TIO_2 CONTAINING MORTAR BARS

7.1 Introduction

Porous, brittle materials such as stone, masonry or cement-based materials can be damaged due to crystallization pressure generated in their pores, as stated in Chapter 2. When salts are the cause of damage, this phenomenon is called “salt weathering”, “salt scaling” or, particularly when referring to crystallization of sulfate salts, “physical salt attack” [145]. In Chapter 6, it was suggested that cyclic exposure to NOx and wet-drying have a potential to damage the surface of a cementitious materials in the long term. However, the extent of the damage was not sufficient to be measured quantitatively. Since it is reported that the nitrates could participate in salt crystallization damage of porous materials (Chapter 2), a detailed examination is needed of the potential for salt crystallization damage to cementitious materials from nitrate salts which form within their structure.

The objective of this research, then, was to examine specifically the effect of calcium nitrate salts on cementitious materials and to determine if exposure to them has a potential to generate expansive cracking in mortars. To examine the influence of microstructure (e.g., porosity, pore size), the water-to-binder ratio and rate of addition of TiO_2 nanoparticles were varied. Two different concentrations of calcium nitrate solutions

were utilized and compared with the more commonly examined sodium sulfate solution as well as samples exposed to deionized water.

7.2 Theoretical Background

The mechanism of damage to porous materials by crystallization pressure proposed by Scherer [105] is the most widely accepted and has been extended to assess damage to porous, brittle materials by ice formation, as well as various forms of salt crystallization (e.g., sulfate attack, delayed ettringite formation). The theory considers the pressure exerted by a crystallizing salt and examines conditions which can induce cracking of porous materials such as cement and concrete. The extent of damage depends on the supersaturation of the salt, the size of the pores, and a disjoining pressure between the growing crystal and pore wall [105]. One of the common conditions for the supersaturation is the evaporation of liquid, which increases salt concentration in a solution.

Among the three cases where the crystallization pressure affects a material (see Chapter 2), according to Scherer [105], the case of "capillary rise and evaporation" is going to be experimentally examined in this chapter. When a porous material, such as cement or concrete, is in contact with a solution, the solution is drawn into the pores of a material by capillary suction. The flux, as a result of capillary pressure, can be written as Equation (7.1), which is derived from Darcy's law.

$$Jc = \phi \bar{A} \frac{dh}{dt} = \frac{k}{\eta} \frac{(-p_c - \rho_L g h)}{h} \qquad (7.1)$$

Here, J_c is the flux from the capillary rise, ϕ is the porosity of a material, $\bar{A}$ is the area of the surface in contact with the ground, k is the permeability, η is the viscosity, p_c is capillary pressure, ρ_L is the density of the liquid, g is the gravitational acceleration, and h is the height that the liquid has risen to. Note here that the flux, or rate of rise, decreases as h increases. On the other hand, the rate of evaporation from the surface of a material, J_E, is constant. This makes an equilibrium height, h_s, where the rate of capillary rise and drying are equal. As the water evaporates, the concentration of salt increases near the surface of a material. Near the region of contact, the concentration gradient is not large enough to lead to supersaturation because the salt diffuses back towards the source. This causes the lower part of a structure to remain relatively wet under these exposure conditions. Above this region, salt concentration at the drying surface increases, ultimately reaching supersaturation. At this level, salt precipitates out on the surface of a material, a process which is called "efflorescence". Above, near h_s, the rate of evaporation exceeds the rate of capillary rise, which results in salt crystallization within the pores of the material. It is in this "subflorescence" region, where damage may occur when the crystallization pressure exceeds tensile strength of a material. Because drying happens on the surfaces, the damage tends to produce a conical shape for a prismatic sample. The schematic of capillary rise and evaporation is shown in Figure 7.1 (reproduced from Scherer [105]).

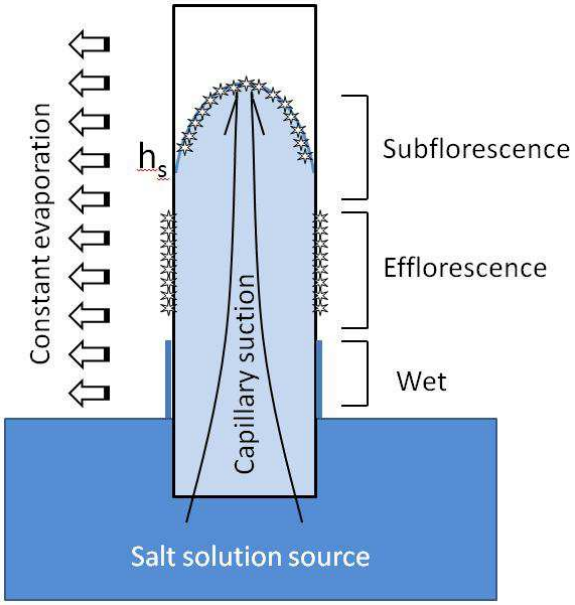

Figure 7.1—Schematic of capillary rise and evaporation

7.3 Experimental Procedure

7.3.1 Materials and Sample Preparation

Mortar bar samples containing TiO_2 nanoparticles were prepared for this study. The cement used was ASTM C 150 Type I portland cement. The TiO_2 powder used for this study was P25 (Aeroxide TiO_2 P25, Evonik Industries), which consisted of 80% anatase and 20% rutile. The average crystal size is 21nm, the surface area is 50±15 m^2/g, and the sample purity is 99.5% as stated by the manufacturer. Standard 20-30 Ottawa sand was used that conforms to ASTM C778. Mortar bars were made based on a cement-aggregate mass ratio of 1:2.23. For the samples with 0% and 5% TiO_2 replacement by mass of cement, mortars were prepared with water-to-binder ratios (w/b) of 0.40, 0.50, and 0.60, where the TiO_2 powder was considered as binder. For 10% and 15% TiO_2 containing samples, only the case of w/b of 0.50 was considered, giving a single w/b

with all four TiO_2 addition rates (0%, 5%, 10%, and 15%), while also examining the influence of varying w/b at a range of 0.40, 0.50, and 0.60 at lower TiO_2 addition rates (0% and 5%).

When mixing the mortar, the TiO_2 powder was first mixed with deionized water for 1 minute in a planetary mixer to better disperse the particles. The remainder of the mortar mixing followed ASTM C305 procedures.

Mortar bars were cast in 1 x 1 x 10 inch steel molds. The molds were coated with thin layer of hydraulic oil prior to casting. After curing in 100% RH for 24 hours at 23±2°C, the specimens were removed from molds and continued to be cured in limewater until 7 days of age at room temperature (23±2°C). Samples were removed from limewater and cut into approximately 9cm bars with wet saw and dried in normal room condition for 3 days (23±2°C) . Note that both ends of mortar bars were also cut to make sure all specimen ends have same absorptive capacity

7.3.2 Procedure: Salt Solution Exposure Conditions

The salt crystallization exposure uses salt solutions of calcium nitrate and sodium sulfate. Deionized water with 18.2MΩ resistivity was used as a control. Calcium nitrate tetrahydrate ($Ca(NO_3)_2 \cdot 4H_2O$, BDH, 99.0% purity) solution was prepared at 15% and 30% by mass, and sodium sulfate decahydrate ($Na_2SO_4 \cdot 10H_2O$, Fisher Scientific, 99.0% purity) solution was prepared at 15% by mass. The experimental plan is summarized in Table 7.1.

Table 7.1 Experimental detail

	0% TiO_2	5% TiO_2 sample				10% TiO_2	15% TiO_2
	$Ca(NO_3)_2$ 15%	$Ca(NO_3)_2$ 15%	$Ca(NO_3)_2$ 30%	Na_2SO_4 15%	Deionized water	$Ca(NO_3)_2$ 15%	$Ca(NO_3)_2$ 15%
0.4		O	O	O	O		
0.5	O	O	O	O	O	O	O
0.6		O	O	O	O		

The experimental procedure was based upon that described by Scherer [105]. A glass-sided chamber was fabricated such that it provides constant relative humidity conditions inside. To control the humidity inside the chamber, a saturated solution of calcium chloride ($CaCl_2$) was used [182], and relative humidity was maintained at 35±3% at room temperature (23±2°C) throughout the experiment. $CaCl_2$ was frequently added to keep the solution saturated and magnetic stirrer was used to keep the concentration constant among the solution. Mortar bar samples were suspended from the top, such that lower portion of the samples were partially immersed (to a height of ~2cm) in each test solution. By this partial immersion, the salt solutions were absorbed into the mortar bar samples from the bottom region and evaporated at upper surfaces of the samples. In order to minimize evaporation from the test solutions and maintain low RH in the chamber, each test solution was prepared in closed containers with holes where the mortar bars pass through (Figure 7.2). To maintain constant height of test solutions in each container, test solutions were connected with back-up solutions outside of the chamber with tubing. A diagram of the test setup is presented in Figure 7.3 and picture of the actual experimental setup is presented in Figure 7.4.

Figure 7.2—Mortar bars partially immersed in test solution

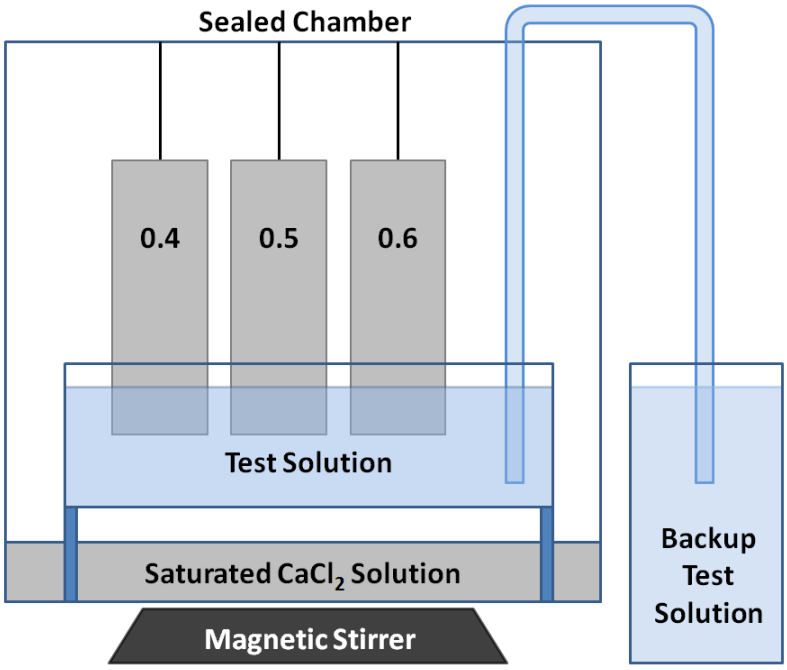

Figure 7.3—Schematic diagram of the experimental setup

Figure 7.4—Picture of the experimental setup

7.4 Results and Discussion

7.4.1 Effect of Different Salt Solutions and Varying Water-to-Binder Ratio

Samples with 5% TiO_2 replacement, partially immersed in 15% $Ca(NO_3)_2$ solution, 30% $Ca(NO_3)_2$ solution, 15% Na_2SO_4 solution, and deionized water for 65 days, were inspected visually with the unaided eye and with a stereomicroscope (Leica MZ6) at 12.6-20X magnification. The visual inspection results are presented in Figure 7.5, 7.6, 7.7, and 7.8 for the 15% $Ca(NO_3)_2$, 30% $Ca(NO_3)_2$, 15% Na_2SO_4, and deionized water, respectively for w/b=0.40, 0.50, and 0.60 samples.

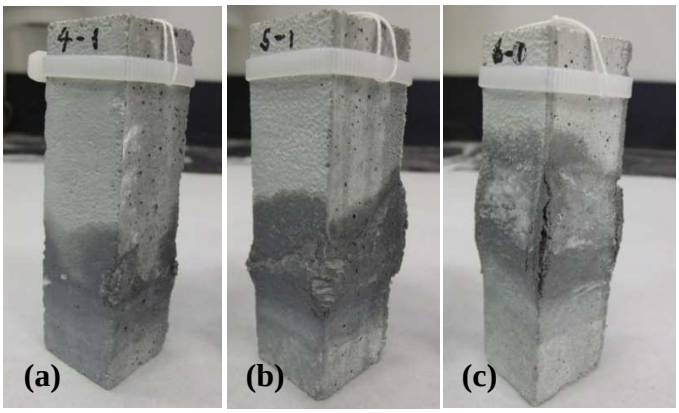

Figure 7.5 — Samples partially immersed in 15% $Ca(NO_3)_2$ solution

(a) w/b=0.40, (b) w/b=0.50, and (c) w/b=0.60

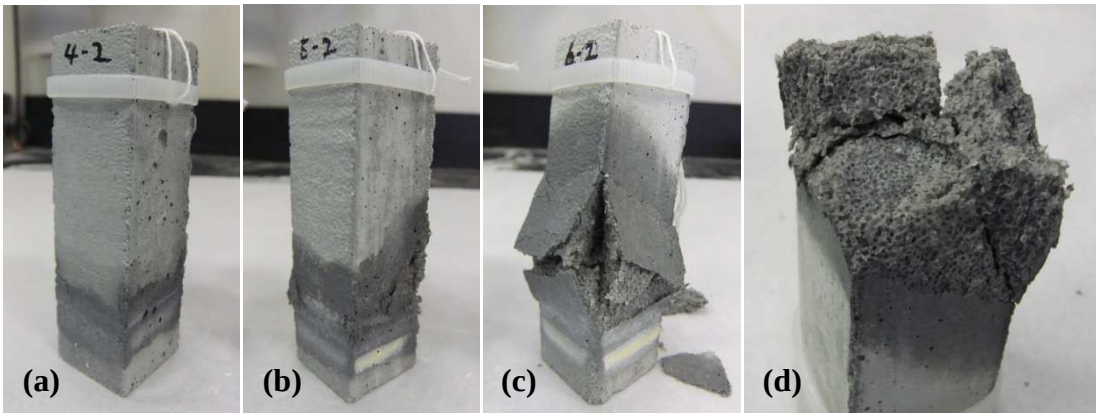

Figure 7.6—Samples partially immersed in 30% $Ca(NO_3)_2$ solution

(a) w/b=0.40, (b) w/b=0.50, (c) w/b=0.60, and (d) crack detail of w/b=0.6 sample

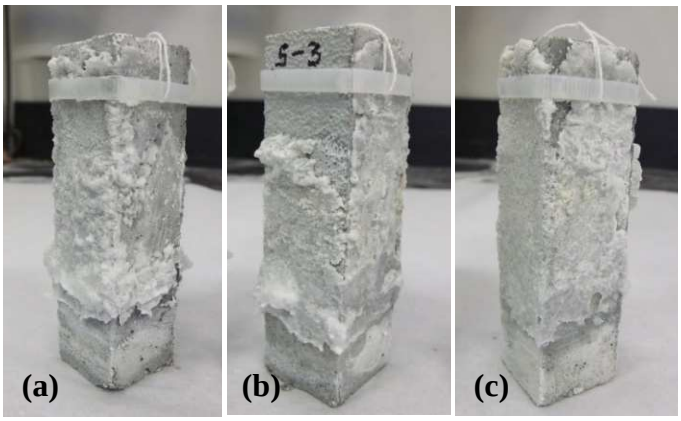

Figure 7.7—Samples partially immersed in 15% Na_2SO_4 solution

(a) w/b=0.40, (b) w/b=0.50, and (c) w/b=0.60

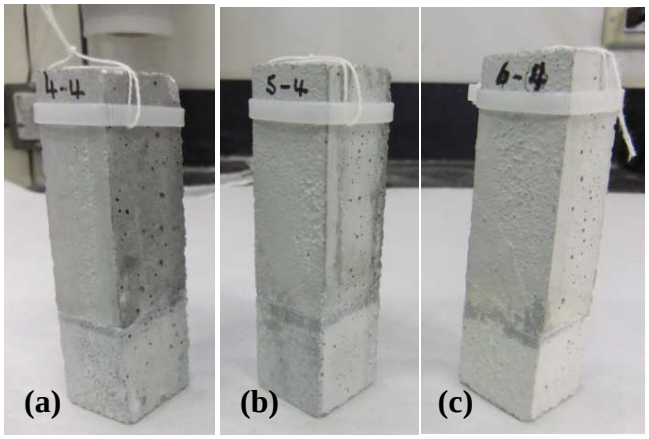

Figure 7.8—Samples partially immersed in deionized water

(a) w/b=0.40, (b) w/b=0.50, and (c) w/b=0.60

Overall, the samples partially immersed in $Ca(NO_3)_2$ solution experienced cracking and spalling, the samples in Na_2SO_4 solution showed heavy efflorescence outside the samples but no damage on the samples was found, and the control samples in water were found to be sound after 65 days exposure. From Figures 7.5 and 7.6, it was

determined that $Ca(NO_3)_2$ solution could induce expansive cracking on cementitious materials that could lead to complete destruction.

Among the three water-to-binder ratios examined, the mortars prepared at w/b=0.60 subjected to either 15% or 30% $Ca(NO_3)_2$ solutions (Figure 7.5 (c) and 7.6 (c)) exhibited the most severe cracking, which was characterized by spalling of outer layer of mortar samples. Over time, cracking, which started from each corner where drying rate is relatively faster, propagated to the sample faces, eventually achieving a crack width of ~2-3mm. Especially, the sample in 30% solution was completely broken in half, indicating that salt crystallization damage affected the entire cross-section of the sample. Major cracking initiated from each corner, forming a conical shape towards the inner structure (Figure 7.6 (d)). Compared to the w/b=0.60 mortar, the w/b=0.50 mortar was damaged in a lesser degree in both of the $Ca(NO_3)_2$ solutions and the w/b=0.40 mortar experienced only subtle damage on the corner of the samples in both solutions.

The different behavior between different w/b samples is believed to be highly related to variations in strengths of the samples. Cracking occurs when the salt crystallization pressure exceeds tensile strength of a material [109]. Valenza [109] noted that as the compressive strength approaches a value of 40 MPa, the salt scaling resistance of the material should be satisfactory. This suggests that salt crystallization damage can be mitigated by lowering w/b, as w/b is conventionally inversely related to compressive strength. Compressive strengths of cement pastes with w/b from 0.40 to 0.60 are shown in Chapter 3 in Figure 3.6, where all the cases exceed the limit value of 40 MPa which is ~5800 psi. However, it is expected that the compressive strength of mortars, as utilized in this study, would be lower than the cement pastes utilized in Chapter 3. It is likely that

the compressive strength would be lower than the 40MPa at higher w/b, leading to salt crystallization damage.

It should be also noted that the location where cracking occurs varies with w/b, with cracks forming at greater heights above the solution surface as the w/b increases. This is believed to be related to the influence that w/b has on the pore structure in the samples. The capillary flux increases proportionally as porosity increases (Equation 8.3). With high w/b producing a greater porosity, thus, the salt solution would be transported higher within the high w/b sample. This would result in subflorescence at greater height above the solution than for lower w/b samples. Visually, the location of drying front, characterized by darker color within each sample, was observed at higher location for the higher w/b samples.

Comparing samples in 15% and 30% calcium nitrate solutions, samples subjected to 30% solution experienced more severe damage than the ones in 15% solution as expected. This indicates that higher concentration of salt solution resulted in more severe damage at early times.

The samples immersed in Na_2SO_4 solution developed heavy efflorescence within several days after the start of the experiment, with white deposits covering whole sample surfaces. The thickness of the deposit continued to increase with time reaching ~2-5mm at some areas, but no difference was observed with varying w/b. However, no cracking was observed on the sample surfaces. Typically, efflorescence takes place when solution dries outside of a sample. This negatively impacts the aesthetics of a structure, but does not affect its soundness. While the more damaging subflorescence occurs at above the

efflorescence, the mortar bars were apparently not of ample height to support that mode of deposition.

The sodium sulfate salt precipitated on the sample surface was scraped off and examined by x-ray diffraction analysis. It was confirmed to be pure thenardite, the anhydrous form of Na_2SO_4 (Figure 7.9). Considering that the salt used for making the solution is mirabilite ($Na_2SO_4 \cdot 10H_2O$), the humidity condition in this experiment is low enough that anhydrous thenardite salt precipitates, since the phase diagram for sodium sulfate indicates that thenardite transforms to mirabilite at RH=~78% at 25°C (Figure 7.10). Although the damage mechanism due to sodium sulfate remains controversial, it is believed that thenardite dissolution generates high supersaturations with respect to mirabilite, and that crystallization stress of mirabilite growth induces damage [107]. In the experiment, mirabilite solution dried out into anhydrous thenardite, the opposite direction of generating disruptive crystallization damage. This suggests that the mortars in sodium sulfate solution in this experiment are not conditioned under the worst case scenario damage. However, supersaturation is still expected during drying, such as calcium nitrate solution cases, leading to salt crystallization stress.

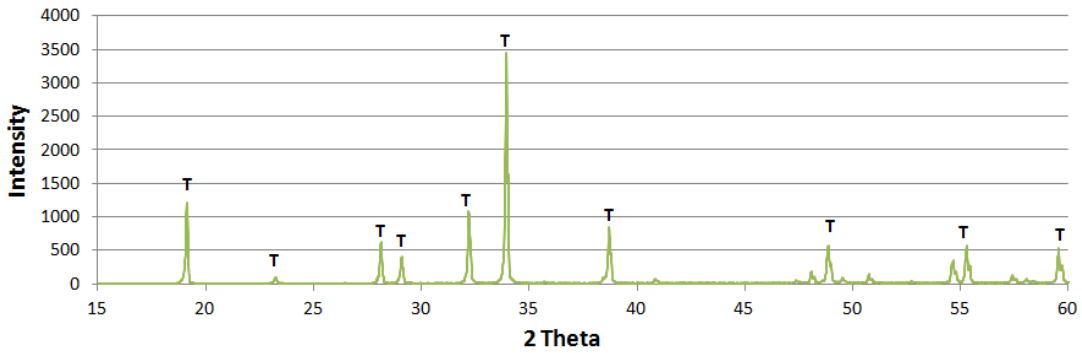

Figure 7.9 – X-ray diffraction pattern of salt outside of w/b=0.60 sample immersed in 15% Na_2SO_4 solution. "T" designates Thenardite, anhydrous form of Na_2SO_4.

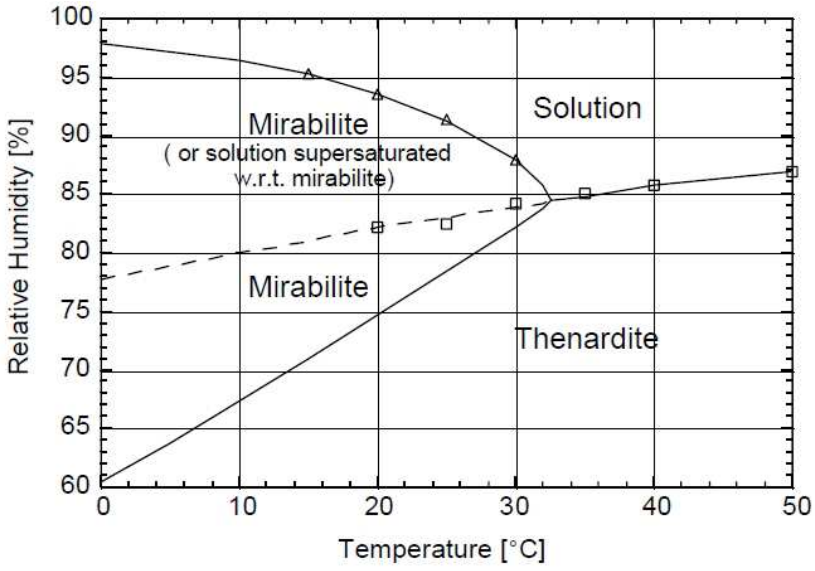

Figure 7.10 – Phase diagram for sodium sulfate (from [107])

In addition to visual inspection, samples immersed in calcium nitrate solution (15% and 30%) that went through damage were examined by optical microscopy at 65 days. Damaged parts were chosen for examination and the results from these observations are shown in Table 7.2. In all of the samples, needle-like structures along with glassy amorphous-appearing deposits were observed within cracks. The amorphous deposits

covered the inside of cracks on cement pastes and sand particles. The needle-like crystallized salts were developed inside of the cracks on the amorphous deposits. The w/c=0.5 samples had the most amorphous deposits possibly because they had the longest time out from the controlled chamber. It is hypothesized that the crystallized salts absorb moisture from the atmosphere and are dissolved, then dry again forming amorphous morphology. To identify the composition of any crystalline precipitates, additional powder x-ray diffraction analysis was performed. The w/b=0.6 sample immersed in 30% $Ca(NO_3)_2$ solution was chosen for this purpose because it experienced the most damage and thus was anticipated to have the most amount of salt formed. The damaged part was carefully collected and crushed. During this step, sand particles were removed using No.50 sieve (0.297mm opening). Using mortar and pestle, the powder was ground and was run under CuKα radiation for 2 hours. A control sample from the same batch but not used for the experiment, was also prepared in a same way. As shown in Figure 7.11, calcium nitrate hydrate was identified in two forms - $Ca(NO_3)_2{\cdot}2H_2O$ and $Ca(NO_3)_2{\cdot}4H_2O$. In addition, another nitrate compound, $Ca(OH)NO_3(H_2O)$ was also found, suggesting chemical reactions between the salt from the solution with the cementitious materials. It is notable that calcium hydroxide (OH), a major crystalline phase in cementitious materials, was not found in deteriorated portion of the sample. This suggest that the calcium hydroxide could potentially react with the calcium nitrate salt, leading to the formation $Ca(OH)NO_3(H_2O)$.

Table 7.2 Damaged surfaces of samples immersed in $Ca(NO_3)_2$ solution

	15% $Ca(NO_3)_2$ solution	30% $Ca(NO_3)_2$ solution
w/b=0.4		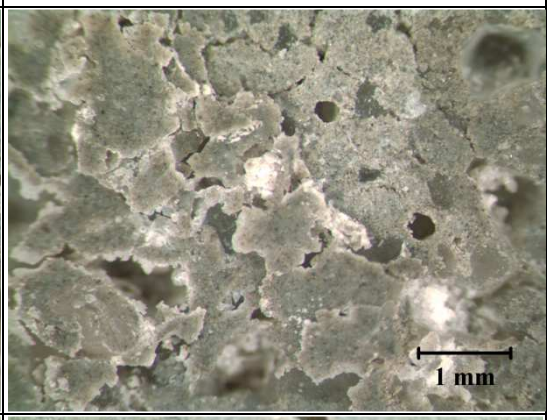
w/b=0.5		
w/b=0.6		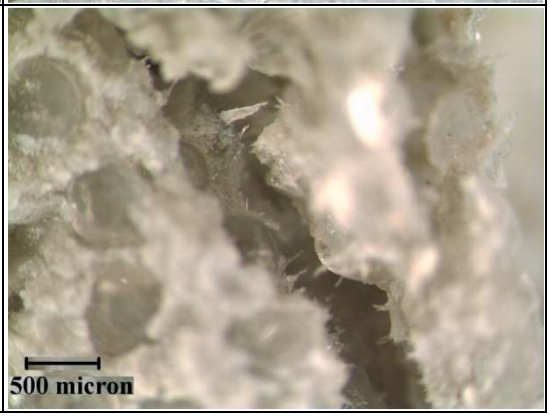

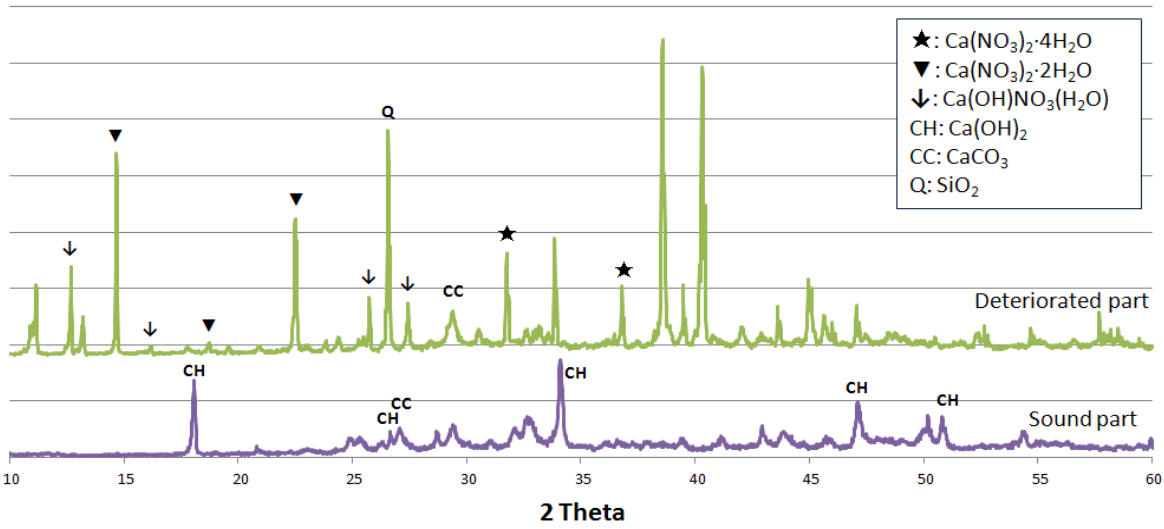

Figure 7.11 – Diffraction pattern of w/b=0.60 sample immersed in 30% $Ca(NO_3)_2$ solution. The top and the bottom represent deteriorated part and unaffected part, respectively.

7.4.2 Effect of Different Amounts of TiO_2

A similar salt crystallization experiment was performed with samples prepared with different amounts of TiO_2 powder in order to examine the effect of addition of inert nanoparticles. Some of the effects of addition of TiO_2 nanoparticles were addressed in Chapter 3 and 4 already. In Chapter 4, the effect of TiO_2 was examined on early hydration of cement, where the nanoparticles promote cement hydration due to nucleation effect. This could possibly alter the microstructure of cementitious materials, which would affect transport properties and thus long-term durability as well. In Chapter 3, it was found that the compressive strength slightly decreased in case of the w/c=0.5 samples with TiO_2 addition, and it is known that compressive strength plays a critical role

in salt crystallization damage. Thus, this subsection focuses on the effect of varying TiO_2 dosing rates, especially on the salt crystallization damage.

Mortar bar samples with water-to-binder ratio of 0.50 and containing 0%, 5%, 10%, and 15% of TiO_2 particles were partially immersed in 15% $Ca(NO_3)_2$ solution for 92 days.

Samples were inspected visually and by optical microscopy. The visual inspection results are presented in Figure 7.12 for the 0%, 5%, 10%, and 15% TiO_2 containing mortar bars. Comparing these, it was shown that the ordinary mortar exhibited the least damage, with relatively minor salt spalling at the corners (Figure 7.12 (a)). The extent of damage grows with increasing amounts of TiO_2 in the mortar, with the maximum damage in case of 15% TiO_2 (Figure 7.12 (d)). For that case, spalling, expansion, and vertical cracking were observed at the corners with expansion and scaling progressing from the corners across the sample faces.

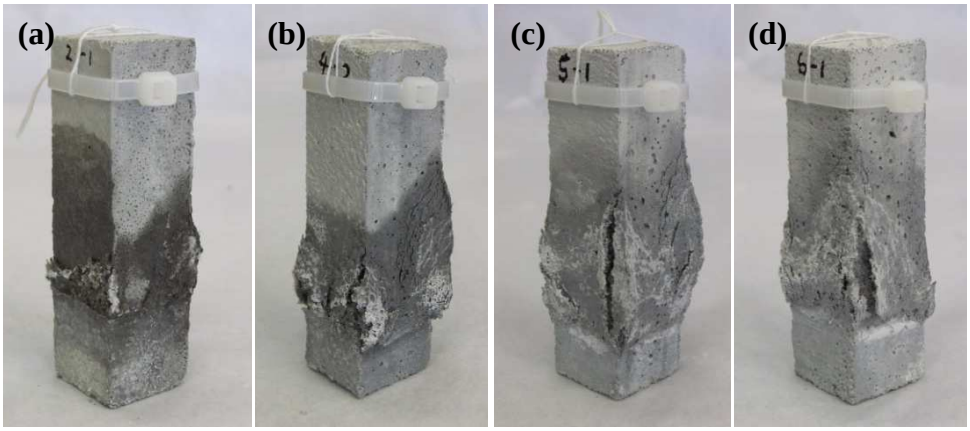

Figure 7.12— w/b=0.50 samples partially immersed in 15% $Ca(NO_3)_2$ solution

(a) 0% TiO_2, (b) 5% TiO_2, (c) 10% TiO_2, and (d) 15% TiO_2

Figure 7.13 shows at higher magnification the deteriorated parts of the samples presented in Figure 7.12. The needle-like precipitates of $Ca(NO_3)_2$ salts were observed in the cracks of all of the samples.

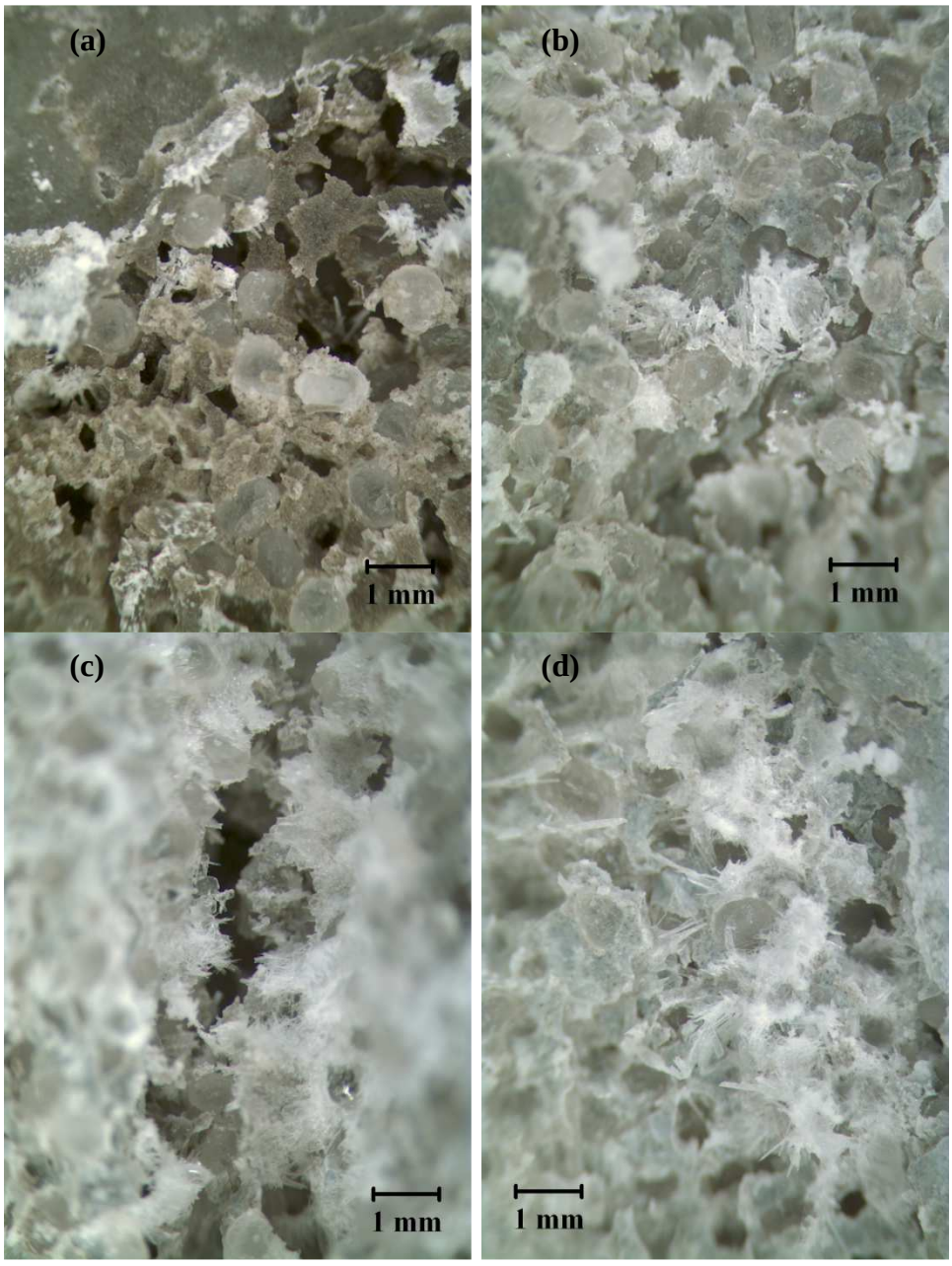

Figure 7.13— w/b=0.50 samples partially immersed in 15% $Ca(NO_3)_2$ solution (a) 0% TiO_2, (b) 5% TiO_2, (c) 10% TiO_2, and (d) 15% TiO_2

In order to investigate the possible reasons for the differences in salt scaling damage between varying TiO_2 replacement rates, a microstructural evaluation was performed. In particular, the surface area and pore size distribution of a hydrated cementitious material are closely related to microstructure development that could potentially explain variations in macroscopic properties, including salt crystallization damage. Nitrogen BET surface area and pore size distribution of the 0%, 5%, and 10% TiO_2 (P25) containing cement pastes at w/b=0.50 were measured at 7 days of curing, using a surface area and porosimetry analyzer (ASAP 2020, Micromeritics, Norcross, GA). The curing conditions and age for these paste samples were the same as the mortar bars used for this study. The samples were crushed to pass the No. 8 sieve (0.0937 in or 2.38 mm opening) and retained on a No. 16 sieve (0.0469 in or 1.19 mm opening), and were subsequently freeze dried for 3 days. The BET surface area was measured to be 50.3124 m^2/g, 66.0541 m^2/g, and 84.4845 m^2/g for the 0%, 5%, and 10% samples respectively, showing an increased surface area with higher TiO_2 replacement. The pore size distribution was calculated using the Barrett, Joyner, Hallenda (BJH) method and the cumulative pore size distribution and cumulative pore volume distribution results are shown in Figure 7.14 (a) and (b) respectively.

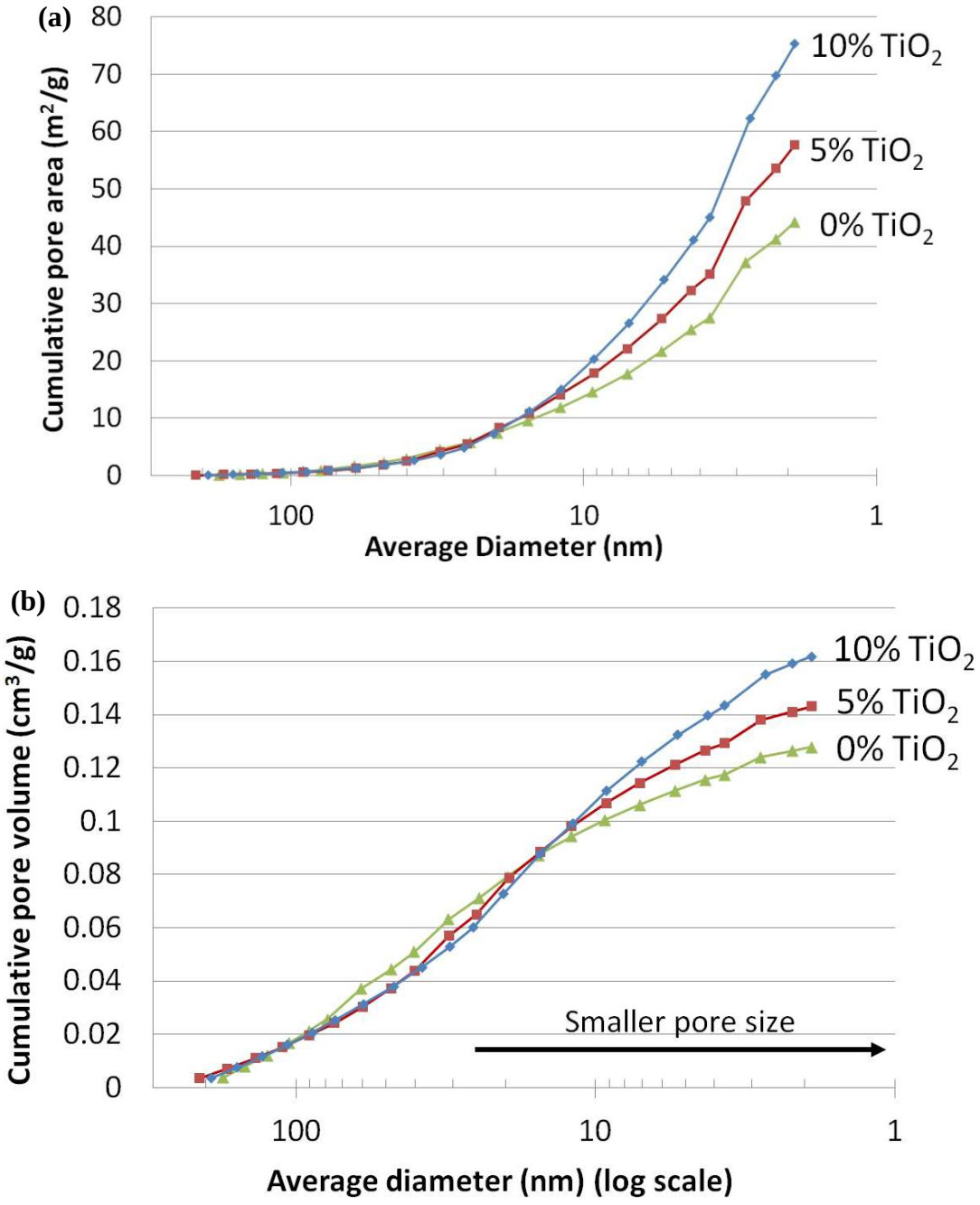

Figure 7.14—(a) Cumulative pore area distribution and (b) Cumulative pore volume distribution of w/b=0.50 paste samples at 7 days of curing at 0%, 5%, and 10% TiO_2 replacement

From these results, it was found that higher TiO_2 replacement rate resulted in greater pore area and pore volume at pores smaller than 10 nm. This suggests that the addition of high surface TiO_2 nanoparticles altered the microstructure of cement pastes despite the less cement content. These results can be related to the salt crystallization theory proposed by Scherer, where smaller pores are more susceptible to high crystallization pressure than large pores [105] as shown in Equation (2.10). Thus, these results suggest that the denser microstructure developed with high TiO_2 addition could have led to high salt crystallization damage.

7.5 Conclusions

The salt crystallization damage on mortar bar samples was experimentally investigated using calcium nitrate solution. It was determined that calcium nitrate salt could induce salt crystallization damage to cementitious materials under low RH, and that the extent of damage gets severer with higher w/b and higher TiO_2 content. Crystalline calcium nitrates and nitrate compounds were found from the cracked surface. It is suggested that w/b less than 0.4 be used for mortar that contains less than 5% of TiO_2 nanoparticles to be resistant to salt crystallization damage. Careful site investigation is necessary in planning of a structure, where the ambient RH is low and continuous supply of nitrates are anticipated.

7.6 References

105. Scherer, G.W., *Stress from crystallization of salt.* Cement and Concrete Research, 2004. **34**(9): p. 1613-1624.

107. Flatt, R.J., *Salt damage in porous materials: how high supersaturations are generated.* Journal of Crystal Growth, 2002. **242**(3-4): p. 435-454.

109. Valenza, J.J. and G.W. Scherer, *A review of salt scaling: I. Phenomenology.* Cement and Concrete Research, 2007. **37**(7): p. 1007-1021.

145. ACI, *201.2R-08: Guide to Durable Concrete*, 2008, American Concrete Institute.

182. Stokes, R.H. and R.A. Robinson, *Standard Solutions for Humidity Control at 25° C.* Industrial & Engineering Chemistry, 1949. **41**(9): p. 2013-2013.

CHAPTER 8

CONCLUSIONS AND FUTURE RESEARCH

8.1 Conclusions and Contributions of Research

Performances of photocatalytic cement-based materials ranging from early age properties to the long-term durability have been investigated in this research. In this chapter, key findings and global conclusions are presented with the contributions of this research.

Cement Hydration:

While interest in the use of titanium dioxide in construction materials is increasing due to its NOx binding capability among other functionalities, the effect of the addition of these functional nanoparticles on cement-based materials had not been previously investigated. This study examined the impact of the chemically inert TiO_2 nanoparticles on the properties of cementitious materials. An important contribution of this effort was the conclusion that the addition of TiO_2 nanoparticles increases the rate of early cement hydration and the degree of early hydration, resulting in decreased setting time and increased compressive strength at lower water-to-cement ratio, but with decreased microhardness. These series of results from Chapter 3 suggest that the TiO_2 nanoparticles could be used to optimize cementitious materials to achieve specific early age behavior as well as hardened properties, setting aside the photocatalytic benefit. In particular, this research has demonstrated that reductions in clinker content in cement or

concrete could be realized through the addition or substitution of cement with chemically inert nanoparticles, such as titania.

Boundary Nucleation:

Further, this research provided experimental evidence, coupled with modeling, that demonstrated the addition of TiO_2 nanoparticles accelerated and increased the degree of hydration of the early hydration of C_3S and C_2S, the two primary components in portland cement. With mathematical modeling, it was shown that the additional surface area of the TiO_2 nanoparticles provide nucleation sites for the hydrated cement products, thus decreasing the induction period and accelerating hydration. The boundary nucleation model was found to approximate the hydration curve more accurately than the conventionally used Avrami model due to the assumption that nucleates develop preferably on surface rather than random nucleation. In summary, the results suggest that the nanoparticles participate in the hydration process by adding huge surface area, and should not be considered just as inert "fillers."

Acceleration of Belite Reaction:

Also, importantly, the rate of hydration of the C_2S phase in portland cement was examined by isothermal calorimetry for the first time in this study. The hydration curves of C_2S pastes were successfully collected with and without TiO_2 nanoparticles, and an accelerated hydration was found with the samples containing the TiO_2 particles. This suggests that practical use of C_2S-rich cements could be promoted by optimizing the performance using nano-TiO_2 or other inert nanoparticles; currently such cements are not favored, primarily because of their slower rate of reaction. By accelerating the hydration

of C_2S – which can be produced at lower temperatures while emitting less CO_2 during manufacture – another potential pathway to sustainable development was identified.

Binding of NO and NO_2:

Most prior research has utilized NO gas while examining the photocatalytic reaction in cement-based materials, primarily due to the existing standards. However, it is the NO_2 that is directly harmful to humans that needs to be diminished, although the NO and NO_2 coexist in the atmosphere. In the current study, the photocatalytic behavior between the NO and NO_2 gases was investigated and compared. It was found that the photocatalytic efficiency between the two gases was similar after 3 hours of NOx and UV exposure. However, in both cases, the NOx binding efficiency, or the decrease in the NOx level, decreased with long-term NOx/UV and environmental exposure presumably due to carbonation and overgrowth of hydration products. In addition, the current study examined the NOx binding capability within the cementitious materials, which is qualitatively addressed for the first time. It was found that the NO_2 gas has a greater potential to be bound in hardened cement paste than the NO gas, and the amount is comparable to the amount decreased by photocatalytic reactions. These results suggest that photocatalytic cement-based materials could be used to mitigate the harmful NO_2 gas in the atmosphere not only through photocatalysis, but also through NOx binding within the cementitious matrix.

Long-term Durability:

The repeated exposure to the NOx-UV condition as well as wetting and drying was shown to result in pits on the surface of the samples as evidenced by SEM images, which is an indication of chemical damage. However, microhardness, surface roughness,

and x-ray diffraction analysis were insensitive to any resulting changes in surface properties or composition. These results suggest that NOx-wet-dry cycling has a potential to generate surface damage of a cementitious materials, but that further research is warranted to better address this problem. It is recommended that these photoctalytic cement-based materials be used in a vertical configuration such as on walls, rather than in a horizontal configuration such as pavements, so that the photocatalytic products can be washed out more efficiently and to decrease chance of abrasion.

Salt Crystallization:

Nitrates are anticipated to form during the photocatalytic NOx oxidation, which are known to damage porous materials by salt crystallization. In this study, the potential of salt crystallization damage due to calcium nitrate solution is investigated on cementitious materials for the first time. The results indicated that the calcium nitrate salt could induce salt crystallization damage on mortar, characterized by cracking and spalling at relative humidity lower than 35%. It is suggested that increasing the strength could mitigate the damage, by using water-to-binder ratio less than 0.4 and using less than 5% of TiO_2 nanoparticles replacement of cement.

8.2 Recommendations

Based on the current investigations on photocatalytic cement-based materials, some recommendations are made as follows.

- It was shown from Chapter 3 that the surface hardness decreased significantly with TiO_2 nanoparticles replacement, which can be related to abrasion resistance.

Also, from Chapter 7, a possibility of a surface degradation after a long term exposure to NOx and varying moisture states was found. It is recommended that a novel experimental technique be developed to measure the abrasion resistance in pavements for the photocatalytic materials. Also, for long term durability, it is recommended that these photocatalytic cementitious materials be used in a vertical configuration such as on walls, rather than used as a horizontal component such as pavements to decrease the chance of abrasion. This will also ensure that photocatalytic oxidation products be washed away more effectively by water rather than the horizontal configuration, where the photocatalytic final products could remain on the surface of cementitious materials for a longer time.

- It is recommended that these materials be used in a high pollutant concentration environment or in a confined place to achieve the best efficiency to cost ratio. For example, photocatalytic cement-based materials can be used in lower level parking decks or in tunnels where the NOx concentration is high and ventilation or dilution is poor. Especially in case of the parking decks, it is critical to lower the NOx level because people are exposed to high concentration of the NOx while walking to and from their cars.
- More generally, photocatalytic cement-based materials could be used for oxidizing other species rather than the NOx. For instance, these materials could be used in indoor applications to decrease indoor pollutants such as volatile organic compounds (VOCs), outgassing of some types of building materials, and odor molecules. These pollutants are the cause of sick building syndrome (SBS) [183], which is a well-known phenomenon caused from bad indoor air quality.

Durability issue in this case, would be much lower than outdoor applications. Also, these materials can be used for biological applications. It was reported that fungal colonization and fouling was strongly inhibited by use of photocatatic cementitious materials [48].

8.3 Future Research

The present research has contributed much to the knowledge of photocatalytic cement-based materials that contain titanium dioxide nanoparticles. However, much future research will be necessary in order to utilize this material in an optimal way. Some key topics that require additional research are listed below.

- One of the big challenges of using nanomaterials on cementitious materials is agglomeration. All of the TiO_2 nanoparticles used in this study were produced as micro-size agglomerates due to health concerns. These are not dispersed well in water even after ultrasonification and tend to reagglomerate due to high interfacial energies [184, 185]. Further effort is required to better disperse these particles in water in an acceptably easy way so that the method could be used in the field. Also, any further effects of using well dispersed nanoparticles, such as on cement hydration, strength development, microstructure, and photocatalytic efficiency, should be investigated.
- Properties of commercially available TiO_2's vary quite a bit depending on many factors. Companies use different processes to purify TiO_2 nanoparticles, and their primary particle size, agglomerate size, dispersability, and even photocatalytic

reactivity are different. Although the TiO_2's cannot be standardized, a certain minimum should be set, in terms of use with cementitious materials, on the photocatalytic reactivity and early and long-term properties. Furthermore, the use of treated TiO_2 that activates under a visible light could be examined [71, 186], which could be used in the interior of a building where UV light is not present.

- The study on the NO_2 binding in cementitious materials holds importance as a preliminary step examining the binding capacity qualitatively. A detailed research is required to quantitatively examine how much of the NO_2 can be bound in cementitious materials at various conditions such as varying w/c, humidity, NO_2 concentration. Also, it is necessary to investigate whether the NO_2 molecules are freely bound or permanently bound in the cementitious materials, and to examine any possibility if the NO_2 adsorbed could take part in chemical reactions with cement substrate.
- Recently, a new mathematical model was suggested by Tomellini to explain the dissolution-precipitation reaction taking place on the surface of small particles, based on the nucleation and growth processes [187]. This model considers two different nucleation rates, continuous and simultaneous, thus enabling more detailed analysis. Since this model was successfully applied to explain the kinetics of C_3S hydration, it could be further applied to the system with inert nanoparticles such as TiO_2.
- This research utilized fluorescent lamps as a UV light source to provide constant UV irradiation to samples in a controlled environment. However, the sunlight might have a different effect on the photocatalytic cement samples [188]. A

similar NOx degradation experiment is suggested under the sunlight to better simulate the field condition because most of the photocatalytic cements are installed in the external environment. Also, an in-situ experiment could be performed near major roadways in the long-term to investigate any possible durability issues that are not expected in this study.

- From the observations in Chapter 6, it is suggested that longer duration and more intense environmental conditions be used in the NOx-wet-dry cycling, in order to examine if the pits, as observed by the SEM, have negative effect on the durability of cementitious materials.
- Results from life cycle analysis (LCA) suggest that the overall environmental impact of the TiO_2-cement is significantly higher than ordinary cement paste, mostly coming from the production of TiO_2 nanoparticles [189]. Although the photocatalytic cement is capable of diminishing environmental NOx during its lifetime, it might not overcome the environmental cost associated with the production in an acceptable amount of time. Thus, further research on other types of nanomaterials can be beneficial in terms of sustainable development. The nanomaterials that have lower embedded energy but have similar acceleratory effect on cement hydration and strength development would be ideal option to replace TiO_2 nanoparticles.
- Relationship between surface hardness, strength, and abrasion resistance should also be investigated when nanoparticles are added to cementitious materials.

8.4 References

48. Giannantonio, D.J., et al., *Effects of concrete properties and nutrients on fungal colonization and fouling.* International Biodeterioration & Biodegradation, 2009. **63**(3): p. 252-259.

71. Tseng, Y.H., et al., *Visible-light-responsive nano-TiO_2 with mixed crystal lattice and its photocatalytic activity*. Nanotechnology, 2006. **17**(10): p. 2490-2497.

183. Godish, T., *Sick buildings : definition, diagnosis, and mitigation*. 1995, Boca Raton :: Lewis Publishers.

184. Mandzy, N., E. Grulke, and T. Druffel, *Breakage of TiO_2 agglomerates in electrostatically stabilized aqueous dispersions.* Powder Technology, 2005. **160**(2): p. 121-126.

185. Horst, A.M., et al., *Dispersion of TiO_2 nanoparticle agglomerates by pseudomonas aeruginosa.* Applied and Environmental Microbiology, 2010. **76**(21): p. 7292-7298.

186. Ishibai, Y., et al., *Photocatalytic oxidation of NOx by Pt-modified TiO_2 under visible light irradiation.* Journal of Photochemistry and Photobiology A: Chemistry, 2007. **188**(1): p. 106-111.

187. Tomellini, M., *Kinetics of dissolution-precipitation reaction at the surface of small particles: modelling and application.* Journal of Materials Science, 2012. **47**(2): p. 804-814.

188. Saquib, M. and M. Muneer, *Semiconductor mediated photocatalysed degradation of an anthraquinone dye, remazol brilliant blue R under sunlight and artificial light source.* Dyes and Pigments, 2002. **53**(3): p. 237-249.

189. Jayapalan, A.R., B.Y. Lee, and K.E. Kurtis, *Can 'nano' be 'green'? Comparing efficacy of nano and microparticles in cementitious materials.* Cement & Concrete Composites.

VITA

BO YEON LEE

Bo Yeon Lee was born on March 1st, 1982. She graduated from Myung-Il Girls' High School in Seoul, Korea in 2000. Bo Yeon received a B.S. in Architectural Engineering from Yonsei University, Seoul, Korea in 2005. Following her undergraduate studies, she worked at 3D Structural Engineers, Seoul, Korea from 2005 to 2006 as a structural engineer before coming to Georgia Institute of Technology for graduate studies. At Georgia Institute of Technology, she received an M.S. in 2007 and a Ph.D. in 2012, both in Civil Engineering. Her doctoral work emphasizes Structural Engineering and Materials Science.